Università di Pisa

Corso di Dottorato in Matematica

Tesi di Dottorato

Satellite Geodesy of Other Planets

Candidato:
Daniele Serra

Relatore:
Prof. Andrea Milani Comparetti

– Lad, I've never seen anyone with more natural talent for sailing!
– There's no such thing as talent, cap'n! Only inspiration and ambition!

---

from *The Life and Times of Scrooge McDuck*
by Don Rosa

Contents

Introduction

Satellite geodesy of the Earth

According to (Helmert, 1880), *geodesy* is the science of the measurement and the mapping of the Earth's surface. It is a very ancient science, already known in the Ancient Greece (Eratosthenes, for instance, measured the circumference of the Earth using a simple astronomic argument) and also in the Eastern world (Al-Biruni in the Middle Age measured the radius of the Earth using trigonometry). In the early modern period, the invention of the telescope and the creation of the logarithmic tables allowed the development of triangulation and grade measurement. Noteworthy are the two expeditions dispatched by the French Academy of Sciences, directed to Torne Valley and to Ecuador, aimed at measuring the oblateness of the Earth.

Nowadays, thanks to the development of space industry, geodesy has expanded its methods and applications and a new discipline has taken root, the so-called *satellite geodesy*. Based on the observations of mainly artificial bodies orbiting the planet, such discipline deals with three main problems (cf. (Seeber, 2003)):

Geodesy determination of precise global, regional and local three-dimensional positions;

Gravimetry determination of Earth's gravity field;

Geodynamics measurement and modeling of geodynamical phenomena (e.g., polar motion, Earth rotation, crustal deformation).

Actually, if one considers the Moon a source of satellite measurements, satellite geodesy has its roots in the beginning of the XIX century, when Laplace used

observations of the lunar nodal motion to measure the Earth's flattening. After the launch of the first artificial satellite, Russian SPUTNIK-1 (October 4, 1957), the knowledge of our planet has improved rapidly: in 1959 the third zonal harmonic coefficient was measured ("Earth Is Pear Shaped!", see Fig. 1), in 1962 a geodetic connection between France and Algeria was established and by 1964 scientists determined the general shape of the Earth's geoid. For the last 20 years, satellite geodesy has been giving an essential contribution to the GPS service, which is still evolving thanks to the continuous improvements in terms of spacial and temporal resolution of the Earth's gravity field.

Satellite geodesy of other planets

Almost at the same time, attention was drawn also to interplanetary space missions, whose targets were other planets of the solar system, the Sun, asteroids, comets, the outer space. The first attempt of sending a spacecraft towards another planet dates back to 1961, when the Sovietic probe Venera 1 was launched; it was intended to enter a Venus orbit, but the radio contact was lost before the flyby. Since that first unsuccessful effort, many other missions have achieved their goals, making it possible to answer some of the same questions raised for Earth. Missions like *Mariner 10* to Mercury, *Voyager 1* and *2* to the outer planets, *Mars Global Surveyor* to Mars and *Cassini-Huygens* to Saturn helped the mankind gain insight into the characteristics of the other planets and understand more about the origins and the formation of the Solar System and the Earth itself.

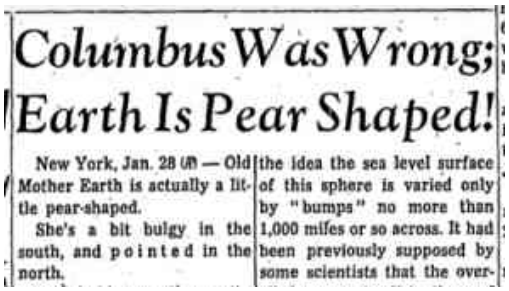

Columbus Was Wrong;
Earth Is Pear Shaped!

New York, Jan. 28 (AP) — Old Mother Earth is actually a little pear-shaped.

She's a bit bulgy in the south, and pointed in the north.

the idea the sea level surface of this sphere is varied only by "bumps" no more than 1,000 miles or so across. It had been previously supposed by some scientists that the over-

Figure 1: A fragment from the *Chicago Tribune*'s issue dated January 29, 1959 (CT, 1959) reporting the Vangard's discovery about the asimmetry of our planet with respect to the equatorial plane, the so-called pear shape. Mathematically it is showed by the presence of a non-zero gravitational momentum J_3.

One of the main differences between a space mission on Earth and one on another planet is the environment in which they operate: while in the first case one can build very accurate mathematical models of all the gravitational and non-gravitational perturbations experienced by a probe, in the second case the objective of the space mission is to *find* and/or *verify* such models, most of the times. For instance, planet Jupiter as well as Saturn are fluid bodies, thus for them the rigid body laws hold only in first approximation; this means that new models for the

gravity field and the rotation must be studied and space missions help reach this goal.

Another difference is that space missions on other planets are often planned to undertake several experiments at the same time, whereas Earth missions are usually focused on a single experiment. This requires a hard work during the design phase in setting the mission parameters (total duration, orbit shape, ...) so that all the experiments give the best outcomes. Of course this is difficult to accomplish and most of the times a compromise between quality of the results of a single experiment and number of experiments must be reached.

For its nature of using precise measurements to, from, or between artificial satellites, satellite geodesy of other planets requires a comprehensive knowledge of satellite motion under all the active forces and perturbations as well as the description of the positions of satellites in suitable reference frames. For example, it is necessary to study in detail also the relativistic effects that can be experienced by the probe, such as the corrections to the observables due to the curvature of space-time or the difference of proper times of the planets. For this reason, satellite geodesy belongs to *basic sciences*. On the other hand, when satellite observations are used to solve practical problems, it belongs to the field of the *applied sciences*. The work described in these pages follows the same duality: mathematical models are developed independently within a self-consistent theory and have general validity; nevertheless, most of them find a natural application in or are motivated by the *Radio Science Experiment* (RSE) of interplanetary space missions, especially the NASA Juno mission to Jupiter.

Outline

This thesis is divided in two parts. In the first part we focus on the numerical simulations of the RSE of the mission Juno in jovicentric orbit. The second part deals with the analysis of real data of the cruise-stage of the mission Juno and the assessment of the numerical error introduced by the orbit determination software developed for the analysis of such data.

Part I: The Radio Science experiment of the mission Juno

Ever since the first space missions were launched, Radio Science experiments have been performed. The RSE of a space mission is performed either analyzing the Doppler/ranging signal reaching the Earth from the spacecraft, or by analyzing the signal modified by occulations of the spacecraft by a planet (cf. (Dehant et al.,

2011)). Some examples of the objectives of RSE are: the measurement of the gravity field of the planet (Gravity Science, see Section 1.3), the assessment of the validity of general relativistic theories, the determination of the composition of the atmosphere of a planet and of its atmospheric dynamics.

NASA's mission Juno will reach planet Jupiter on July 5, 2016 at 02:37 UTC and, among all the experiments planned, will undertake a RSE. Objectives of the latter are: the determination of Jupiter's gravity field and the parameters giving the tidal deformation of Jupiter; the determination of the position of the rotation pole of Jupiter and the angular momentum. Thanks to such information, it will be possible to improve our knowledge of Jupiter's origins and interior structure.

This part is organised as follows.

Chapter 1 contains a brief summary of the previous space missions to Jupiter as well as a detailed description of the Juno mission, its objectives, and a specific focus on the Gravity Science experiment and the design of the orbit of Juno when at Jupiter.

Chapter 2 deals with the mathematical formulation of Orbit Determination and describes the algorithms necessary to process the data obtained during a RSE. Moreover, it contains a presentation of the ORBIT14 Orbit Determination software developed at the Department of Mathematics of the University of Pisa, which has been used to perform the simulations presented in this work.

The results of the simulations regarding the gravity field of Jupiter are described in Chapter 3. Here, we start introducing a semi-analytical method to predict the uncertainties of the spherical harmonics coefficients of the gravity field of a planet, valid in general for any spacecraft orbiting a celestial body. Then, we cope with the results of the simulations for the spherical harmonics coefficients of Jupiter. Finally, since the observations of the planet will be confined to a latitude band in the north hemisphere of the planet, we introduce a local model for the gravity field of Jupiter, based on ring shaped mascons. This chapter also deals with the determination of Jupiter's Love numbers, measuring the tidal response of the planet to the attraction of its natural satellites and the Sun.

In Chapter 4 we tackle the determination of Jupiter's pole of rotation and the magnitude of its angular momentum, the latter particularly important because it is strictly connected to Jupiter's normalized polar moment of inertia, fundamental for the determination of the interior structure of the planet. The joint discussion is due to the fact that we found high correlation between the parameters related to these physical quantities, mirroring the fact that their effects on the motion of the spacecraft are indistinguishable. We propose a possible solution and hint at an alternative method for determining Jupiter's moment of inertia.

Part II: Analysis of the cruise-stage data

Whereas the first part of this thesis is dedicated to the analysis and description of the results of simulations of the Juno RSE, the second part deals with the analysis of real data from the Juno spacecraft. Although the scientific content of these data is rather poor because they have been obtained during the cruise phase, when the relative position of the Earth-Sun-spacecraft would not allow a Solar Conjunction Experiment, the reasons for such an analysis are at least two. Firstly, it was a chance to assess the performance of the telecommunication system onboard and test the quality of the data. The second motive is more relevant for the scope of this thesis and is the validation of the ORBIT14 software and the assessment of the numerical noise introduced therein. We will show that the software is in good condition and well-performing, the numerical error being negligible.

This thesis is the natural conclusion of a three-year research work, whose aim was to get ready to tackle the analysis of the data of the space mission Juno. This entailed developing a rock-solid theoretical background which had to take into account the peculiarities of the mission, and producing numerical simulations of the scheduled scientific experiment. For the latter, it was necessary to have at our disposal an orbit determination software which could exploit the characteristics of the mission which up to that point were confined to the theory. Because of the experience gained through the years, our choice was to develop our own software. It is redundant to say that we had to cope with the July 5, 2016 deadline and make sure that the software would be ready by that time. This thesis shows that we achieved what we planned to do three years ago: we managed to produce a software we can fully control. We are prepared to analyse the real data when they start arriving later in 2016, undertake an actual experiment, and deliver sound scientific results. Thus the scientific production is constrained to the analysis of the data and slim are the chances of publishing some results earlier than 2018. For the moment, we have one published article, (Tommei et al., 2015), and a submitted one, reporting most of the results contained in this dissertation. The author also participated in the work (Le Maistre et al., 2016) during his research visit at Jet Propulsion Laboratory from April to August 2015 in the program JPL Visiting Student Researchers Program (JVSRP).

We are not stating - and do not mean to - that it is all downhill from here. In fact we are conscious that the hardest part is to come: we had the chance in the past three years to realise that coping with real data is deeply different from performing simulations. Yet if any modifications are needed or new science is

found that requires software adjustements, having access to the source code will facilitate our job.

Acknowledgments

The research leading to the results presented in this thesis has been financially supported by the Italian Space Agency within the scope of the contract "Radioscienza per BepiColombo e Juno - fasi B2/C/D - Attività scientifiche", ASI/2007/I/082/06/0.

I would like to thank Jet Propulsion Laboratory for funding my participation in the JPL Visiting Student Researchers Program.

I wish to express my very great appreciation to the two referees who reviewed this thesis, for providing relevant and interesting remarks, contributing to the overall improvement of the work.

I am deeply grateful to Professor Andrea Milani, my supervisor, for the patient guidance and for the respect and the attention he has always shown in the workplace.

I would like to offer my special thanks to Linda Dimare, with whom I have shared many hours of tireless work and as many coffee breaks.

I wish to acknowledge the support of Giacomo Tommei, Stefano Cicalò, Davide Bracali Cioci, who answered all my questions.

Thank you to Sébastien Le Maistre for the help provided as a colleague and the enjoyable days we shared as friends, and to his family, Stéphanie, Maëlle, Cielle, Ulysse, for the precious moments we shared.

Special thanks to all the colleagues with whom I have shared a room or a desk, Federica, Hélène, Giulia, Sara, Giulio, Stefano, Fabrizio, Giacomo, Giovanni and Giulia, for the constant support and their friendship.

Finally, for their unconditional love and trust, I wish to thank my family, my friends, my boyfriend and all those people who do not belong to any of these categories, but do have a place in my heart.

List of acronyms and abbreviations

AD	Allan Deviation
ASI	Italian Space Agency
AWVR	Advanced Water Vapor Radiometer
BCRF	Barycentric Celestial Reference Frame
BCRS	Barycentric Celestial Reference System
BJS	Barycenter of Jovian System
DOY	Day Of Year
DSN	Deep Space Network
DSS	Deep Space Station
ECRF	Ecliptic Celestial Reference Frame
ECRS	Ecliptic Celestial Reference System
ESA	European Space Agency
GS	Gravity Science
ICRF	International Celestial Reference Frame
ICRS	International Celestial Reference System
ITAR	International Traffic in Arms Regulation
ITRF	International Terrestrial Reference Frame
ITRS	International Terrestrial Reference System
JOI	Jupiter Orbiter Insertion
JUICE	JUpiter ICy moons Exploration
JPL	Jet Propulsion Laboratory
KaT	Ka-band Transponder
LCP	Left-hand Circularly Polarized
MOI	Moment Of Inertia
NASA	National Aeronautics and Space Administration
PPN	Post-Newtonian Parameters
RCP	Right-hand Circularly Polarized

RSE	Radio Science Experiment
S/N	Signal to Noise Ratio
SEP	Sun-Earth-Planet
SPICE	Spacecraft Planets Instruments C-matrix Events
STD	STandard Deviation
TDB	Barycentric Dynamical Time
TDJ	Jupiter Dynamical Time
TDT	Terrestrial Dynamical Time

Part I

Simulations of the Radio Science experiment of the mission Juno

CHAPTER 1

The Juno mission

Contents

Outline: This chapter is dedicated to the description of the Juno mission to Jupiter. Before describing in detail the scientific objectives and the experiments planned to be undertaken as to achieve such goals, a brief synopsis of some of the past space missions aimed at exploring Jupiter is given.

1.1 The exploration of Jupiter

Since the early years of the 1970s, many spacecrafts have visited Jupiter, although only one of them was designed specially for the exploration of the largest planet of the Solar System. In this section we summarize the most important discoveries made by these missions. For a detailed comparison, the reader is invited to refer to (Young, 1998).

Figure 1.1: Jupiter photographed by Pioneer 10 during the close approach, December 1973. Credit: NASA.

The Pioneer mission

The first space probe that encountered Jupiter and had the chance to obtain the first close-up images of the planet was NASA's *Pioneer 10*. The spacecraft made its closest approach with Jupiter on December 3, 1973, more than one year after becoming the first human-made object to cross the asteroid belt. On that occasion, Pioneer 10 mapped Jupiter's radiation belts, located the planet's magnetic field and established that Jupiter is a liquid planet. Almost exactly one year later, the *Pioneer 11* spacecraft reached the distance of $0.6R_{\mathrm{Jup}}$ from the surface of the planet ($\sim$ 36000 km), obtaining the first images of the *Great Red Spot* and observing the polar regions. The particularly short distance from the center of the planet allowed Pioneer 11 to sample the inner magnetosphere of Jupiter, paving the way for the further studies pursued by the *Voyager* program. By the Doppler data from the two Pioneer spacecrafts, (Anderson, 1976) computed the first gravity field solution of Jupiter, up to degree 6 (see Table 1.1).

Coefficient $\times 10^{-6}$	Pioneer 10	Pioneer 11	Pioneer and Voyager
J_2	14720 ± 40	14750 ± 50	14697 ± 1
J_3	< 150	10 ± 40	n.a.
J_4	-650 ± 150	-580 ± 40	-584 ± 5
J_6	assumed zero	50 ± 60	31 ± 20

Table 1.1: Column 2 and 3: gravity field of Jupiter from analysis of Doppler Data from Pioneer 10 and Pioneer 11 (cf. (Anderson, 1976)). Column 4: gravity field of Jupiter from analysis of Doppler Data from both the Pioneer and the Voyager spacecrafts (cf. (Campbell and Synnott, 1985)).

The Voyager program

The NASA's *Voyager* program consisted in two spacecrafts aimed at exploring the outer Solar System. The two probes succeded in making a Grand Tour of the four giant planets, providing a deeper insight into Jupiter and Saturn and - for Voyager 2 - becoming the only spacecraft to have visited Uranus and Neptune so far. During the two subsequent close approaches to Jupiter that took place in 1979, the two Voyager spacecrafts collected more than 33000 images of the giant planet. Great was the impact Voyager had on the exploration of Jupiter's atmosphere and magnetosphere. For instance, Voyager instruments first detected auroral emissions on Jupiter, a phenomenon that is planned to be investigated by Juno (cf. Section 1.2). The existence of a magnetotail on the antisolar side of Jupiter was confirmed by Voyager 1 and Voyager 2 proved that it extends to Saturn. The discovery of vulcanism on Jupiter's moon Io is presumably the most striking finding: although not being directly related to Jupiter, such volcanic activity was observed to affect the entire Jovian system. As far as the gravity field of Jupiter is concerned, Voyager contributed to improving the accuracy of the low-degree part of gravity field, as showed by (Campbell and Synnott, 1985) in their solution obtained using both Pioneer and Voyager Doppler data (see Table 1.1).

Galileo

Until the arrival of Juno at Jupiter, NASA's *Galileo* mission will remain the only space mission to have been designed specifically for the exploration of Jupiter and the only spacecraft to have orbited the planet. The project consisted of an orbiter and an atmospheric probe, the latter set to descend into Jupiter's atmosphere

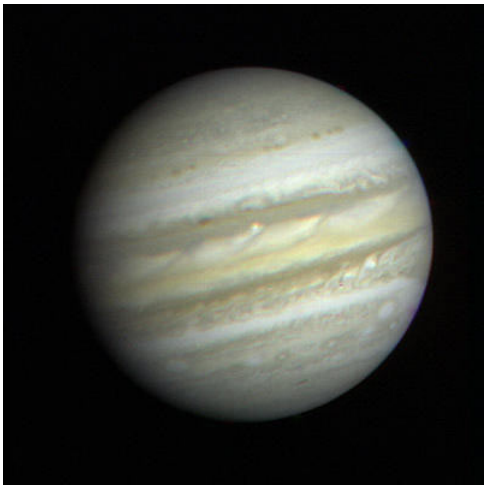

Figure 1.2: First close-up view of Jupiter by Voyager 1, January 1979. Credit: NASA.

right after the arrival of the orbiter, in 1995. Galileo provided the first direct sampling of Jupiter's atmosphere, from the thermosphere to the troposphere, revealing its chemical composition and the abundances of the different elements. Among the other accomplishments, Galileo verified that the winds observed on the surface extend below cloud levels. Unfortunately, the gravimetry experiment was compromised by a failure to the deployment of the high-gain antenna, thus no important contribution was given to the gravity field of Jupiter by Galileo. As the author himself suggests in (Young, 1998), Galileo changed the way scientists look at Jupiter. Whereas the pre-Galileo vision was to consider atmospheric composition, clouds, dynamics, thermal structure and energy balance like separate phenomena on Jupiter, now they are considered all coupled, making the goal of achieving a comprehensive study of Jupiter more challenging and possibly pushing it further in the future, when a space mission of the entire Jovian system is launched.

1.2 Motivation and scientific objectives

Juno is a NASA mission, the second within the New Frontiers program, aimed to study Jupiter by means of a polar orbiter. The mission and spacecraft, spin-stabilized and endowed with three solar arrays for power, are designed in such a fashion as to meet the scientific requirements despite Jupiter's high radiation and magnetic environment.

The spacecraft was launched on August 5, 2011 and will arrive at Jupiter on July 4, 2016. During the five-year journey, Juno performed two deep-space maneuvres in 2012 in preparation of the spacecraft's Earth flyby (for gravity assist) of October 2013. After the close approach with the Earth, the probe has gained enough velocity to reach Jupiter.

After Jupiter Orbit Insertion (JOI), the orbiter will study Jupiter for about 15 months. The payload of eight instruments carried by Juno will operate to collect science data and thus achieve the scientific objectives. After the nominal mission time, if not extended, Juno will be de-orbited into Jupiter for planetary protection reasons[1].

The scientific goals of Juno can be summarized in four main points: *atmosphere*, *magnetosphere*, *interior*, *origins*. In order to improve the general understanding on these themes, the scientific team has selected the following objectives to be met by Juno:

Atmospheric Composition - measuring Jupiter's abundance of water and ammonia.

Atmospheric Structure - investigating Jupiter's meterology, temperature profiles, atmospheric dynamics.

Magnetic Field - mapping the global magnetic field and providing information on the nature of the dynamo.

Gravity Field - in order to explore the distribution of mass inside the planet.

Polar Magnetosphere - exploration of the three-dimensional polar magnetosphere and aurorae.

For a detailed discussions of the previous points and a description of the instruments dedicated to the experiments, the reader can see (Grammier, 2008) and (Matousek, 2007).

Surely the several experiments that Juno will perform while at Jupiter will help improve our knowledge of the planet as it is nowadays. Apart from that, if we consider that Jupiter had a primary role in the formation of the Solar System, then Juno's findings will also provide more clues to understanding the origin and evolution of the Solar System. In conclusion, not only is Juno a chance to learning our own history, but also an opportunity to improve our knowledge of the several giant planets orbiting other stars.

[1]It is indeed believed that Jupiter's satellite Europa might host life. In view of a possible future mission on Europa, letting the spacecraft in Jupiter system could interfere with the search of local life, because of biological contamination risks.

1.3 Gravity Science

The experiment of Gravity Science (GS) is aimed at measuring Jupiter's Gravity Field in order to discriminate amongst different models of the distribution of mass in the planet's interior. In particular, Juno's GS experiment has been conceived to:

- provide constraints on the mass of the core;
- determine the depth of the zonal winds;
- investigate the response to tides raised by the Jovian satellites.

In terms of harmonic coefficients (see Section 3.1), the objective of the GS experiment is the determination of Jupiter's even coefficients J_2 to J_{14}.

The instrument used for the GS experiment is a telecommunication system which uses both X and Ka-band frequencies, providing a two-way signal from the ground station to the spacecraft, allowing to observe the Doppler shift in the proximity of Jupiter. The X-band system has been provided by Jet Propulsion Laboratory, whereas the Ka-band translator (KaT) carried by the spacecraft has been supplied by the Italian Space Agency (ASI). The accuracies reachable for the measurement in terms of relative velocity is of 3×10^{-4} cm/s over an integration time of 1000 sec. The ground antenna is the DSS-25 antenna at the Deep Space Network (DSN) station in Goldstone, CA (more details can be found in (Mukai et al., 2012)).

1.4 The orbit of Juno

Until October 2013, the Juno orbit during the jovicentric phase was planned to be a polar, 11-day orbit, characterized by high eccentricity, $e = 0.946$, thus with a very low perijove distance, $r_p \sim 1.04 R_{\text{Jup}}$, and a very high apojove distance, $r_a \sim 39 R_{\text{Jup}}$. Such a configuration allowed the spacecraft to avoid Jupiter's radiation belt for most of the orbital period, guaranteeing the integrity of the instrumentation for the duration of the mission. After experiencing several episodes of the spacecraft switching automatically to *safe mode*[2], the Juno team came up with the idea that a jovicentric orbit with longer period would have allowed more time to recover from safe mode in case that happened while at Jupiter. In July 2015 the new Juno orbit was finally approved by NASA and announced publicly.

[2] An operating mode during when only the essential systems are on.

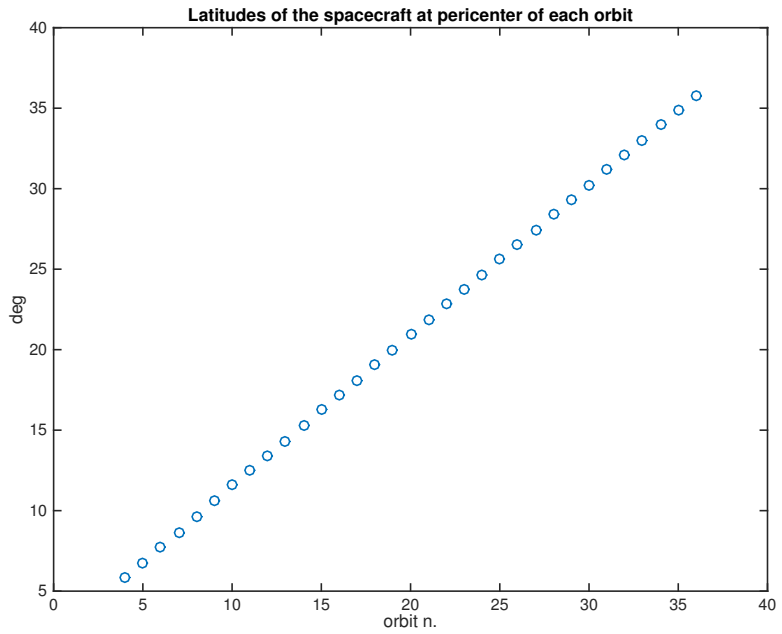

Figure 1.3: Latitudes of the spacecraft with respect to Jupiter's equator at pericenter for each orbit, from orbit 4 to orbit 36.

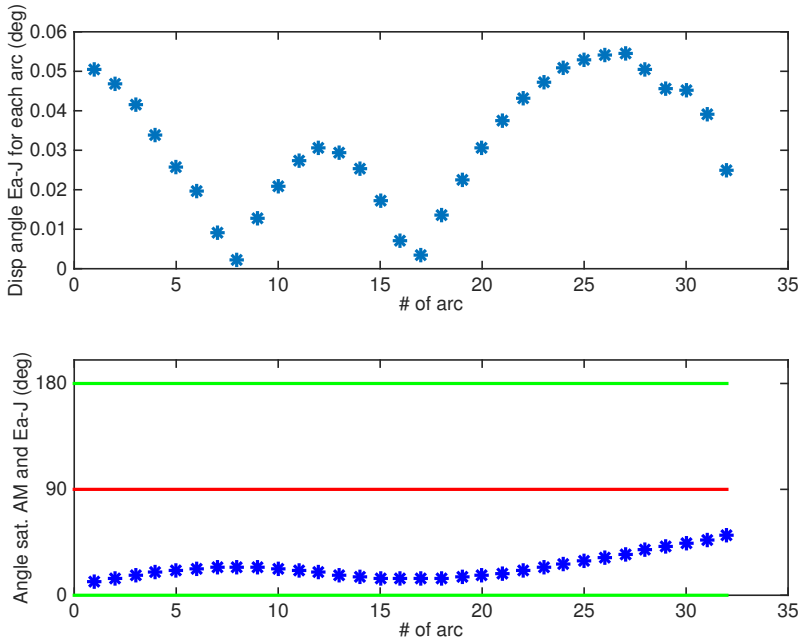

Figure 1.4: Top: angular displacement of the vector Earth-Jupiter with respect to previous position for each arc. Bottom: inclination of Juno's orbital plane with respect to the vector Earth-Jupiter.

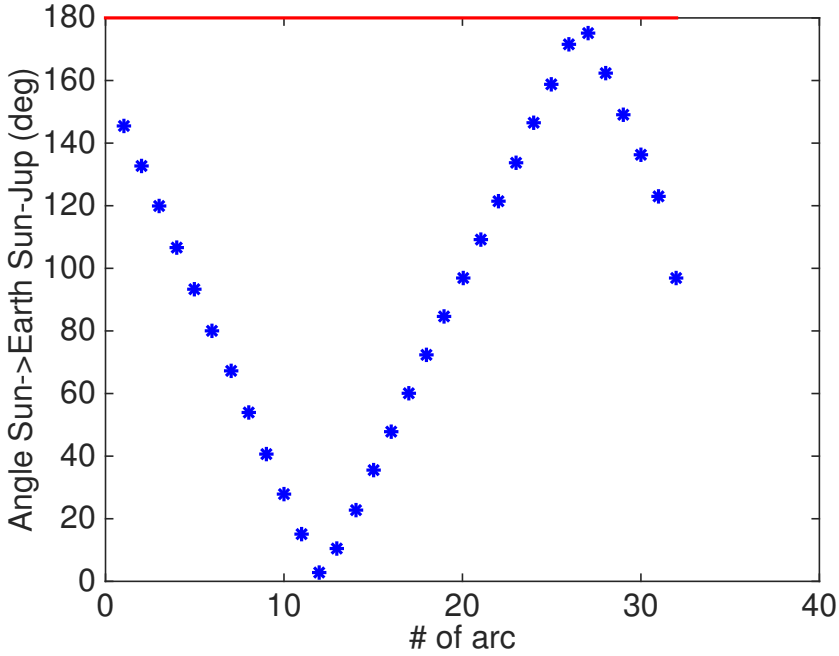

Figure 1.5: Sun-Earth-Planet (SEP) angle over the Juno mission.

After JOI, Juno will perform two 53.5-day orbits, for total of 107 days, which will prepare the spacecraft to the insertion in the scientific mission orbit, whose period is set now to 14 days. The perijove distance will vary from $1.06R_{\rm Jup}$ to $1.11R_{\rm Jup}$ (in terms of altitude of the spacecraft with respect to Jupiter's surface[3], from 4200 km to 7900 km) and the apojove distance on average $\sim 45.7R_{\rm Jup}$. The nominal mission will start in November 2016 and will end in February 2018. Thus, during the 15-month mission the probe will orbit the giant planet 35 times (plus one possible extra orbit). Orbit 5 and orbits 10 to 35 will be dedicated to GS, although communication with the spacecraft in the X-band will be available also during orbits 4 and 6 to 9. Data will be collected since 3 hours before the pericenter pass, until 3 hours later. By effect of Jupiter's oblateness, the latitude of the pericenter with respect to Jupiter's equator is not fixed in time: starting from about 6 deg N at orbit 4, it reaches about 35 deg N at orbit 35 (cf. Fig. 1.3).

Many maneuvers are scheduled during the orbit, out of the observation window at pericenter. For instance, right after every perijove a maneuver will ensure that the next orbit Juno will observe the right longitude of the planet. The middle-course maneuver is meant to change the longitude of the ascending node of the Juno orbit

[3]Being Jupiter a gaseous planet it is not obvious how to define its surface. Here we mean a sphere having as radius Jupiter's mean radius $R_{\rm Jup} = 69911$ km, obtained averaging the equatorial and the polar radii, measured at the 1 bar level of pression.

in order to have a more uniform coverage of Jupiter's surface. The large number of maneuvers is crucial for selecting the most convenient orbit determination method (see Section 2.1.2).

As regards the position of Juno's orbital plane in space, Fig. 1.4 and 1.5 show the evolution over the orbits when data will be available for GS. The orbit is close to face-on for almost the entire duration of the mission, thus making Juno always visible when Jupiter is in the sky. As we can see studying the Sun-Earth-Probe (SEP) angle, the Sun and Jupiter will be in opposition at arc 12 (orbit 15) and in conjunction at arc 27 (orbit 30).

CHAPTER 2

Orbit determination for space missions

Contents

Outline: In this chapter we describe the orbit determination method used for the Radio Science experiment of a generic space mission, having in mind that our goal is to apply the theory to the Juno mission. After recalling the classical least squares method proposed by Carl Friedrich Gauss, we show how to define the observable we deal with, the *range-rate* of the spacecraft, and give a sketch of how its computation can be tackled. Since it is particularly important for Juno, a

specific focus on the Shapiro effect follows. The chapter closes with a description of the orbit determination software *ad hoc* developed.

2.1 Non-linear least squares

Orbit determination for a space mission is based on the classical least squares method, first introduced in (Gauss, 1809). The concept of orbit determination in this case is strictly connected to the process of *parameter estimation*. By observing the spacecraft, not only do we want to calculate its orbit, but we can also attempt to determine a set of unknown - or poorly known - physical parameters chracterizing the planet orbited and its system. For a comprehensive analysis, see ((Milani and Gronchi, 2010), Chapter 5) or (Bierman, 2006).

Let $r_1, \dots, r_m$ be observations of the spacecraft at times $t_1, \dots, t_m$. The state vector of the spacecraft $\mathbf{y}$ is solution of the equation of motion

$$\begin{cases} \dfrac{d}{dt}\mathbf{y} = \mathbf{F}(t, \mathbf{y}, \boldsymbol{\mu}) \\ \mathbf{y}(t_0) = \mathbf{y}_0, \end{cases} \tag{2.1}$$

where $\mathbf{F}$ is dependent on $\mathbf{y}$ and on a vector of dynamical parameters $\boldsymbol{\mu}$, and $\mathbf{y}_0$ is the initial state at time t_0. Thus $\mathbf{y} = \mathbf{y}(t, \mathbf{y}_0, \boldsymbol{\mu})$. If $R(t, \mathbf{y}, \boldsymbol{\nu})$ is the *observation function* modeling the observation, where ν is a vector of *kinematical parameters* (e.g., the positions of the stations on Earth or the accelerometer readings) then we can define the *prediction function* by composition of R and $\mathbf{y}(t, \mathbf{y}_0, \boldsymbol{\mu})$:

$$r(t) := R(t, \mathbf{y}(t, \mathbf{y}_0, \boldsymbol{\mu}), \boldsymbol{\nu}). \tag{2.2}$$

The previous, evaluated at times $t_1, \dots, t_m$, gives a prediction of the observations $r_1, \dots, r_m$. Ideally, the difference between r_i and $r(t_i)$ should be zero. In fact, even in case of perfect model, the difference is always non zero, for instance because of the measurement noise affecting r_i. The difference $\xi_i := r_i - r(t_i)$ is called residual at time t_i, the residual vector is $\boldsymbol{\xi} := (\xi_i)_{i=1,\dots,m}$. Note that $\boldsymbol{\xi} = \boldsymbol{\xi}(t, \mathbf{y}_0, \boldsymbol{\mu}, \boldsymbol{\nu})$.

Let us now select a subvector[1] $\mathbf{x}$ of $(\mathbf{y}_0, \boldsymbol{\mu}, \boldsymbol{\nu})$, made of parameters we would like to determine. Let N be the length of $\mathbf{x}$. Let us define the *target function*

$$Q(\mathbf{x}) = \frac{1}{m}\boldsymbol{\xi} \cdot \boldsymbol{\xi}.$$

The idea for the determination of $\mathbf{x}$ is given by the minimum principle: the solution $\mathbf{x}^*$ is a point of minimum for Q. Thus the solution $\mathbf{x}^*$ satisfies

$$\frac{\partial Q}{\partial \mathbf{x}}(\mathbf{x}^*) = \mathbf{0}.$$

[1] We will also refer to such vector as vector of *solve-for* parameters.

The previous is a non linear equation, which can be solved using an iterative method. We omit the details and skip to the main result: the nominal solution $\mathbf{x}^*$ is given by the limit, if exists, of the sequence $(\mathbf{x}_k)$ generated by the *differential correction algorithm*

$$C(\mathbf{x}_{k+1} - \mathbf{x}_k) = -B^T \boldsymbol{\xi}. \tag{2.3}$$

The matrices B, C are respectively the *design matrix* and the *normal matrix* and are defined as follows

$$B = \frac{\partial \boldsymbol{\xi}}{\partial \mathbf{x}}, \quad C = B^T W B,$$

where W is the weight matrix. Note that, like $\boldsymbol{\xi}$ and Q, also B and C depend on $\mathbf{x}$, $B = B(\mathbf{x}), C = C(\mathbf{x})$.

2.1.1 Probabilistic interpretation

The minimum principle expresses the optimization interpretation of the least squares method. The following theorem, proved by Gauss, gives a probabilistic interpretation. The symbol $N(\mathbf{m}, G)$ indicates the *multi-dimensional normal (or Gaussian) distribution* of mean vector $\mathbf{m}$ and covariance matrix G.

Theorem 1. *Let us suppose that the residual vector $\boldsymbol{\xi}$ is a vector of random variables with probability density $p(\boldsymbol{\xi}) = N(\mathbf{0}, I)(\boldsymbol{\xi})$, where I is the identity matrix. Then the solution of a linear least squares problem has a Gaussian probability density, with mean equal to the nominal solution $\mathbf{x}^*$ and covariance matrix equal to the inverse of the normal matrix C.*

The matrix $\Gamma = C^{-1}$ is called *covariance matrix*. Thanks to the previous theorem we have that the covariance matrix $\Gamma(\mathbf{x}^*)$, computed at convergence of the differential correction algorithm, contains the formal errors and the correlations of the solve-for parameters. In particular, the *formal error* of the parameter x_i is

$$\sigma(x_i) = \sqrt{\gamma_{i,i}} \tag{2.4}$$

and the *correlation* between any two parameters $x_i, x_j,\ i \neq j$, is

$$\operatorname{corr}(x_i, x_j) = \frac{\gamma_{i,j}}{\sigma(x_i)\sigma(x_j)}.$$

2.1.2 Multi-arc method

Sometimes it is impossible to model the dynamics of the spacecraft over the entire time span of the observations with a single set of initial conditions $\mathbf{y}_0$. It is the

case when the non-gravitational accelerations acting on the orbiter are not known accurately enough or when many maneuvres are scheduled along the trajectory.

The multi-arc strategy is a possibile solution to this issue. The time span of observations is divided into disjoint subinterval and the observations belonging to each subinterval are said to constitute an *arc*. Each arc has its own set of initial conditions, thus it is as if each arc is the result of the observation of a new spacecraft.

If n is the number of arcs, the observations and the residuals are split in n sub-vectors. The vector of solve-for parameters can be split in the vector of *global parameters* $\mathbf{g}$ and that of *local parameters* $\mathbf{h}$,

$$\boldsymbol{\xi} = \begin{pmatrix} \boldsymbol{\xi}_1 \\ \vdots \\ \boldsymbol{\xi}_n \end{pmatrix} \quad \text{and} \quad \mathbf{x} = \begin{pmatrix} \mathbf{g} \\ \mathbf{h} \end{pmatrix}.$$

The vector of local parameters is also split in n vectors $\mathbf{h}_j$, where $\mathbf{h}_j$ is associated with arc j. The residuals $\boldsymbol{\xi}_j$ depend on $\mathbf{h}_j$ only:

$$B^{(j)}_{\mathbf{g}} := \frac{\partial \boldsymbol{\xi}_j}{\partial \mathbf{g}}, \quad B^{(j)}_{\mathbf{h}_i} := \frac{\partial \boldsymbol{\xi}_j}{\partial \mathbf{h}_i} = \mathbf{0} \ \text{ for } \ i \neq j.$$

Consequently the normal matrix C has an arrow-like structure:

$$C = \begin{pmatrix} C_{\mathbf{gg}} & C_{\mathbf{gh}} \\ C_{\mathbf{hg}} & C_{\mathbf{hh}} \end{pmatrix} = \begin{pmatrix} C_{\mathbf{gg}} & C_{\mathbf{gh_1}} & \dots & C_{\mathbf{gh_n}} \\ C_{\mathbf{h_1 g}} & C_{\mathbf{h_1 h_1}} & \mathbf{0} & \mathbf{0} \\ \vdots & \mathbf{0} & \ddots & \mathbf{0} \\ C_{\mathbf{h_n g}} & \mathbf{0} & \mathbf{0} & C_{\mathbf{h_n h_n}} \end{pmatrix}.$$

This simplifies the solution of the normal system (2.3), allowing to solve $n + 1$ smaller normal systems in place of a larger one (see (Milani and Gronchi, 2010), Chapter15 for the explicit formulae).

In the case of the mission Juno, the geometry of the observations - 6 hours every 14 days - suggests the use of a multi-arc strategy. On the one hand, this means that we can ignore all the dynamics outside the observation time, including all the maneuvers, obtaining a considerable simplification of the dynamical model. On the other hand, the price to pay is that now we must solve for at least $6n$ local parameters. In the Juno case, being $n = 32$, this is a rather convenient compromise.

2.1.3 Apriori conditions

When some information on one or more solve-for parameters is available, it may be taken into account during the differential correction process. This can happen for instance when another orbiter previously visited the planet and produced a solution of the gravity field or if Earth-based observations have been collected, e.g. visual astrometry, optical transits etc[2]. If on the one hand this is useful to stabilize the fit because the search of the solution is limited to a subset of the space of the parameters, on the other hand the use of apriori information - if available - is the only way to cure a rank deficiency (cf. Milani and Gronchi (2010), Chapter 6) of that specific orbit determination problem.

Let us suppose that some information on the single parameters is provided by some source (past space missions, ground-based gravimetry, etc.) and let $\mathbf{x}^P$ the apriori values of the solve-for parameters. To each apriori observation $x_i = x_i^P$ is associated the apriori standard deviation σ_i. If $C^P := \mathrm{diag}(\sigma_1^{-2}, \ldots, \sigma_N^{-2})$, this is equivalent to the normal equation $C^P\mathbf{x} = C^P\mathbf{x}^P$. The target function is modified to take into account the apriori information, thus becoming

$$Q(\mathbf{x}) = \frac{1}{m+N}[\boldsymbol{\xi}\cdot\boldsymbol{\xi} + (\mathbf{x}-\mathbf{x}^P)\cdot C^P(\mathbf{x}-\mathbf{x}^P)].$$

Finally, the new normal system is

$$[C + C^P]\Delta\mathbf{x} = -B^T\boldsymbol{\xi} + C^P(\mathbf{x}-\mathbf{x}^P),$$

where $\Delta\mathbf{x} = \mathbf{x}_{k+1} - \mathbf{x}_k$.

Note that the same formulae can be used in case we knew that a subset of the solve-for parameters satisfies a number k of linear relations[3]. Let $F(\mathbf{x}-\mathbf{x}^P) = \mathbf{0}$ the linear system expressing such linear relations (here $F \in \mathbb{R}^{k\times N}$). We define the apriori normal matrix as

$$C^P = F^T W^P F, \tag{2.5}$$

where $W^P = \mathrm{diag}(\sigma_1^{-2}, \ldots, \sigma_N^{-2})$ is the matrix of the apriori weights.

It is important to remark that the use of apriori conditions should be based on the actual availability of previous information. The risk of using fictitious apriori observations - or with very low apriori standard deviations associated - is to obtain a solution which is fictitious as well.

[2]The solutions for Jupiter gravity field given by (Jacobson, 2003) were in fact obtained combining spacecraft and Earth-based observations.

[3]Such relations usually come from theoretical considerations. For example, the *Nordtvedt equation* (cf. (Nordtvedt, 1970)) is a linear combination of some Post-Newtonian relativity parameters used for Relativity experiments. See also Section 3.4 for an example regarding the Juno mission.

2.2 Observations

Once the equation of motion (2.1) is solved for the spacecraft and for all the bodies involved in the dynamics, we need to tackle the computation of the observations, that is of the prediction function (2.2). For Juno the observables will be almost exclusively *range-rate* measurements, that is the component of the velocity of the spacecraft along the direction of the observer. Since the computation of the range-rate entails the computation of the *light-time*[4] from the station on Earth to the spacecraft, which is equivalent to calculating the *range*, the distance of the spacecraft from the antenna on Earth, we will show how to obtain both.

The definitions are very simple: if the range of the spacecraft is the distance between the ground antenna on Earth and the center of phase of the antenna on the spacecraft, the range-rate is the time derivative of the range. Despite the easy-to-write definitions, the computation of both range and range-rate is definitely non trivial. It is beyond the scope of this work to give a comprehensive analysis of the well-known problem of the computation of the light-time, thus we will outline the key-points and indicate other works the reader can refer to.

2.2.1 Light-time iterations

In a flat space-time where the light propagates instantaneously, the range is (see Fig. 2.1)

$$r_0(t) = \left|\mathbf{y}_{\mathrm{BJS}} + \mathbf{y}_{\mathrm{Jup}} + \mathbf{y}_{\mathrm{S/C}} - \mathbf{y}_{\mathrm{E}} - \mathbf{y}_{\mathrm{ant}}\right|, \tag{2.6}$$

where $\mathbf{y}_{\mathrm{BJS}}$ and $\mathbf{y}_{\mathrm{E}}$ are respectively the position of the Barycenter of the Jovian System (BJS) and the Earth Barycenter with respect to the Solar System Barycenter, $\mathbf{y}_{\mathrm{Jup}}$ is the position of Jupiter Barycenter with respect to the BJS, $\mathbf{y}_{\mathrm{S/C}}$ is the position of the orbiter with respect to Jupiter Barycenter and $\mathbf{y}_{\mathrm{ant}}$ is the position of the ground antenna with respect to the Earth Barycenter. All the previous vectors are computed at time t [5].

Since the signal has finite velocity $c = 299,792.458$ km/s, it takes a time Δt to get to the spacecraft[6]. Therefore we must introduce the times t_t, t_b and t_r of transmission, bounce and reception of the signal and compute each of the considered vectors at the adequate time. In particular, we have two different light-times,

[4]The time the light takes to reach the spacecraft and go back to Earth.

[5]In this modelization we assumed that the spacecraft center of mass and the antenna center of phase are coincident. In general - and in particular for Juno - this is not true, thus a vector $\mathbf{y}_{\mathrm{CoP}}$ should be added to $\mathbf{y}_{\mathrm{S/C}}$. The effect of such approximation will be described in Chapter 5.

[6]Since Jupiter is $\sim 5AU$ far from the Sun, during the Juno mission it will be from 4 to 6 AU far from the Earth, Δt thus varying from 33 to 50 minutes.

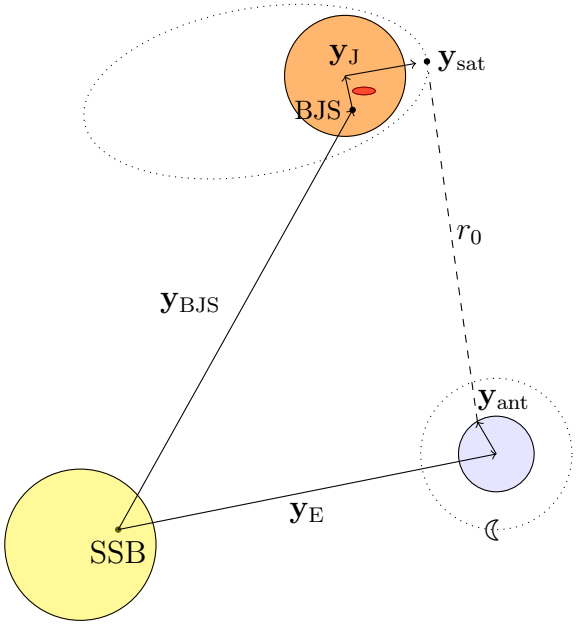

Figure 2.1: Scheme describing the positions of the bodies involved in the dynamics and showing the range in case of flat space-time and infinite speed of light.

the up-leg $\Delta t_{\rm up}$ and the down-leg $\Delta t_{\rm do}$, along with the up-leg and the down-leg distances:

$$r_{\rm up}(t_r) = \left|\mathbf{y}_{\rm BJS}(t_b) + \mathbf{y}_{\rm Jup}(t_b) + \mathbf{y}_{\rm S/C}(t_b) - \mathbf{y}_{\rm E}(t_t) - \mathbf{y}_{\rm ant}(t_t)\right| \tag{2.7}$$

$$r_{\rm do}(t_r) = \left|\mathbf{y}_{\rm BJS}(t_b) + \mathbf{y}_{\rm Jup}(t_b) + \mathbf{y}_{\rm S/C}(t_b) - \mathbf{y}_{\rm E}(t_r) - \mathbf{y}_{\rm ant}(t_r)\right|. \tag{2.8}$$

Usually the observable is labeled with the receive time t_r, thus the times t_b and t_t are unknown and must be calculated. The computation uses an iterative method which involves the previous relations and is described in detail in (Tommei et al., 2010) in the case of the BepiColombo orbiter around Mercury. Once t_t and t_b are known, the range is defined by average of the up-leg and the down-leg ranges,

$$r(t_r) := (r_{\rm up}(t_r) + r_{\rm do}(t_r))/2. \tag{2.9}$$

The computation of the range-rate is even more complicated, because it is necessary to take into account that t_t and t_b are function of t_r, defining implicit equations for $\dot{r}_{\rm up}$ and $\dot{r}_{\rm do}$. Similarly to what has to be done for the range, the instantaneous range-rate is defined as the average of the up-leg and the down-leg range-rate: $\dot{r}(t_r) := (\dot{r}_{\rm up}(t_r) + \dot{r}_{\rm do}(t_r))/2$.

In fact, the observation is not the instantaneous range-rate of the spacecraft. The actual observable is computed measuring the difference in phase between carrier

waves generated at the ground station and the one returned from the spacecraft, over some integration time Δ. Therefore it is a difference of range indeed:

$$\frac{r(t_b + \Delta/2) - r(t_b - \Delta/2)}{\Delta}, \tag{2.10}$$

or, equivalently, an integrated range-rate:

$$\frac{1}{\Delta}\int_{t_b-\frac{\Delta}{2}}^{t_b+\frac{\Delta}{2}} \dot{r}(s)ds. \tag{2.11}$$

By a numerical point of view, using (2.11) is preferable because it allows much more control of the rounding off problems, as it is described in ((Milani and Gronchi, 2010), Chapter 17). In Chapter 5 we will show in the special case of the Juno mission that this formulation is in fact more convenient.

2.2.2 Shapiro effect

In the previous section we neglected the fact that by General Relativity space-time is not flat. This means that the light path is not a straight line, rather some geodesics of the 4-dimensional manifold. The deviation from the straight-line propagation can be quantified with the Shapiro effect $S(\gamma)$ (cf. (Shapiro, 1964)), to be added to the down-leg and up-leg range (2.7) and (2.8). Here γ is the coefficient of the Parametrized Post-Newtonian (PPN) formalism related to the curvature of the space-time (cf. (Will, 1971)). It is known that such curvature is due to the presence of the bodies and their masses, in this case the planets and the satellites. Thus, the Shapiro effect is the sum of the terms due to each body.

Note that the Shapiro effect due to a spherical body is different from that of an oblate one. The difference between the two can be modeled as a term to be added to the monopole term S_0:

$$S(\gamma) = S_0(\gamma) + S_{J_2}(\gamma).$$

The term S_0 can be approximated as (cf. (Moyer, 2003)):

$$S_0(\gamma) = \frac{(1+\gamma)GM_P}{c^3}\ln\left[\frac{r_1 + r_2 + r_{12} + \frac{(1+\gamma)\mu}{c^2}}{r_1 + r_2 - r_{12} + \frac{(1+\gamma)\mu}{c^2}}\right],$$

and the term S_{J_2} is given to the order $1/c^2$ by (cf. (Klioner, 1991) and (Teyssandier and Le Poncin-Lafitte, 2008)):

$$\begin{aligned} S_{J_2}(\gamma) = &-\frac{1+\gamma}{2}\frac{GM}{c^2}J_2\frac{R_E}{r_1 r_2}\frac{r_{12}}{1+\mathbf{n}_1\cdot\mathbf{n}_2}\cdot \\ &\cdot\left[\left(\frac{1}{r_1}+\frac{1}{r_2}\right)\frac{(\mathbf{s}\cdot\mathbf{n}_1+\mathbf{s}\cdot\mathbf{n}_2)^2}{1+\mathbf{n}_1\cdot\mathbf{n}_2} - \frac{1-(\mathbf{s}\cdot\mathbf{n}_1)^2}{r_1} - \frac{1-(\mathbf{s}\cdot\mathbf{n}_2)^2}{r_2}\right]. \end{aligned}$$

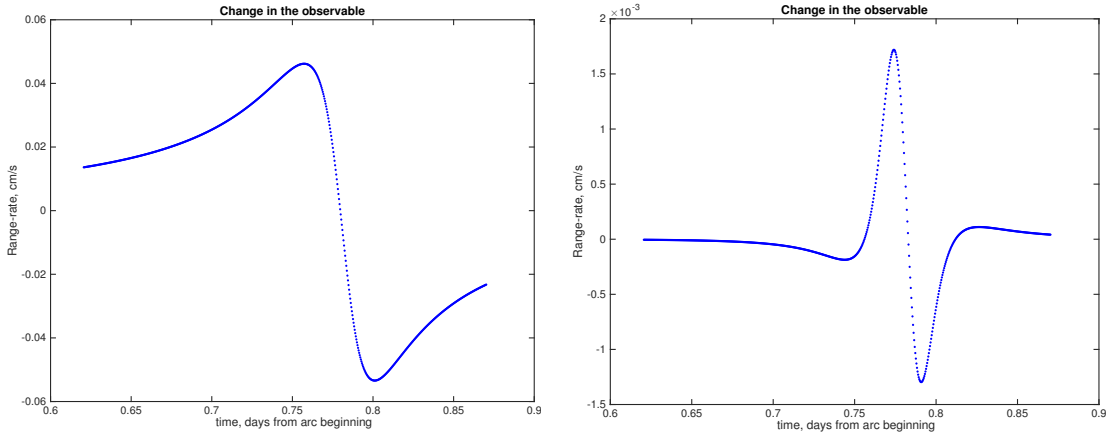

Figure 2.2: Signals on the range-rate observables from first pericenter pass due to the Shapiro effect induced by Jupiter (on the left) and the Shapiro effect due to Jupiter's oblateness only (on the right). The S/N is ~ 30 for $S(\gamma)$, whereas $S_{J_2}(\gamma)$ is of the order of noise.

In the previous formulae: M_P and R_E are the mass and the equatorial radius of the perturbing body[7]; if we indicate with $\mathbf{r}_1, \mathbf{r}_2$ the vectors originating in the central body's center of mass pointing respectively to the spacecraft and to the ground antenna on Earth, then $r_i = |\mathbf{r}_i|$ and $\mathbf{n}_i = \mathbf{r}_i/r_i$, $i = 1, 2$; $r_{12} = |\mathbf{r}_2 - \mathbf{r}_1|$; $\mathbf{s}$ is a unit vector along the spin axis of the perturbing body.
For the Shapiro effect on the range-rate, one differentiates the previous expressions with respect to time.

For the Radio Science experiment of the Juno mission, we included in the observables the contributions due to the Sun and Jupiter, which are not negligible: the first because of its large mass, the second for its proximity to the light path from the spacecraft to the ground antenna.

Fig. 2.2 shows the effect on the range-rate observables due to the light bending induced by Jupiter, the complete $S(\gamma)$, and the effect due to the light bending induced by Jupiter's oblateness, the term $S_{J_2}(\gamma)$ alone. The first effect is measurable, the S/N being ~ 30, the second is of the level of noise. We considered both in the computation of the observable. On the contrary, the signal on the range observables of $S_{J_2}(\gamma)$ is well below the level of noise and therefore we neglected it. As regards the oblateness term of the Sun, note that its magnitude with respect to the oblateness term of Jupiter is proportional to $(m_\odot J_{2\odot})/(m_{\rm Jup} J_{2\rm Jup}) = 10^{-2}$, thus it can be neglected as well.

[7] $R_E = 71492$ km (cf. (Williams, 2015)).

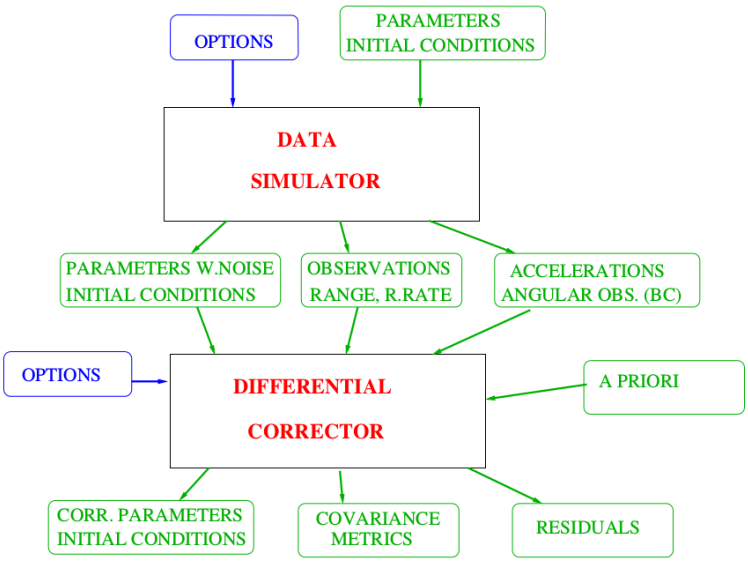

Figure 2.3: The block diagram of a simple simulator setup. The black rectangles indicate the main programs, the rectangles with smoothed corners the data structures.

2.3 ORBIT14

The Department of Mathematics of the University of Pisa, in collaboration with the spin-off SpaceDyS s.r.l. has designed and developed ORBIT14, a software able to perform the orbit determination and the parameter estimation for the missions BepiColombo (ESA) and Juno. In the following we describe shortly the structure of the software and focus on the dynamical modules and the relativistic corrections that have been included.

2.3.1 Software architecture in short

The structure of ORBIT14 is showed in Fig. 2.3. It is composed of two main programs, the *data simulator* and the *differential corrector*.
The latter solves the equation of motion computing the dynamics of the bodies involved, calculates the observables following what said in Section 2.2 and implements the non-linear least squares method performing the differential correction algorithm described in Section 2.1. The outcomes are the results of the parameter estimation, which is accompanied by the covariance analysis.
The data simulator responds to the necessity of using the differential corrector

before the mission starts, in order to assess whether the scientific goals could be reached. It simply produces a simulation of the observables that are given as input to the differential corrector.

2.3.2 Dynamics

The complexity of the software is in the computation of the observable and in the propagation of the dynamics. While we have addressed the first in Section 2.2, in the following we describe the dynamics considered for the Juno mission.

For the dynamics which have to be propagated by numerical integration we call a propagator which uses the corresponding dynamic module and solves the equation of motion for the requested time interval. The states (time, position, velocity, acceleration) are stored in a memory stack, from which interpolation is possible with the required accuracy. Then, when the state is needed to compute the observables, the dynamics stacks are consulted and interpolated by the propagator modules.

Reference systems and their realizations

In celestial mechanics the concept of reference system is crucial. A *reference system* is the complete specification of how a celestial coordinate system is to be formed, i.e. it is defined by a point - the *origin* - and three orthogonal axes. A *reference frame*, or *realization* of the reference system, is specified by a set of points in the sky along with their coordinates, which allow the practical realization of the reference system.

The following reference systems - and the relative realizations - are used in the software ORBIT14. The rigorous definitions can be found in the corresponding papers; for a divulgative yet detailed and technically coherent description, see (IERS, 2016).

- **International Celestial Reference System** (ICRS): an ideally inertial reference system with the Earth mean equator at epoch J2000 as fundamental plane; the origin is the Barycenter of the Solar System, the x axis points in the direction of the mean equinox of J2000 and the pole is given by the direction of the z axis. The realization of ICRS is called International Celestial Reference Frame (ICRF) and in this thesis will be indicated with Σ_{ICRF} (cf. (Ma and Feissel, 1997)).
- **International Terrestrial Reference System** (ITRS): an Earth-fixed reference system centered at the geocenter (center of the whole Earth system)

whose x and y axis are in the plane of the true equator at date, with the condition that there is no residual rotation with respect to the Earth surface. The realization of the ITRS is the International Terrestrial Reference Frame (ITRF) and in this thesis will be indicated with Σ_{ITRF} (cf. (Petit and Luzum, 2010), Chapter 4).

- **Ecliptic Celestial Reference System of J2000** (ECRS): an ideally inertial reference system with the Earth ecliptic at epoch J2000 as fundamental plane; the origin is the Barycenter of the Solar System, the x axis points in the direction of the mean equinox of J2000 and the pole is the point on the celestial sphere in the direction of the z axis[8] (cf. (Dehant and Mathews, 2015), Chapter 3). The realization of ECRS, the ECRF, will be indicated with Σ_{ECRF}.

- **Jupiter Equatorial**: a conventional inertial reference system centered at Jupiter's barycenter, whose fundamental plane is Jupiter's equator; its definition can be found in the 2009 Report of the IAU Working Group on Cartographic Coordinates and Rotational Elements (Archinal et al., 2011). It will be indicated with Σ_{EQ}.

- **Jupiter body-fixed**: a Jupiter-fixed reference system, rotating with Jupiter, whose fundamental plane is Jupiter's equator; if Σ_{BF} is such reference system, the transformation mapping Σ_{EQ} to Σ_{BF} is a rotation, whose expression in coordinates will be given in Section 4.2.

In 2000, the IAU General Assemby defined a system of space-time coordinates for the Solar System, within the framework of the General Relativity (cf. (Rickman, 2001)), called Barycentric Celestial Reference System (BCRS). Later in 2006, the IAU General Assembly established that *"for all practical applications, [...] the BCRS is assumed to be oriented according to the ICRS axes"*. Thus, whenever in this work we speak of BCRS, the previous statement will be implicitly considered.

Dynamics of the spacecraft

The dynamics of the orbiter is integrated numerically in the reference system Σ_{EQ}. Its equation of motion contains:

- the gravitational attraction of Jupiter, expressed through spherical harmonics expansion (see Section 3.1);

[8] The ECRS is obtained from the ICRS by a rotation about the x axis of angle $\epsilon_0 = 23°26'21''.406$ (cf. (Petit and Luzum, 2010)), the mean obliquity of the Earth.

- the non-gravitational perturbations, including direct radiation pressure, pressure from radiation reflected and emitted by Jupiter, thermal emission;
- solar and planetary differential attractions;
- Jupiter's satellites differential attractions and tidal perturbations (see Sections 3.5.1 and 3.5.2)
- relativistic corrections (a term due to the use of a Jupiter Dynamical Time - see Section 2.3.3 - a term due to the mass of Jupiter and the Lense-Thirring effect - see Section 4.1).

Dynamics of Barycenter of the Jovian System

The dynamics of BJS is integrated numerically in Σ_{ECRF}, which gives the possibility to include its initial conditions in the vector of solve-for parameters. The equation of motion for BJS contains the following perturbations:

- the Newtonian attraction from the Sun and the planets;
- the relativistic PPN corrections, including the PN parameters γ, β and the Sun's dynamic oblateness;
- the effect of the Galilean satellites on the motion of BJS, expressed by the Jupiter-satellite-Sun Roy-Walker parameters[9] (cf. (Milani and Gronchi, 2010), Chapter 4).

Rotation of Jupiter and of the Earth

For the rotation of Jupiter, we use a semi-empirical model, containing parameters defining the model of Jupiter's rotation, see Section 4.2.

For the Earth, we are using the interpolation tables made public by the IERS, because we can by no means solve for the Earth rotation parameters from observations at Jupiter at accuracies competitive with other available measurements. The same argument applies to the station coordinates: we assume they are supplied by the ground station with the required accuracy, including corrections for the antenna motion.

[9]Such perturbations are actually detectable only using range measurements; since Juno will supply ranging only in the X-band, their relevance to our scope is limited. Future missions to the satellites will have to consider such perturbations.

Dynamics of other bodies

The current state, as a function of time, of the planets Mercury to Neptune (excluding Jupiter and considering also Pluto) are read from the Jet Propulsion Laboratory (JPL) ephemerides (currently the DE421 version, cf. Folkner et al. (2009)) as Chebychev polynomials, which are interpolated with the JPL algorithm. For Jupiter satellites the ephemerides are provided by JPL in the form of SPICE kernels (cf. Jacobson (2003)): the SPICE software has been linked and suitable interfaces have been implemented in the code.

We need also to take into account asteroid perturbations on the orbit of the BJS. The software to generate asteroid ephemerides interpolation tables is available, and the interface has been built, to be used with as many asteroids as needed. At the moment, for consistency with DE421 we use the perturbations from 343 asteroids, each one with a mass as assigned by the ephemerides.

2.3.3 Time ephemerides and reference systems

A correct relativistic formulation[10] of the observable must consider that with different reference systems are associated different time coordinates, and the conversion between them must be handled properly.

The vectors in (2.6) must be converted to a common space-time reference system in order to perform the sums. It is conventional to choose some realization of BCRS: we adopt the so-called Solar System Barycentric (SSB) realization, in which the time coordinate is a redefinition of the Barycentric Dynamic Time (TDB) (cf. IAU 2006 Resolution B3, (van der Hucht, 2008)). All the other possible choices for such time coordinate differ from TDB by linear scaling.

For all the practical issues on Earth the time scale of reference is the Terrestrial Dynamical Time (TDT or TT), whose definition is based on averages of clock and frequency measurements on the Earth surface. The other time scales realizing TT differ by some time offset (TAI, UTC or GPS time).

When coping with an orbiter around a planet, its equation of motion can be approximated with a Newtonian equation provided that the independent variable is the proper time T of the planet. As described in (Milani et al., 2010) in the case of Mercury and in (Tommei et al., 2015) in the case of Jupiter, it is necessary to define a new time coordinate whose relationship with TDB time t, truncated to

[10] By "correct" we mean "that takes into account all the measurable effects".

1-PN order[11], is given by the differential equation

$$\frac{dT}{dt} = 1 - \frac{1}{c^2}\left[U + \frac{v^2}{2} - L\right], \tag{2.12}$$

where U is the gravitational potential of the contributing bodies[12] at the center of the planet, v is the SSB velocity of the planet and L is a constant used to perform the conventional rescaling motivated by removal of secular terms, e.g. for the Earth, L is $L_{\rm C} = 1.48082686741 \times 10^{-8}$ (cf. (Irwin and Fukushima, 1999)). For Jupiter, we call this time Jupiter Dynamical Time (TDJ).

The previous can be solved by a quadrature formula, provided we know the orbits of the Sun and the planets (by numerical integration or by JPL ephemerides). ORBIT14 implements a Gaussian quadrature formula to generate an interpolation table for the conversion from TDB to TDT, TDJ. This table is pre-computed by a separate main program and it can be read by all other programs: a suitable module uses the interpolation to compute all conversions of time coordinates, that is it implements an internal system of time ephemerides.

Going back to the transformation of the vectors in (2.6) to SSB, they involve essentially the geocentric position of the antenna $\mathbf{y}_{\rm ant}$ and the position of the orbiter $\mathbf{y}_{\rm S/C}$. The former must be converted to SSB from the geocentric frame and the latter from the jovicentric equatorial system. We report here the transformation of the spacecraft state; the reader is referred to (Tommei et al., 2015) for the others. The position and the velocity of the Juno spacecraft from the jovicentric frame to the SSB frame are given by

$$\begin{aligned}
\mathbf{y}^{\rm TB}_{\rm S/C} &= \mathbf{y}^{\rm TJ}_{\rm S/C}\left(1 - \frac{U}{c^2} - L_{\rm CJ}\right) - \frac{1}{2}\left(\frac{\mathbf{v}^{\rm TB}_{\rm M}\cdot\mathbf{y}^{\rm TJ}_{\rm S/C}}{c^2}\right)\mathbf{v}^{\rm TB}_{\rm M} \\
\mathbf{v}^{\rm TB}_{\rm S/C} &= \left[\mathbf{v}^{\rm TJ}_{\rm S/C}\left(1 - \frac{U}{c^2} - L_{\rm CJ}\right) - \frac{1}{2}\left(\frac{\mathbf{v}^{\rm TB}_{\rm M}\cdot\mathbf{v}^{\rm TJ}_{\rm S/C}}{c^2}\right)\mathbf{v}^{\rm TB}_{\rm M}\right]\cdot\left[\frac{dT}{dt}\right],
\end{aligned}$$

where dT/dt is the transformation of the local time T at the planet (TDJ) to the SSB time t given by (2.12) and $L_{\rm CJ}$ is the constant to remove the secular terms. We believe that we do not need to do this, since a very simple iterative scheme is very efficient in providing the inverse time transformation. Thus, as described in (Tommei et al., 2015), we set $L_{\rm CJ} = 0$.

[11] Although the $O(c^{-4})$ terms are known, we do not need to include them because their contribution is below the accuracy level of the experiment.

[12] The list depends on the accuracy required: we included the Sun, Mercury to Neptune, the Moon.

CHAPTER 3

Determination of the gravity field

Contents

Outline: As discussed in Section 1.3, the Gravity Science experiment of the mission Juno is aimed at determining Jupiter's gravity field. This chapter is dedicated to this problem. Firstly, we give the mathematical definition of gravitational potential, introducing the classical spherical harmonics expansion and recalling its

properties. Then we present a semi-analytical method for determining the formal uncertainty of the gravity field of a generic planet and apply it to the Juno-Jupiter case. Our discussion will focus on the results of full numerical simulations conducted with Orbit14 regarding Jupiter's gravity field. Not only do we analyze the accuracies available using the spherical harmonics model, we also introduce a local model for the gravity field of Jupiter, the *ring mascons* model, useful for describing high-frequency components of the gravity field.

3.1 The gravity field of a planet

Let us consider an extended body A and a reference system $\Sigma = O\hat{\mathbf{e}}_1\hat{\mathbf{e}}_2\hat{\mathbf{e}}_3$. The *gravitational potential* of an extended body A of density ρ is a real-valued function $U\colon \mathbb{R}^3 \to \mathbb{R}$ defined as

$$U(\mathbf{p}) = \int_A \frac{G\rho(\mathbf{p}')}{|\mathbf{p}-\mathbf{p}'|}\mathrm{d}\mathbf{p}'.$$

The *gravity field* of A is its gradient, $\operatorname{grad} U$. It is a well-known fact that U is harmonic on $\mathbb{R}^3 \setminus A$ (cf. (Heine, 1861)), therefore it can be expanded in series of spherical harmonics[1]. Using spherical coordinates (r, θ, λ) with respect to Σ, such expansion reads

$$U(r,\theta,\lambda) = \frac{GM}{r} + \sum_{\ell=1}^{\infty}\sum_{m=0}^{\ell} U_{\ell m}(r,\theta,\lambda), \tag{3.1}$$

where

$$U_{\ell m}(r,\theta,\lambda) = \frac{GM}{r}P_{\ell m}(\sin\theta)\frac{R^\ell}{r^\ell}[C_{\ell m}\cos(m\lambda) + S_{\ell m}\sin(m\lambda)].$$

Here $P_{\ell m}$ is *Legendre's associated function* of *degree* ℓ and *order* m, R is the radius of an open ball strictly containing A, $C_{\ell m}, S_{\ell m}$ are the *spherical harmonics coefficients*. We distinguish the *zonal* coefficients ($C_{\ell m},\ m = 0$) from the *tesseral* coefficients ($C_{\ell m}, S_{\ell m},\ 0 < m < \ell$) and the *sectorial* coefficients ($C_{\ell m}, S_{\ell m}, m = \ell$). The *gravitational momentum* of degree ℓ is $J_\ell := -C_{\ell 0}$.

Let us remark that since O is exactly the planet's center of mass, then the degree-1 coefficients C_{10}, S_{11}, C_{11} are necessarily zero (cf. (Milani and Gronchi, 2010), ch.13).

The functions $Y_{\ell m1} := P_{\ell m}(\sin\theta)\cos(m\lambda)$ and $Y_{\ell m0} := P_{\ell m}(\sin\theta)\sin(m\lambda)$ are called *spherical harmonics*. We can normalize the spherical harmonics with respect to

[1] For a detailed description of how to obtain the expansion, see (Kaula, 1966).

the scalar product

$$\langle f, g\rangle := \frac{1}{4\pi}\int_{S^2} fg\ dS$$

of $L^2(S^2)$, the space of the square-integrable functions on the sphere:

$$\overline{Y}_{\ell mi} = \frac{Y_{\ell mi}}{\sqrt{\langle Y_{\ell mi}, Y_{\ell mi}\rangle}} = \sqrt{\frac{(2-\delta_{0m})(2\ell+1)(\ell-m)!}{(\ell+m)!}} = H_{\ell m}Y_{\ell mi}.$$

The normalized harmonic coefficients are then $\overline{C}_{\ell m} = C_{\ell m}/H_{\ell m}$ and $\overline{S}_{\ell m} = S_{\ell m}/H_{\ell m}$. With the new notation, the gravitational potential (3.1) reads

$$U(r,\theta,\lambda) = \frac{GM}{r}\sum_{\ell=0}^{\infty}\frac{R^\ell}{r^\ell}\sum_{m=0}^{\ell}[\overline{C}_{\ell m}\overline{Y}_{\ell m1} + \overline{S}_{\ell m}\overline{Y}_{\ell m0}].$$

Using normalized spherical harmonics is particularly convenient in numerical applications, since their magnitude $1/H_{\ell m}$ is fast-growing as ℓ increases.

If we use the spherical harmonic expansion to model the gravity field of a planet, then in order to measure it via orbit determination, it is sufficient to determine the harmonic coefficients $C_{\ell m}, S_{\ell m}$. Of course, the (3.1) needs to be truncated at a suitable degree $\ell_{\max}$, which can be established for example by the rule

$$\ell_{\max} = \pi\frac{R}{h},$$

where h is the altitude of the spacecraft with respect the surface of the planet (cf. (Milani and Gronchi, 2010), ch. 16).

3.2 A semianalytical method

During the phase of design of a space mission, it is essential to set the mission parameters so that all the scientific requirements can be met. Usually the scientific goals are limited by external factors, such as the environmental conditions. For example, in the case of an orbiter around a planet, the choice of the orbit of the probe should provide enough coverage of the surface of the planet as well as ensure protection from the magnetic field and/or the high temperatures. Finding the best match between science and mission design requires several simulations. In the case of the gravimetry experiment, the best way to have a global and complete overview of the results achievable is by performing a complete orbit determination and parameter estimation simulation, of course.

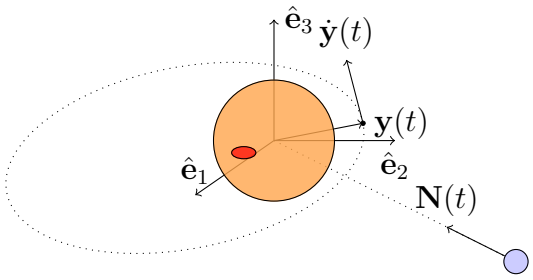

Figure 3.1: The frame $O\hat{\mathbf{e}}_1\hat{\mathbf{e}}_2\hat{\mathbf{e}}_3$, the spacecraft position and velocity $\mathbf{y}(t), \dot{\mathbf{y}}(t)$ and the direction Earth-Jupiter $\mathbf{N}(t)$. The vectors $\hat{\mathbf{e}}_1, \hat{\mathbf{e}}_2$ span the equatorial plane of the planet, the vector $\hat{\mathbf{e}}_3$ is parallel to its rotation axis. The picture is not in scale.

In this section we present a semi-analytical theory for estimating the accuracy in the determination of the gravity field of a target planet. Such a theoretical study can be easily implemented numerically and used in practice to obtain preliminary results exclusively about the gravimetry experiment of a given space mission. We also describe how to map the computed uncertainties on the gravity field to the surface of the planet in order to obtain an estimation of the gravity anomalies uncertainties. This indicates also the regions of the planet in which the gravity field is better recovered.

3.2.1 Axially symmetric planet

In first approximation we consider the case of an axially symmetric planet, leaving the general case to Section 3.2.3.

Let us then consider a planet of mass M, equatorial radius R and symmetric with respect to the z-axis of an inertial frame $O\hat{\mathbf{e}}_1\hat{\mathbf{e}}_2\hat{\mathbf{e}}_3$ of coordinates xyz, with origin in the center of mass of the planet, such that the xy plane is the equatorial plane of the planet (see Fig. 3.1).
The gravitational potential U of the planet is then function only of the latitude θ and the distance r from the center of mass. Thus, the expansion in spherical harmonics (3.1) contains only zonal coefficients:

$$U = \frac{GM}{r} + \sum_{\ell=2}^{\infty} U_{\ell 0}, \quad \text{where} \quad U_{\ell 0} = \frac{GM}{r} C_{\ell 0} \left(\frac{R}{r}\right)^{\ell} P_\ell(\sin\theta).$$

Let $\ell_{\max} > 2$ be an integer. We want to study the uncertainty in the determination of the zonal harmonic coefficients $C_{2\ 0}, \ldots, C_{\ell_{\max} 0}$. The main idea is to find an

analytical expression for the elements of the normal matrix C in order to compute the covariance matrix and use (2.4).

Let us start defining a proper prediction function. Let $(t_i, \dot{r}_i)_{i=1,\dots,m}$ be observations of the spacecraft, where $\dot{r}_i$ is the range-rate of the probe orbiting the planet[2]. Let $\mathbf{y}(t)$ be the cartesian coordinates of the spacecraft with respect to the planet at time t and $\dot{\mathbf{y}}(t)$ its velocity. Let us truncate the spherical harmonic expansion of U at degree $\ell_{\max}$. Note that by the principle of linearity of the first order perturbations, we have, at the first order,

$$\dot{\mathbf{y}} = \mathbf{v} + \Delta\mathbf{v} = \mathbf{v} + \sum_{\ell=2}^{\ell_{\max}} \Delta\mathbf{v}^{(\ell)} \tag{3.2}$$

where $\mathbf{v}$ is the component of the velocity due to the monopole $U_0 := GM/r$ and $\Delta\mathbf{v}^{(\ell)}$ is the first order component due to the correction $U_{\ell 0}$.

If we denote with $\mathbf{N}(t)$ the opposite of the unit vector centered at the planet and pointing at the center of the Earth, we can define our prediction function as

$$\dot{r}(t) := [\dot{\mathbf{y}}(t) + \mathbf{w}(t)] \cdot \mathbf{N}(t),$$

where $\mathbf{w}(t)$ is a function of the time accounting, among the others, for the dynamics of the Earth and the planet; in particular it does not depend on the gravity of the planet. The residuals are

$$\xi_i = \dot{r}_i - \dot{r}(t_i) = v_i - \dot{\mathbf{y}}(t_i) \cdot \mathbf{N}(t_i) - \mathbf{w}(t_i) \cdot \mathbf{N}(t), \quad i = 1, \dots, m. \tag{3.3}$$

Since $\mathbf{w}$ does not depend on the harmonic coefficients of the planet, it does not affect the uncertainty of the gravity field and can be considered perfectly known.

The following remark is crucial. For an unperturbed orbit, the energy (per unit of mass)

$$E := \frac{1}{2}|\mathbf{v}|^2 - U_0$$

is an integral of motion. Perturbing the gravitational potential with a term $U_{\ell 0}$, the function

$$E_\ell := \frac{1}{2}\left|\mathbf{v} + \Delta\mathbf{v}^{(\ell)}\right|^2 - (U_0 + U_{\ell 0})$$

is still an integral of motion, equal to E. Thus

$$\frac{1}{2}|\mathbf{v}|^2 - U_0 = \frac{1}{2}\left|\mathbf{v} + \Delta\mathbf{v}^{(\ell)}\right|^2 - (U_0 + U_{\ell 0})$$

[2]The notation follows the same used in Chapter 2: the dot here is purely notational, not indicating an actual derivative. The same holds later, when we define the prediction function.

and, neglecting second order terms,

$$\mathbf{v} \cdot \Delta\mathbf{v}^{(\ell)} = U_{\ell 0}, \quad \ell \geq 2.$$

In fact, the transversal component of $\Delta\mathbf{v}^{(\ell)}$ with respect to $\mathbf{v}$ can be neglected because the main effect is given by the parallel one, the effect being quadratic in time. Therefore we rewrite the previous equation as

$$|\mathbf{v}| \left|\Delta\mathbf{v}^{(\ell)}\right| = U_{\ell 0}, \quad \ell \geq 2. \tag{3.4}$$

In conclusion, a measurement of the range-rate of the spacecraft gives a direct measurement of the potential of the planet.

Combining (3.2) and (3.3), if φ_i is the angle between the vectors $\dot{\mathbf{x}}(t_i)$ and $\mathbf{N}(t_i)$, the residual assumes the expression

$$\xi_i = v_i - (|\mathbf{v}(t_i)| \cos\varphi_i + \sum_{\ell=2}^{\ell_{\max}} \left|\Delta\mathbf{v}^{(\ell)}(t_i)\right| \cos\varphi_i) - w(t_i). \tag{3.5}$$

If $\mathbf{x} := (C_{\ell+1\,0})_{\ell=1,\ldots,\ell_{\max}-1} \in \mathbb{R}^N$ is the vector of the solve-for parameters, we obtain from (3.4) and (3.5) that the design matrix $B = (b_{i\ell}) \in \mathbb{R}^{m\times N}$ has elements

$$b_{i\ell} = \frac{\partial \xi_i}{\partial x_\ell} = -\frac{GM}{r_i}\left(\frac{R}{r_i}\right)^{\ell+1} \frac{P_{\ell+1}(\sin\theta_i)}{|\mathbf{v}_i|} \cos\varphi_i \tag{3.6}$$

where the subscript i indicates the evaluation in t_i.

Now it is straightforward to compute the normal matrix $C := B^T W B = (c_{jk}) \in \mathbb{R}^{N\times N}$. Choosing $W = \sigma^{-2} I$ as weight matrix[3], it immediately follows from (4.2) that

$$c_{jk} = \sum_{i=1}^{N} \sigma^{-2} b_{ij} b_{ik} = \sum_{i=1}^{N} \frac{(GM)^2 R^{j+k+2}}{r_i^{j+k+3}} \frac{P_{j+1}(\sin\theta_i) P_{k+1}(\sin\theta_i)}{\sigma^2 |\mathbf{v}_i|^2} \cos^2\varphi_i.$$

It is possible to compute numerically the inverse of C and use (2.4) to compute the formal uncertainty of the spherical harmonic coefficients $C_{\ell 0},\ \ell = 2, \ldots, \ell_{\max}$.

3.2.2 Surface gravity anomalies uncertainties

We define a gravity anomaly as the difference between the real value of the gravity acceleration and the value due to the monopole term. We can predict the uncertainty of the gravity anomalies at the surface of the planet using the principal components analysis of the covariance matrix computed in section 3.2.1.

[3]That is, we use a uniform weight $1/\sigma^2$. Such weight is usually assumed equal to the inverse of the square of the RMS of the observables, in this case the range-rate.

Let $\lambda_1 > \lambda_2 > \cdots > \lambda_N > 0$ be the eigenvalues of the covariance matrix Γ and let $V^{(i)} = (V_\ell^{(i)})_\ell,\ i = 1, \ldots, N$ be respective unit eigenvectors. It is a known fact that $\sqrt{\lambda_i}V^{(i)}$ is the i-th semiaxis of the 1-sigma confidence ellipsoid (cf. Milani and Gronchi (2010), ch. 5), thus its entries belong to the space of the parameters and are zonal harmonics coefficients. Consequently, each eigenvector $V^{(i)}$ can be mapped onto the following function:

$$U^{(i)}(r, \theta) := \frac{GM}{r} \sum_{\ell=2}^{\ell_{\max}} \sqrt{\lambda_i} V_{\ell-1}^{(i)} \left(\frac{R}{r}\right)^\ell P_\ell(\sin\theta). \tag{3.7}$$

The function $U^{(i)}$ represents the contribute of the i-th semiaxis of the confidence ellipsoid to the uncertainty of the non-spherical part of the gravitational potential. In other words, it is the uncertainty of the gravitational potential in the direction of the i-th semiaxis. To obtain the uncertainty of the gravity anomalies at the surface, one simply takes the derivative with respect to r of (3.7)

$$\frac{\partial U^{(i)}}{\partial r}(r, \theta) = -\frac{GM}{r^2} \sum_{\ell=2}^{\ell_{\max}} (\ell + 1) \sqrt{\lambda_i} V_{\ell-1}^{(i)} \left(\frac{R}{r}\right)^\ell P_\ell(\sin\theta)$$

and evaluates it at the surface $r = R$:

$$\mathcal{U}^{(i)}(\theta) := \frac{\partial U^{(i)}}{\partial r}(R, \theta) = -\frac{GM}{R^2} \sum_{\ell=2}^{\ell_{\max}} (\ell + 1) \sqrt{\lambda_i} V_{\ell-1}^{(i)} P_\ell(\sin\theta). \tag{3.8}$$

The latter gives the uncertainty of the gravity anomalies on the surface of the planet due to the i-th semiaxis of the confidence ellipsoid.

We use the root mean square of the $\mathcal{U}^{(i)}$ to have a representation of the surface acceleration uncertainty which takes into account the contributes of all the semiaxis:

$$\mathcal{U}(\theta) := \sqrt{\frac{\sum_{i=1}^N (\mathcal{U}^{(i)}(\theta))^2}{N}}. \tag{3.9}$$

If the magnitude of some $\mathcal{U}^{(i)}$ is negligible with respect to the others, we can choose not to consider it in the sum (3.9).

Note that the unit eigenvector relative to a certain eigenvalue is not unique: if $\mathbf{u}$ is such a vector, then also $-\mathbf{u}$ is. This causes an ambiguity in the definition of $U^{(i)}$, as it is defined except for the sign. This is not important as we are interested in $\mathcal{U}$, where only the square of $\mathcal{U}^{(i)}$ appears, thus eliminating the ambiguity.

3.2.3 Effect of tesseral harmonics

In this section we consider the case of a planet with no symmetries. Following the same argument of Section 3.2.1, we show that the uncertainty of the zonal harmonic coefficients is influenced by the presence of the tesseral and sectorial coefficients and is larger than in the axially symmetric case.

Repeating the same calculations of and using the same notation as in Section 3.2.1, we obtain immediately that

$$\dot{\mathbf{y}} = \mathbf{v} + \Delta\mathbf{v} = \mathbf{v} + \sum_{\ell,m} \Delta\mathbf{v}^{(\ell,m)},$$

where $\Delta\mathbf{v}^{(\ell,m)}$ is the component due to the correction $U_{\ell m}$ and

$$|\mathbf{v}| \left|\Delta\mathbf{v}^{(\ell,m)}\right| = U_{\ell m} \quad \text{for all } \ell \geq 2,\ m = 0, \ldots, \ell. \tag{3.10}$$

Hence the residual is

$$\xi_i = v_i - (|\mathbf{v}(t_i)| \cos\varphi_i + \sum_{\ell,m} \left|\Delta\mathbf{v}^{(\ell,m)}(t_i)\right| \cos\varphi_i) - w(t_i). \tag{3.11}$$

Even if we want to study the uncertainty in the computation of the first $\ell_{\max}$ zonal harmonic coefficients, the presence of the tesseral and sectorial coefficients cannot be ignored. If $\boldsymbol{\mu} \in \mathbb{R}^N$, $N := (\ell_{\max}+1)^2 - 4$, is the vector of the solve-for parameters made up of all the harmonic coefficients up to degree $\ell_{\max}$, the design matrix $B = (\partial\xi_i/\partial\mu_j) \in \mathbb{R}^{m\times N}$ has elements:

$$\frac{\partial\xi_i}{\partial C_{\ell m}} = -\frac{GMR^\ell}{r_i^{\ell+1}} \frac{P_{\ell m}(\sin\theta_i)}{|\mathbf{v}_i|} \cos(m\lambda_i)\cos(\varphi_i), \tag{3.12}$$

$$\frac{\partial\xi_i}{\partial S_{\ell m}} = -\frac{GMR^\ell}{r_i^{\ell+1}} \frac{P_{\ell m}(\sin\theta_i)}{|\mathbf{v}_i|} \sin(m\lambda_i)\cos(\varphi_i), \tag{3.13}$$

where the subscript i indicates the evaluation in t_i.

By reordering the entries of the vector $\boldsymbol{\mu}$, we can suppose that $\boldsymbol{\mu} = (\mathbf{z}; \mathbf{w})$, where $\mathbf{z}$ is the subvector of the zonal harmonic coefficients and $\mathbf{w}$ is the subvector of the other harmonic coefficients. With this notation, the normal matrix C and the covariance matrix Γ have the block structure

$$C = \begin{pmatrix} C_{\mathbf{zz}} & C_{\mathbf{zw}} \\ C_{\mathbf{wz}} & C_{\mathbf{ww}} \end{pmatrix}, \quad \Gamma = \begin{pmatrix} \Gamma_{\mathbf{zz}} & \Gamma_{\mathbf{zw}} \\ \Gamma_{\mathbf{wz}} & \Gamma_{\mathbf{ww}} \end{pmatrix}, \tag{3.14}$$

where:

- the submatrices $\Gamma_{\mathbf{zw}} = \Gamma_{\mathbf{wz}}^T$ contain information about the correlations among zonal and non-zonal coefficients;
- the submatrix $C_{\mathbf{zz}}$ is the normal matrix of the fit obtained by choosing $\mathbf{z}$ as vector of the fit parameters and moving $\mathbf{w}$ into the consider parameters, thus it is the same normal matrix obtained in section 3.2.1.

The uncertainty of the zonal coefficients, considering correlations with tesseral coefficients, is given by definition by the square root of the diagonal of $\Gamma_{\mathbf{zz}}$. Note that the matrices $\Gamma_{\mathbf{zz}}$ and $C_{\mathbf{zz}}^{-1}$ are in general different. It is possible to define an order relation between positive definite matrices - using their interpretation as quadratic forms - and show that $\Gamma_{\mathbf{zz}} \geq C_{\mathbf{zz}}^{-1}$: given two positive definite matrices $A, B \in \mathbb{R}^{n\times n}$, we say that $A \geq B$ if $\mathbf{x}^T A\mathbf{x} \geq \mathbf{x}^T B\mathbf{x}$ for all vectors $\mathbf{x} \in \mathbb{R}^n$. The inequality can be proven using the following known formula (cf. Milani and Gronchi (2010), Chapter 5):

$$\Gamma_{\mathbf{zz}} = (C_{\mathbf{zz}} - C_{\mathbf{zw}} C_{\mathbf{ww}}^{-1} C_{\mathbf{wz}})^{-1}.$$

As a consequence, we have that the uncertainty of the coefficient $C_{\ell 0}$ when considering non-zonal coefficients is always higher than the uncertainty of the same coefficient in the axially symmetric case.

3.2.4 Test on the Juno mission

In this section we apply the theory developed in the previous section to the Juno mission.

Implementation of the algorithm

We implemented the theory described in section 3.2 in a MATLAB function called `uncertainties`. The user is invited to specify a value for the $\ell_{\max}$, the highest degree in the truncation of the spherical harmonics series of Jupiter's potential U, and to provide a file with a simulation of the spacecraft orbit around the planet. The data set is required to be composed of cartesian coordinates of the positions and velocities of the spacecraft $\mathbf{y}(t_i),\ \dot{\mathbf{y}}(t_i),\ i = 1, \ldots, m$ and unit vectors $\mathbf{N}(t_i)$ centered at the planet pointing at the Earth, all referred to a planet equatorial reference frame.

The algorithm converts the observations to spherical coordinates and computes the design matrix B using (4.2), in a form that uses normalized spherical harmonics, for numerical stability (cf. Milani and Gronchi (2010), ch. 13). Therefore, the

code gives as result the uncertainties of the normalized zonal harmonic coefficients $\overline{C}_{\ell 0} = \sqrt{2\ell+1} C_{\ell 0}$.

The weight matrix W is defined as a multiple of the identity matrix, $W = \sigma^{-2} I$. The constant factor σ is chosen as the standard deviation of the two-way Doppler observables of the spacecraft, possibly rescaled in order to take into account the difference between the integration time and the sampling time of the orbit. The uncertainties of the normalized zonal harmonic coefficients is given by (2.4).

The principal components analysis is performed as described in Section 3.2.2. The program computes the eigenvalues of the covariance matrix Γ and provides, upon request of the user, a comparison between the first principal component and any other component. Then the user can decide how many components should be included in the computation of (3.9). Normalized Legendre polynomials $\overline{P}_\ell$ are used for the principal components analysis, too.

Formal errors

In order to stress the fact that the accuracy of the estimated gravity field depends on the surface coverage, we compare the uncertainties obtained with a complete mission to those obtained with a single arc, namely the first Juno orbit dedicated to GS. We set $\ell_{\max} = 30$, that is we compute the uncertainty of the normalized zonal harmonic coefficients $C_{2\,0}, \ldots, C_{30\,0}$. The standard deviation $\sigma = 3\mu\mathrm{m}/s$ for 1000 sec integration time is assumed for the two-way Doppler measurements. The simulation of the orbit of the spacecraft is provided by the Data Simulator Program of the Orbit14 orbit determination software (cf. Section 2.3).

Fig. 3.2 shows the uncertainty of the normalized zonal harmonic coefficients $\overline{C}_{\ell 0}$ in the one-arc and the full mission cases. We trivially remark that the formal error is minor for the latter, since more observations result in more accuracy. It is interesting to remark that the uncertainties do not always increase with the harmonic degree: they reach the maximum value at degree 23, then they start decreasing. This increase in the uncertainty is due to the well-known fact that each zonal coefficient is highly correlated to the two following ones. On the other hand, truncating the spherical harmonics series at degree $\ell_{\max} = 30$ prevents from taking into account the correlations of the coefficients $C_{\ell 0},\ \ell = 23, \ldots, 30$ with the coefficients $C_{\ell 0},\ \ell \geq 30$, thus causing a decreasing in the uncertainty. This "hump" behaviour does not depend on the particular value of $\ell_{\max}$, but it disappears for small values of $\ell_{\max}$.

When we take into account the effect of the tesseral coefficients, the analysis can be done only with the datas coming from all the GS orbits, otherwise the solve-for

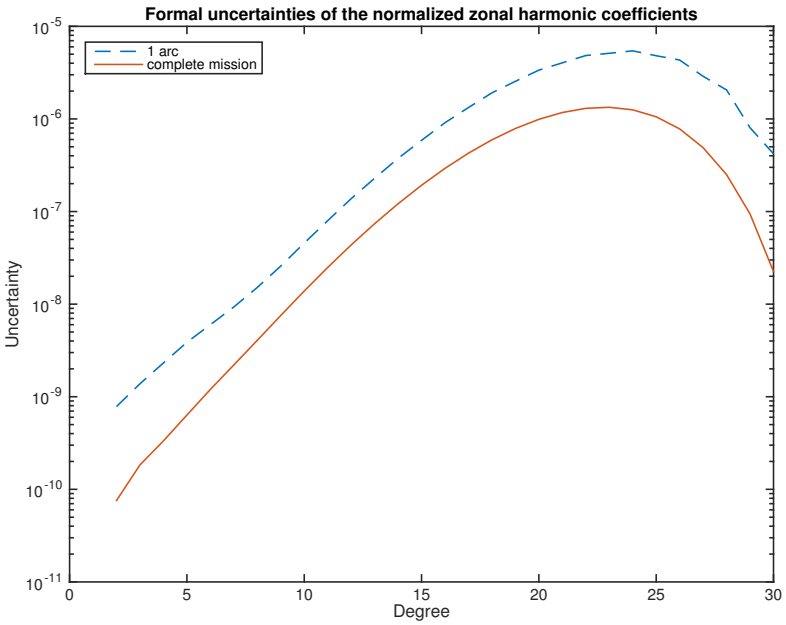

Figure 3.2: Comparison of the formal errors of the first 30 zonal harmonic coefficients of Jupiter's gravitational potential computed using one pericenter pass and a full mission. Semilogarithmic scale is used.

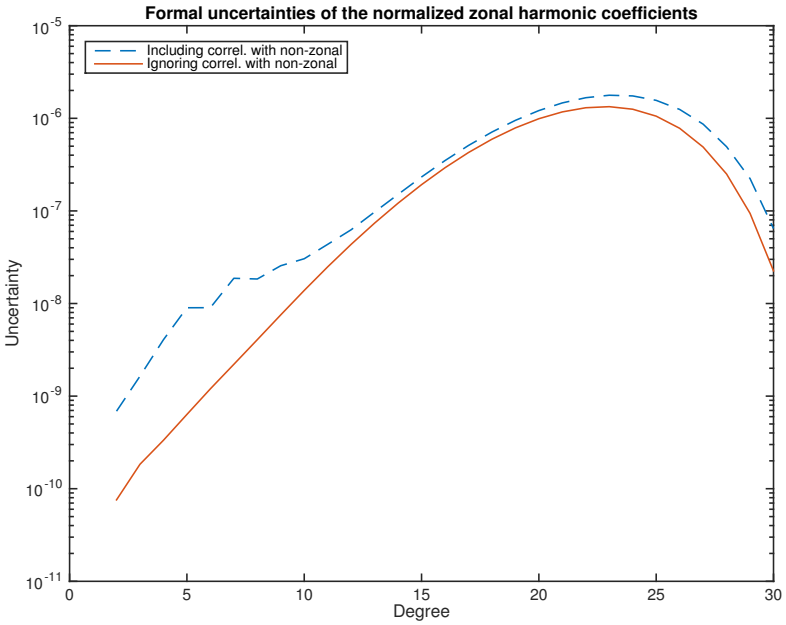

Figure 3.3: Formal errors of the zonal harmonic coefficients of Jupiter's gravitational potential obtained with the full Juno mission. The effect of the correlations with non-zonal coefficients is neglectable.

parameters would be more than the observations, making the recovering impossible.

We already remarked that the formal error of the zonal coefficients, comprehensive of tesseral harmonics correlations, is given by the diagonal entries of

$$\Gamma_{\mathbf{zz}} = (C_{\mathbf{zz}} - C_{\mathbf{zw}} C_{\mathbf{ww}}^{-1} C_{\mathbf{wz}})^{-1}.$$

The computation of the latter is difficult because the matrix $C_{\mathbf{ww}}$ is badly conditioned. We can avoid this obstacle by adding some a priori observations of the tesseral coefficients, as described in (Milani and Gronchi, 2010), Chapter 6: under the hypothesis that the depth of Jupiter's zonal winds is ~ 100 km, we can suppose that the tesseral coefficients are not larger than 10^{-8} (cf. (Parisi et al., 2016)). In other words, we can assume we observed Jupiter's potential tesseral coefficients being $\mathbf{t}_P := \mathbf{0}$ with uncertainty $s_P = \pm 10^{-8}$ and add to $C_{\mathbf{ww}}$ the a priori normal matrix $C_P := s_P^{-2} I$, where I is the identity matrix of the suitable dimension. The new covariance matrix is

$$\Gamma_{\mathbf{zz}} = [C_{\mathbf{zz}} - C_{\mathbf{zw}} (C_{\mathbf{ww}} + C_P)^{-1} C_{\mathbf{wz}}]^{-1},$$

which is no more badly conditioned. In Fig.3.3 the result is compared to the formal error obtained ignoring tesseral harmonics. While the uncertainty is higher for low-degree coefficients, it is almost the same for high-degree ones. This confirms the fact that the accuracy with which the zonal harmonic coefficients can be recovered depends mainly on the spacecraft's orbit geometry and is not largely infuenced by the presence of other parameters.

Surface gravity anomalies uncertainties

Fig. 3.4 shows the square root of the eigenvalues of the covariance matrix Γ in the 1-arc and in the full mission cases. It is clear that $\sqrt{\lambda_1}, \sqrt{\lambda_2}$ are the largest, therefore we could expect that their effect on the surface gravity anomalies uncertainty is dominating. This is only partially true. To understand this, it is useful to look at Fig. 3.5: here the contributes due to $\sqrt{\lambda_i} V^{(i)},\ i = 10, 15, 20, 25$ are compared with the effect of $\sqrt{\lambda_1} V^{(1)}$ (we considered the full mission case, the same conclusions can be drawn from the other one). The effect on the polar caps rapidly decreases as i grows, while the uncertainty on middle latitudes is of the same order of magnitude up to $i = 20$. For $i > 20$, even this effect can be considered negligible as the corresponding figure for $i = 25$ suggests.

We computed the RMS of the principal components according to the previous analysis, thus including $\mathcal{U}^{(i)},\ i = 1, \ldots, 20$. The result is shown for both the 1-arc and the full mission in Fig. 3.6. Since the uncertainty at low latitudes is $> 10^2$

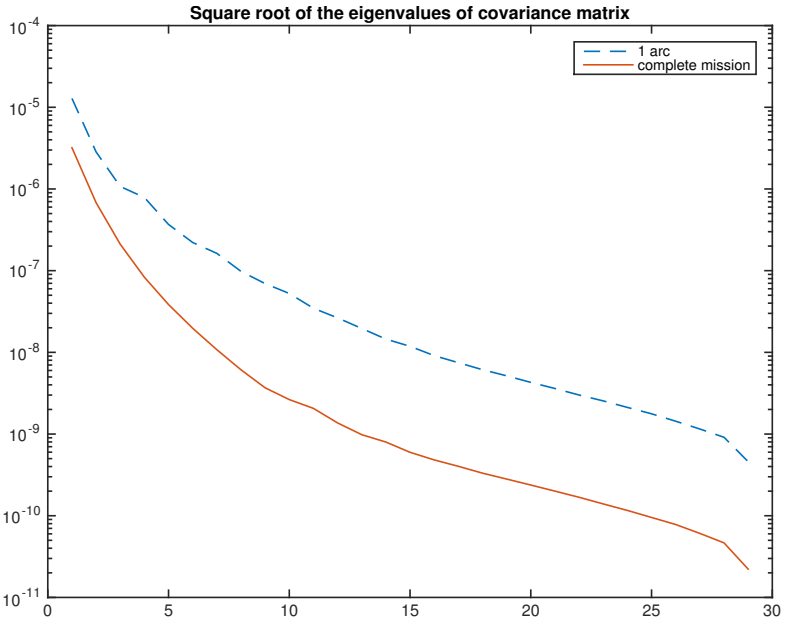

Figure 3.4: Square root of eigenvalues of covariance matrix Γ, in the case of one passage and two passages (semilogarithmic scale).

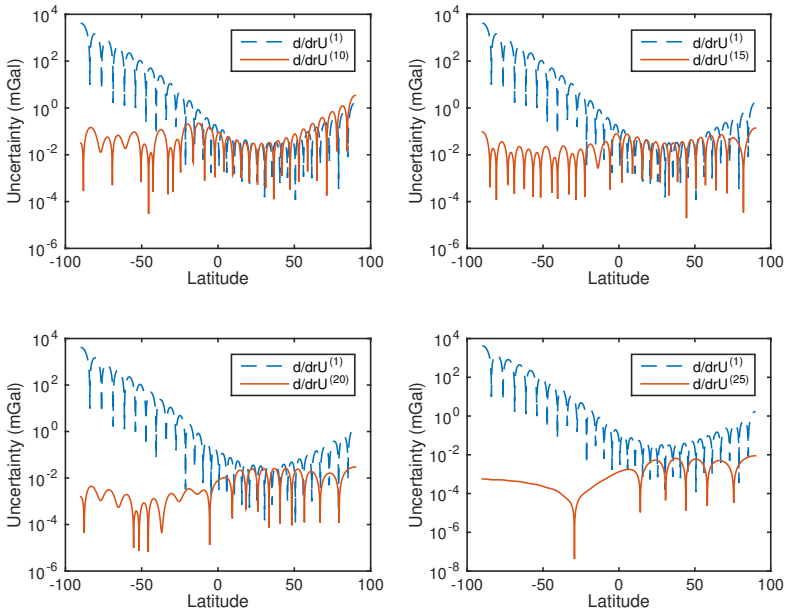

Figure 3.5: Comparison between gravity anomalies uncertainty due to $\sqrt{\lambda_1}V^{(1)}$ and $\sqrt{\lambda_i}V^{(i)}, i = 10, 15, 20, 25$ (all GS orbits were considered). The difference in magnitudine between eigenvalues reflects into a difference in anomalies uncertainty on polar caps, while around the perijove their influences are the same in terms of order of magnitude, at least up to $i = 20$.

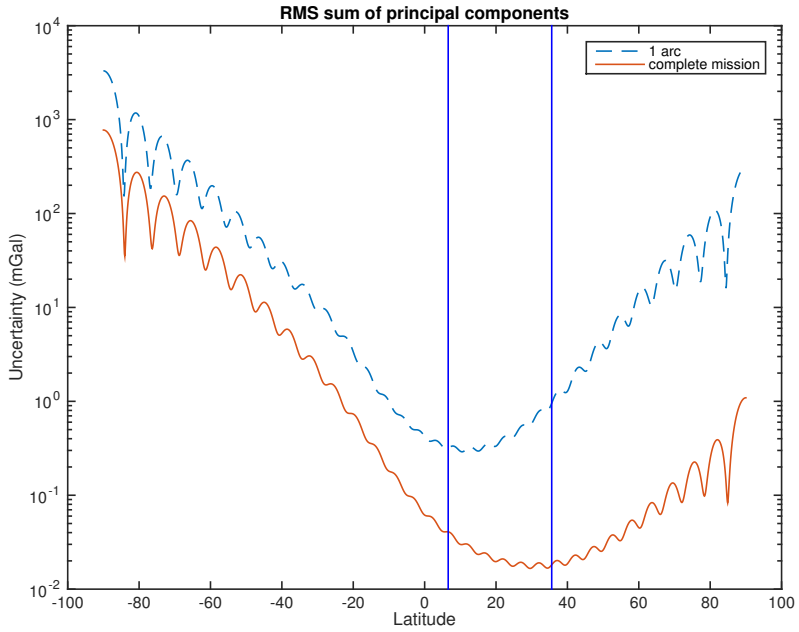

Figure 3.6: Root mean square of $\mathcal{U}^{(i)}$, $i = 1, \ldots, 20$, in the 1-arc case and for the full mission, in semilogarithmic scale. The vertical lines bound the pericenters of the Juno spacecraft on Jupiter's equator.

mGal, we conclude that the gravity field at the South pole is badly recovered. On the contrary, the gravity field at the latitudes corresponding to the Juno probe's pericenters, namely 6 deg N - 35 deg N, is well determined. The uncertainties are smaller than 10^{-1} mGal in this area.

It is evident that a full mission allows a better determination of the gravity field. The improvement with respect to the 1-arc mission is concentrated on the latitudes of the Juno's pericenters and on the northern hemisphere in general, thus confirming our claim that the accuracy in the determination of the gravity field is mainly function of the quantity of surface covered and the distance of the spacecraft from the surface.

3.3 The gravity field of Jupiter with Juno

In this section we cope with the determination of Jupiter's gravity field through orbit determination and present the results obtained by simulating the Juno Gravity Science experiment with the Orbit14 software. The model used in this section is the spherical harmonics expansion for the gravitational potential.

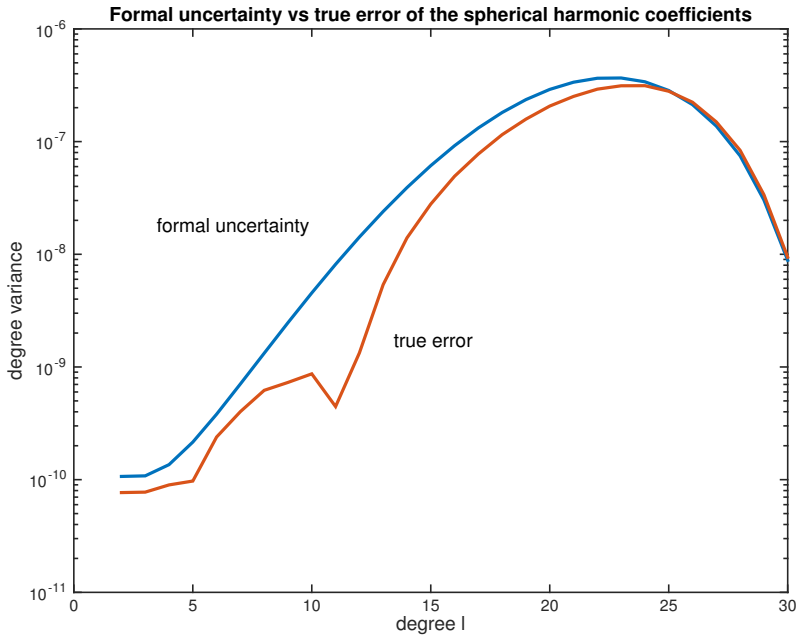

Figure 3.7: Formal error vs true error of the zonal harmonic coefficients $C_{20}, \dots C_{300}$ at convergence. The formal uncertainties increase along with the degree because of the high correlations among the parameters. Truncating at degree 30 is equivalent to set to zero the correlations with the higher-degree coefficients, making the formal errors of the last coefficients decrease, thus causing the peculiar "hump". Since we did not introduce any source of sistematic error, the true error is always less than the formal uncertainty.

First let us describe the setup for the gravity field estimation. We simulated Jupiter's gravity field using the values for the gravitational momenta J_2, J_3, J_4 and J_6 of the orbit solution by (Jacobson, 2003) and set to zero the other coefficients. We supposed Jupiter's gravity field being composed of only zonal terms, that is Jupiter being axially symmetric with respect to the rotation axis. We truncated the spherical harmonics expansion at degree 30, estimating the normalized coefficients $\overline{C}_{\ell 0}$, $\ell = 2, \dots, 30$. Finally, we used no apriori information on spherical harmonic coefficients during the estimation process.

Fig. 3.7 shows the formal uncertainties obtained at convergence compared to the true errors. Note that since no systematic error was added to the observables, but only random error, the ratio true error/formal uncertainty is about 1 for every harmonic degree. The "hump" behaviour of the formal errors curve is the result of the constraint imposed truncating the series (3.1) to a finite degree, as we already explained in Section 3.2.4. In fact, every harmonic coefficient is highly correlated to the next one. In Fig. 3.8 the correlations between all the estimated

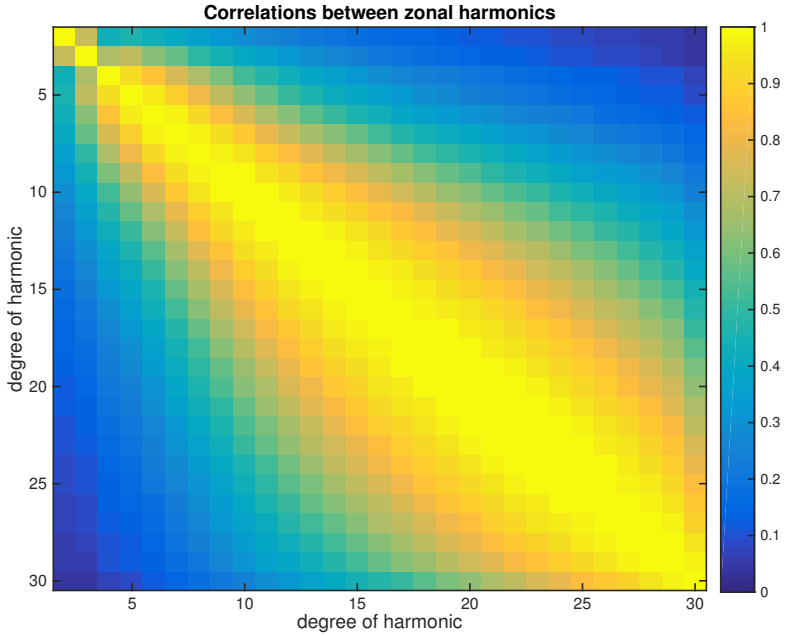

Figure 3.8: Correlations of the spherical harmonic coefficients at convergence.

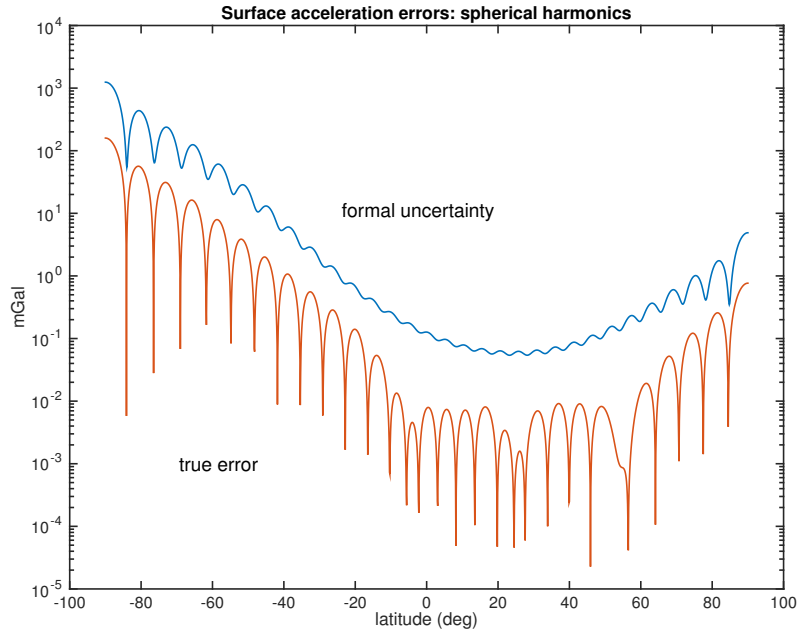

Figure 3.9: Errors in the determination of the gravity anomalies of Jupiter for the spherical harmonics coefficients $C_{\ell 0}$, $\ell = 2, \ldots, 30$, at the reference spherical surface of radius R_{Jup}, mean radius of Jupiter.

spherical harmonics coefficients are displayed. With reference to the latter, the highest values (> 0.99) are close to the diagonal and they gradually decrease to 0 when moving towards the top right corner (or, by symmetry, the bottom left) of the figure. This means that any two spherical harmonics coefficients of subsequent degrees are highly correlated, causing loss of accuracy in the determination of the high-degree coefficients, as the "hump" of Fig. 3.7 also shows. In fact, by Kaula's expansion (Kaula, 1966), two subsequent even-degree or odd-degree spherical harmonics share a great number of frequencies, thus making it hard to separate the effects. By neglecting such correlations the results would look much better, nonetheless illusory.

If we consider that the expected values of the spherical harmonic coefficients of degree ℓ, $\ell > 15$, range between 10^{-6} and 10^{-9} for depths of the zonal flows varying from 10^5 km to 10 km (cf. (Kaspi et al., 2010) and (Galanti and Kaspi, 2016)), the conclusion is that these parameters have too high uncertainties and thus cannot be trusted. In Table 3.1 the results obtained for the even normalized spherical harmonic coefficients up to degree 14 can be found.

As the zonal winds produce a signature in the gravity anomalies of Jupiter, from measuring such signature it is possible to gain information about the depth of the winds. For this reason, it is useful to look at the uncertainties of Jupiter's gravity field over some reference surface, say a sphere of radius R_{Jup}, Jupiter's mean radius. We followed the procedure described in (Konopliv and Sjogren, 1994): if $g_{r,\ell_{\max}}(r,\theta)$ is the radial component of Jupiter's zonal gravity field (truncated at some degree L), the uncertainty of the gravity anomalies due to the spherical coefficients from degree 2 to $\ell_{\max}$ as a function of the latitude of the planet, over a reference sphere of radius R_{Jup}, is

$$\sigma_{2:\ell_{\max}}(\theta) = \left(\frac{\partial g_{r,\ell_{\max}}}{\partial C_{\ell 0}}\right)^T \Gamma_{2:\ell_{\max}} \left(\frac{\partial g_{r,\ell_{\max}}}{\partial C_{\ell 0}}\right),$$

where $\Gamma_{2:\ell_{\max}}$ is the covariance matrix relative to the coefficients $C_{\ell 0}$, $\ell = 2, \ldots, \ell_{\max}$. The result for $\ell_{\max} = 30$ is shown in Fig. 3.9. The determination of the gravity anomalies is better in the latitude belt of the pericenters, the formal uncertainty being ~ 0.1 mGal. At the poles, especially the south pole, the uncertainties are much higher, ~ 1000 mGal, thus making the recovery of the gravity field over these latitudes impossible.

The same conclusion was found in Section 3.2 using a semi-analytic method. The relation between surface coverage and gravity field estimation was also investigated in (Milani and Gronchi, 2010), ch. 16, in the case of an Earth orbiter with non-polar orbit.

Note that the results of Table 3.1 have been obtained excluding Jupiter's gravita-

Coefficient	Formal Uncertainty
$\overline{C}_{20}$	1.068×10^{-10}
$\overline{C}_{40}$	1.359×10^{-10}
$\overline{C}_{60}$	3.810×10^{-10}
$\overline{C}_{80}$	1.325×10^{-9}
$\overline{C}_{100}$	4.540×10^{-9}
$\overline{C}_{120}$	1.420×10^{-8}
$\overline{C}_{140}$	3.905×10^{-8}

Table 3.1: The formal uncertainties obtained with Orbit14 of the normalized even zonal spherical harmonics coefficients from degree 2 to degree 14.

tional parameter GM_{J} from the fit. Including the latter in the estimation process - with no additional apriori information - caused a degradation of the accuracy of the coefficient $\overline{C}_{20}$ of two orders of magnitude, originated by the particular geometry of Juno Gravity Science orbits: since data are available only from pericenter passes, the distance of the spacecraft from Jupiter's center of mass is approximately the same in each pass, making the separation of the monopole effect and the $\overline{C}_{20}$ effect difficult. Since the relative uncertainty obtained for GM_{J} was $\sim 4 \times 10^{-7}$, almost twenty times worse than the current knowledge (cf. (Jacobson, 2003)), it is not questionable whether to estimate it using no apriori constraint. Thus we made a second experiment, in which we determined also GM_{J}, this time constraining its value to the currently known value, with apriori uncertainty corresponding to the current uncertainty. The correlation with coefficient $\overline{C}_{20}$ dropped, the uncertainty on the latter becoming $\sim 2 \times 10^{-10}$. The formal sigma of the other coefficients were not affected by the addition of GM_{J} to the fit, remaining the same of Table 3.1.

3.4 The ring mascons model for the gravity field

The results of Section 3.3 show that it is impossible to obtain accurate determination of the global gravity field of Jupiter from the Juno mission using the classical spherical harmonics representation. In particular, given the high uncertainties, any information about the gravity anomalies in the south pole cap should be considered meaningless. A simple geometric argument hinting at this is the following: data from the spacecraft do not cover uniformly all the surface of the planet be-

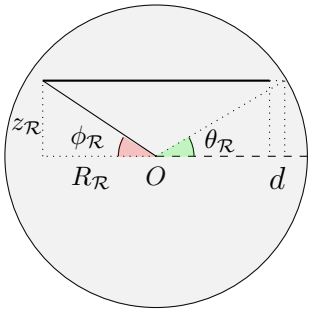

Figure 3.10: A ring mascon located at latitude $\theta_{\mathcal{R}}$ with depth d.

cause the observables are available only from a time interval of six hours centered at the pericenter and the altitude of the orbiter grows rapidly during the arc - with subsequent loss of resolution. Since the spherical harmonics are a complete orthogonal basis of the space of the harmonic functions on the sphere - and are not orthogonal on a portion of it - then the reconstruction is impossible.

A possible way of solving this degeneracy is to turn to a different system of functions, which is a basis for the observed surface, and expand the gravitational potential in this new system (e.g., the Slepian functions).

Alternatively, it may be considered the option of determining the gravity field of Jupiter only in the portion of the planet which is observed best, that is the latitude band covered by the spacecraft's pericenters from 6 deg N to 35 deg N. To do this, it is necessary to use a local model for the gravity field, introducing *ring mascons*. Similarly to what done in the case of rocky planets, where the gravity anomalies in correpondance of craters are modeled with pointwise mass concentrations (cf. (Muller and Sjogren, 1968) for the case of the Moon gravity field), we model the gravity anomalies on Jupiter using ring-shaped mascons, accomodating the fluid nature of the planet, which is approximately axially symmetric.

3.4.1 The gravitational potential of a ring

Let P be an axially symmetric planet of mean radius R_P and mass M_P and let us fix a reference frame $\Sigma = O\hat{\mathbf{e}}_1\hat{\mathbf{e}}_2\hat{\mathbf{e}}_3$, centered at the center of mass O of the planet, and where $\hat{\mathbf{e}}_1$ and $\hat{\mathbf{e}}_2$ span the equator. Let (r, θ, λ) be the spherical coordinates with respect to Σ.

Let us define a ring mascon $\mathcal{R}$ on a planet P as a zero-thickness circumference, endowed with a mass $M_{\mathcal{R}}$, lying in a plane of fixed latitude $\theta_{\mathcal{R}}$ and contained in the planet. By definition, if $R_{\mathcal{R}}$ is the radius of the ring, then $R_{\mathcal{R}} = R_P \cos\theta_{\mathcal{R}} - d$,

where d is called depth of the ring mascon. We are interested in the analytical expression of the gravitational potential $U_{\mathcal{R}}$ of a ring mascon, in particular the coefficients of its expansion in spherical harmonics

$$U_{\mathcal{R}}(r,\theta,\lambda) = \frac{GM_{\mathcal{R}}}{r}\sum_{\ell=0}^{+\infty}\frac{c_{\mathcal{R}}^{\ell}}{r^{\ell}}\sum_{m=0}^{\ell}[C_{\ell m}^{(\mathcal{R})}\cos(m\lambda)+S_{\ell m}^{(\mathcal{R})}\sin(m\lambda)]P_{\ell m}(\sin\theta),$$

where $c_{\mathcal{R}}^2 = R_{\mathcal{R}}^2 + z_{\mathcal{R}}^2$, $z_{\mathcal{R}} = R_P\sin\theta_{\mathcal{R}}$ and $r > c_{\mathcal{R}}$. A first trivial remark is that a ring mascon is axially symmetric by definition, so the tesseral coefficients $C_{\ell m}^{(\mathcal{R})}, S_{\ell m}^{(\mathcal{R})}$, $m \neq 0$, are all zero, the expansion being simply

$$U_{\mathcal{R}}(r,\theta) = \frac{GM_{\mathcal{R}}}{r}\sum_{\ell=0}^{+\infty}C_{\ell 0}^{(\mathcal{R})}\frac{c_{\mathcal{R}}^{\ell}}{r^{\ell}}P_{\ell}(\sin\theta),$$

where P_ℓ is the Legendre polynomial of degree ℓ. The following theorem gives an expression for the non-zero spherical harmonics coefficients of a ring.

Theorem 2. *Let $\mathcal{R}$ be a ring mascon of mass $M_{\mathcal{R}}$ and located at latitude $\phi_{\mathcal{R}}$ of a sphere. The coefficients of the spherical harmonic expansion of its potential are*

$$C_{\ell 0}^{(\mathcal{R})} = P_{\ell}(\sin\phi_{\mathcal{R}}).$$

Proof. Let us compute the gravitational potential of a ring $\mathcal{R}$ of density $\rho_{\mathcal{R}}$ and located at latitude $\theta_{\mathcal{R}}$ on a point $\mathbf{x} = (0,0,r)^T$ on its axis. We remarked in Section 3.4 that its spherical harmonics expansion is composed of only zonal terms. Using the definition of gravity potential,

$$U_{\mathcal{R}}(r) = \int_{\mathcal{R}}\frac{G\rho_{\mathcal{R}}}{|\mathbf{x}-\mathbf{p}|}\mathrm{d}\mathbf{p} = G\int_{\mathcal{R}}\rho_{\mathcal{R}}\sum_{\ell=0}^{+\infty}\frac{c_{\mathcal{R}}^{\ell}}{r^{\ell+1}}P_{\ell}(\cos\psi)\mathrm{d}\mathbf{p},$$

where ψ is the angle between $\mathbf{x}$ and $\mathbf{p}$. For the choice of $\mathbf{x}$, we have that $\cos\psi$ is constant and it is equal to $\sin\phi_{\mathcal{R}}$, the potential becoming trivially (assuming constant density)

$$U_{\mathcal{R}}(r) = GM_{\mathcal{R}}\sum_{\ell=0}^{+\infty}\frac{c_{\mathcal{R}}^{\ell}}{r^{\ell+1}}P_{\ell}(\sin\phi_{\mathcal{R}}).$$

By the unicity of the spherical harmonic expansion, we conclude that $C_{\ell 0}^{(\mathcal{R})} = P_{\ell}(\sin\phi_{\mathcal{R}})$. □

We conclude that the spherical harmonics expansion of the gravitational potential of a ring is

$$U_{\mathcal{R}}(r,\theta) = \frac{GM_{\mathcal{R}}}{r}\sum_{\ell=0}^{+\infty}\frac{c_{\mathcal{R}}^{\ell}}{r^{\ell}}P_{\ell}(\sin\phi_{\mathcal{R}})P_{\ell}(\sin\theta). \tag{3.15}$$

If $d = 0$ obviously $\phi_{\mathcal{R}} = \theta_{\mathcal{R}}$. In the general case $\phi_{\mathcal{R}}$ is defined by $\sin\phi_{\mathcal{R}} = z_{\mathcal{R}}/c_{\mathcal{R}}$, $\cos\phi_{\mathcal{R}} = R_{\mathcal{R}}/c_{\mathcal{R}}$. Let us remark that the coefficient of degree 1 is not zero because the center of mass of the ring does not coincide with O, unless the ring is in the equatorial plane of the planet.

A finite set of ring mascons can be used to model the gravity field of the planet in a latitude band (Θ_1, Θ_2). The low-frequency components of the gravity field are modeled with the regular gravitational potential of the planet, expanded in spherical harmonics up to degree $\ell_{\max} \leq 10$. The high-frequency components are modeled with a number m of ring mascons, of latitudes $\theta_1, \ldots, \theta_m$ such that $\Theta_1 = \theta_1 < \cdots < \theta_m = \Theta_m$, and whose gravitational potential (3.15) is expanded up to degree $L > \ell_{\max}$.

Let us fix an integer $\ell_{\max}$ and a number of ring mascons m. If $\mathcal{R}_1, \ldots, \mathcal{R}_m$ are ring mascons of masses $M_1, \ldots, M_m$ at the latitudes $\theta_1 < \cdots < \theta_m$, then a local representation of the gravity field of the planet in the latitude belt (Θ_1, Θ_2) is given by

$$U(r,\theta) = \frac{GM_P}{r} + \frac{GM_P}{r}\sum_{\ell=2}^{\ell_{\max}}\frac{R_P^{\ell}}{r^{\ell}}C_{\ell 0}P_{\ell}(\sin\theta) + U_{\mathcal{R}_1} + \cdots + U_{\mathcal{R}_m}. \tag{3.16}$$

The previous equation can be rewritten by grouping the terms of the same degree ℓ:

$$U(r,\theta) = \frac{GM_P}{r} + \frac{GM_P}{r}\sum_{\ell=1}^{L}\left(\frac{R_P}{r}\right)^{\ell}\tilde{C}_{\ell 0}P_{\ell}(\sin\theta), \tag{3.17}$$

where

$$\tilde{C}_{\ell 0} = \begin{cases} C_{\ell 0} + \displaystyle\sum_{i=1}^{m}\frac{GM_i}{GM_P}\left(\frac{c_{\mathcal{R}_i}}{R_P}\right)^{\ell} C_{\ell 0}^{(\mathcal{R}_i)} & \ell = 2, \ldots, \ell_{\max} \\ \displaystyle\sum_{i=1}^{m}\frac{GM_i}{GM_P}\left(\frac{c_{\mathcal{R}_i}}{R_P}\right)^{\ell} C_{\ell 0}^{(\mathcal{R}_i)} & \text{otherwise.} \end{cases} \tag{3.18}$$

In a least squares fit, the parameters to estimate would be the spherical harmonic coefficients $C_{\ell 0},\ \ell = 2, \ldots, \ell_{\max}$ and the masses of the ring mascons $GM_1, \ldots, GM_m$.

3.4.2 Numerical simulations

In the case of Jupiter and the Juno mission, we used a degree-8 spherical harmonic expansion of the gravitational potential of Jupiter and a number m of ring mascons in the Juno's pericenters latitude belt (Θ_1, Θ_2), where $\Theta_1 = 6$ deg N and $\Theta_2 = 35$ deg N.

The first problem was to determine how many rings to use in the representation. The first attempt was to use 30 rings, one every degree, but numerical simulations showed that it is impossible to estimate all the 30 parameters GM_i without using any a priori information on their value. Indeed, the normal matrix C of the least squares fit resulted ill-conditioned, with condition number $\sim 8 \times 10^{50}$. In fact, we obtained that the maximum number of ring mascons the software was able to solve for is $m = 11$ (all the rings equally distributed). For greater values of m the normal matrix was not sufficiently well-conditioned to be inverted. In conclusion, we set $m = 11$. We remark that - as explained in (Milani and Gronchi, 2010), Chapter 16 - good sensitivity of a spacecraft to the gravity field of a planet is obtained if the altitude is of the order of spatial scale, in this case the distance between two subsequent rings. Since 11 rings equally distributed means one ring every three degrees, which corresponds to one ring every 3660 km on the surface of Jupiter, considering that the altitude of Juno at pericenter is > 4200 km, then any attempt to determine more than 11 rings is likely not to succeed.

Note that the solution for the masses of the ring mascons must satisfy a number of constraints. For instance, if the sum $\sum_{i=1}^{m} GM_i$ were different from zero, the total mass of Jupiter would change, which surely is not something we want to happen. Thus the previous sum must be set to zero. The same holds for the degree-1 coefficients of the ring mascons potential: if their combinations, weighed with the rings' GM_i, were not null, then the center of mass of Jupiter would move from the actual location, which is again undesirable. In general, we demand that the combinations $\sum_{i=1}^{m} GM_i$ and $\sum_{i=1}^{m} GM_i \mathscr{C}_{\ell,i}$, for each $\ell \leq \ell_{\max}$, where $\mathscr{C}_{\ell,i} = C_{\ell 0}^{\mathcal{R}_i}(c_{\mathcal{R}}/R_P)^{\ell}$, $\ell = 1, \ldots, \ell_{\max}$, $i = 1, \ldots, m$, be equal to zero. In other words, we imposed that the vector $\mathbf{m} = (GM_1, \ldots, GM_m)$ of the gravitational parameters of the rings solved the linear system $F\mathbf{m} = \mathbf{0}$, where

$$F = \begin{pmatrix} 1 & 1 & \ldots & 1 \\ \mathscr{C}_{1,1} & \mathscr{C}_{1,2} & \ldots & \mathscr{C}_{1,m} \\ \vdots & \ddots & & \vdots \\ \mathscr{C}_{\ell_{\max},1} & \mathscr{C}_{\ell_{\max},2} & \ldots & \mathscr{C}_{\ell_{\max},m} \end{pmatrix}.$$

Once that we have obtained an estimation of the masses of the rings, we would like to map it to the uncertainty on Jupiter's gravity field. Using (3.17) and (3.18), we

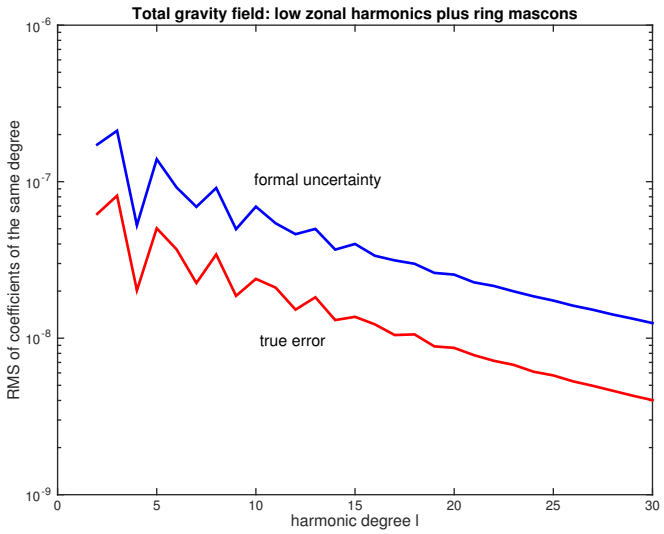

Figure 3.11: Formal uncertainties vs true error of the harmonic coefficients using the ring mascons model; the computation of the uncertainty is given by (3.19). Note that since the coefficients uncertainties are not global, they cannot be compared to Fig. 3.7.

can express the uncertainty obtained on the parameters $C_{\ell 0}, GM_i$ as uncertainty on the harmonic degree ℓ:

$$\sigma(\tilde{C}_{\ell 0}) = \begin{cases} \sigma(C_{\ell 0}) + \displaystyle\sum_{i=1}^{m} \frac{\sigma(GM_i)}{GM_P} \left(\frac{c_{\mathcal{R}_i}}{R_P}\right)^{\ell} C_{\ell 0}^{(\mathcal{R}_i)} & \ell = 2, \ldots, \ell_{\max} \\ \displaystyle\sum_{i=1}^{m} \frac{\sigma(GM_i)}{GM_P} \left(\frac{c_{\mathcal{R}_i}}{R_P}\right)^{\ell} C_{\ell 0}^{(\mathcal{R}_i)} & \text{otherwise.} \end{cases} \tag{3.19}$$

For $L = 30$, Fig. 3.11 shows the RMS of the uncertainties obtained on $\tilde{C}_{\ell 0}$ for every harmonic degree ℓ. Because of the local nature of the ring mascons model, in no way can these uncertainties be compared to those in Fig. 3.7, which are referred to a global model.

Similarly to what done in Section 3.3, the information contained in the covariance matrix of the fit can be used to obtain the accuracy in the determination of the gravity anomalies at a reference surface of Jupiter. Fig. 3.12 shows the error on the gravity anomalies at the spherical surface of radius R_{Jup}, the mean radius of Jupiter. The comparison with what obtained in Fig. 3.9 is only possible in the latitude interval (Θ_1, Θ_2) since the ring mascons model, being a local model, does not give valuable and realistic predictions of the gravity in the latitudes where the resolution of the orbiter is poorest. The two models appear to be in

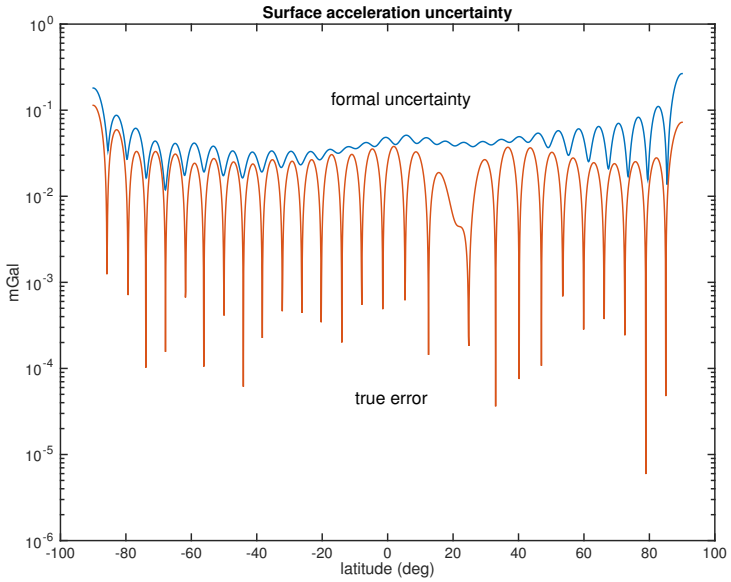

Figure 3.12: Surface acceleration uncertainty as a function of the latitude of the planet obtained using the ring mascons model for the gravity field of Jupiter. Since this model is local, the uncertainties are to be considered realistic only for the latitude belt $(6, 35)$.

good agreement in the latitude belt $(6, 35)$, the ring mascons model being more optimistic by a factor ~ 1.3.

We conclude this section by remarking that the use of the ring mascons in Jupiter's gravity field in place of the pure spherical harmonics model had no effect on the determination of the other parameters.

3.5 Other gravitational parameters

In this section we deal with the determination of the gravitational effects which are not caused by Jupiter's gravitational field directly. More specifically, we will discuss the possibility of determining Jupiter's Love numbers k_ℓ, $\ell = 2, 3, 4$ and the masses of the Galilean satellites.

3.5.1 Jupiter's tidal deformation

The tidal deformation of Jupiter, due mainly to the Galilean satellites, causes an additional gravitational perturbation on the spacecraft which, in the hypothesis of static tidal theory, is induced by a potential, called *Love potential*, whose expansion

Parameter	Formal Uncertainty
k_2	1.955×10^{-3}
k_3	4.752×10^{-3}
k_4	2.701×10^{-2}

Table 3.2: Formal uncertainty of Jupiter's Love numbers k_ℓ, $\ell = 2, 3, 4$.

in spherical harmonics series (cf. (Mignard, 1978)) is

$$U_{\text{Love}} = \sum_{\ell=2}^{+\infty} k_\ell \frac{GM_P R_{\text{Jup}}^{2\ell+1}}{r_P^{\ell+1} r^{\ell+1}} P_\ell(\cos\varphi).$$

Here M_P, r_P are respectively the mass and the distance of the perturbing body from Jupiter, r is the distance of the spacecraft, φ is the angle between the direction of the perturbing body and the direction of the orbiter, the coefficients k_ℓ are called *Love numbers* and their values are a measure of the response of Jupiter to the perturbation. The latter can be used to add more contraints to the interior structure of the planet, as it has been done in (Konopliv and Yoder, 1996) for Venus, in (Iess et al., 2012) for Titan or in (Padovan et al., 2014) for Mercury.

A sensitivity analysis disussed in (Tommei et al., 2015) showed that Juno is sensitive to the Love potential up to degree $\ell = 4$. Our dynamical model includes the Love potential due to the Sun, the Galilean satellites, Amalthea and Thebe. The value of k_2 used for simulating the observables is the conventional value 0.37 given in (Gavrilov and Zharkov, 1977). The values for k_3 and k_4 cannot be found in literature and they were set to the arbitrary value 0.7.

The results of the fit regarding these parameters can be found in Table 3.2. The Love numbers k_2 and k_3 appear to be estimated very accurately, the relative accuracy being respectively $\sim 0.26\%$ and $\sim 0.34\%$. The coefficient k_4 turns out to be determined 5 times worse than k_3.

3.5.2 The masses of the Galilean Satellites

The Galilean moons of Jupiter - Io, Europa, Ganymede and Callisto - were the first Jupiter's natural satellites to have been observed in 1610 by Galileo Galilei. Ever since the first space missions visited Jupiter, these bodies have aroused scientists' curiosity thanks to their surprising features, namely Io's volcanic activity and Europa's ocean layer.

Parameter(cm^3/s^2)	Present knowledge	Juno
GM_{Io}	1.2×10^{13}	2.7×10^{13}
GM_{Eu}	9×10^{12}	9.48×10^{13}
GM_{Ga}	1.7×10^{13}	4.81×10^{14}
GM_{Ca}	1.3×10^{13}	2.54×10^{13}

Table 3.3: Current formal uncertainties of Io, Europa, Ganymede and Callisto's GM (cf. (Jacobson, 2003)) compared to those obtained in the case of the Juno Radio Science experiment.

Even though the exploration of these moons is not one of Juno's scientific objectives, still we attempted to solve for their masses. The results obtained in terms of formal uncertainty, compared with the present knowledge, are displayed in Table 3.3. Unsurprisingly, all the Juno formal errors are higher than the present ones (obtained putting together Earth-based observations and spacecraft observations, cf. Jacobson (2003)), thus confirming that Juno will not be able to improve our knowledge of the system of Jupiter's main satellites.

In the case of the old 11-day Juno orbit, in view of possible availability of Juno observations other than those already scheduled (see Section 1.4), we tackled the determination of the Galilean Satellites' masses in two new scenarios. Both consist in "extended" Juno missions, where we supposed that the number of Juno orbits remained the same, but the number of tracking sessions raised from one per orbit to one every other day - that is 5 or 6 tracking sessions per orbit. In the first scenario the "new" observations were assumed to be in X-band, in the second in Ka-band. The obtained formal uncertainties of the masses of the satellites were indeed smaller. However, relatively to the present knowledge only for the inner satellites Io and Europa an actual improvement was obtained, though rather marginal. In the 14-day orbit case we tried to repeat the same analysis, but the results obtained were worse. For this reason we abandoned the idea of solving for the masses of the satellites, important though it may be.

Indeed, exploring the Galilean moons is crucial for the understanding of the entire Jovian system. The current status and the evolution of the system are the result of gravitational and tidal interactions among the moons and Jupiter, such as the 1:2:4 Laplace resonance among Io, Europa and Ganymede. These interactions are caused by processes that still have not been identified. To do so, it is necessary to design a dedicated mission, more complex, which will provide the same insight into the Jovian system as *Cassini-Huygens* has been doing for the last twelve years for Saturn's system. The ESA JUICE mission (cf. (ESA/SRE, 2014)), to be launched

in 2022 and expected to arrive at Jupiter in 2030, has been studied in such a way as to make a *grand-tour* of the Galilean moons Europa, Callisto and Ganymede. Among its scientific objectives is the study of the diversity of the satellite system and a full characterisation of the processes that led to the dynamically stable environment we see nowadays.

It is thus clear that a mission to Jupiter like Juno, which neglects the study of its moons, is not suitable for a comprehensive investigation of the jovian system, rather it must be regarded as the starting point for a deeper, more fascinating and even more arduous research to be conducted in the future.

CHAPTER 4

The angular momentum and the pole

Contents

Outline: In this chapter we will explore the possibility of determining the parameters relative to two physical quantities regarding Jupiter: the angular momentum magnitude and the direction of the rotation pole. The reason for having a dedicated discussion is that such parameters appear in accelerations acting on the spacecraft which induce scarcely distinguishable effects, inasmuch as the formal uncertainties are too high to ensure a good determination of the parameters.

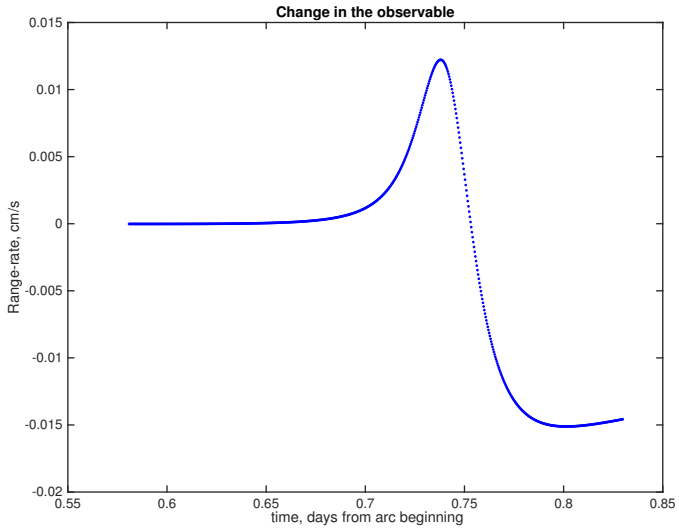

Figure 4.1: Effect on the observable (range-rate) due to the Lense-Thirring effect, during perijove 5.

4.1 The Lense-Thirring effect

In (Iorio, 2010), the author proposed to determine Jupiter's angular momentum magnitude using the information coming from the acceleration on the Juno spacecraft due to the Lense-Thirring effect. As stated in (Helled et al., 2011), knowing the angular momentum of Jupiter and the precession rate of its rotation axis is crucial for the determination of Jupiter's normalized polar moment of inertia (MOI), the latter being an important piece of information for the investigation of the interior of a planet (cf. (Guillot and Gautier, 2007)). In the following we briefly introduce the Lense-Thirring effect; for a critical analysis, the reader might want to refer to (Mashhoon et al., 1984).

Arising when the central mass rotates about some axis and is endowed with angular momentum $\mathbf{J}$, the general relativistic Lense-Thirring effect induces a precession of the longitude of the ascending node of a body moving in the gravity field of the central mass. It can be considered a frame-dragging effect and can be modeled as a perturbative acceleration $\mathbf{a}_{\rm LT}$ to be added to the equation of motion of the spacecraft. If $\mathbf{J} = J\hat{\mathbf{s}}$, where J is the angular momentum magnitude, then $\mathbf{a}_{\rm LT}$ reads (cf. (Moyer, 2003))

$$\mathbf{a}_{\rm LT} = \frac{(1+\gamma)\,GJ}{c^2\,r^3}\left[-\hat{\mathbf{s}}\times\dot{\mathbf{r}} + 3\,\frac{(\hat{\mathbf{s}}\cdot\mathbf{r})\,(\mathbf{r}\times\dot{\mathbf{r}})}{r^2}\right]. \tag{4.1}$$

Here, γ is the Post-Newtonian parameter related to the space-time curvature,

which is equal to 1 in General Relativity, c is the speed of light and $\mathbf{r}$ is the position of the spacecraft with respect to the center of mass of the planet.

Thanks to the low pericenter of its orbit and its high velocity at the closest approach ($\sim 60\,\mathrm{km}\cdot\mathrm{s}^{-1}$), the Juno spacecraft is going to detect such relativistic perturbation generated by Jupiter's rotation: the effect on the observable, displayed in Fig. 4.1, shows that the S/N ratio is approximately ~ 100. The value used for GJ in the simulated Lense-Thirring effect is $2.829\times10^{38}\ \mathrm{cm}^5\cdot\mathrm{s}^{-3}$, given by the formula $GJ = I_\mathrm{J} G M_\mathrm{J} R_\mathrm{J}^2 \Omega_\mathrm{J}$, where $I_\mathrm{J} = 0.254$ is Jupiter's MOI and $\Omega_\mathrm{J} = 1.75853\times10^{-4}\ \mathrm{s}^{-1}$ is Jupiter's angular velocity (all the values are taken from (Williams, 2015)).

For this reason, we are encouraged to believe that the determination of GJ via orbit determination could lead to a very good result. Whether this is the case or not will be discussed in Section 4.3.

4.2 The rotation of Jupiter

In this section we will describe the model of rotation of Jupiter and define the parameters to solve for in order to determine the pole of the planet. We describe two possible sets of parameters: the first is the couple *right ascension* and *declination* (with respect to a suitable reference frame), the second is a set of two *semi-empirical parameters* which correct the position of the pole defined by the International Astronomical Union (IAU) in (Archinal et al., 2011).

4.2.1 Right ascension and declination

In this section we define the first couple of parameters which determine the position of the north pole of Jupiter, and thus the direction of its rotations axis. The definition and the construction of the rotation matrix is taken from (Archinal et al., 2011).

By definition the north pole of a planet is the pole of rotation that lies on the north side of the invariable plane[1] of the Solar System. In the ICRF frame Σ_ICRF, the position of the north pole is defined by two angles, the *right ascension* α_0 and the *declination* δ_0. The former is the angular distance measured eastward along the mean equator from the x-axis to the projection of the north pole, the latter is the angular distance between the mean equator and the north pole.

The position of Jupiter's north pole intervenes in the transformation of coordinates from Σ_ICRF to Σ_BF. The two points of intersection between the ICRF equator and

[1] The plane orthogonal to the total angular momentum of the Solar System.

the Jupiter equator (that is the plane perpendicular to the rotation axis) are $\alpha_0 \pm 90°$. We define *node* the point Q of right ascension $\alpha_0 + 90°$. Let B be the intersection of the prime meridian of the planet with its equator. The angle $\phi(t)$, measured eastward from Q to B is the location of the prime meridian[2]. It is easy to show that the inclination of the body's equator with respect to the celestial equator (the equator of the ICRF) is $90° - \delta_0$. In conclusion, the matrix of coordinate transformation from Σ_{ICRF} to Σ_{BF} is

$$\mathscr{R}(t) = \mathscr{R}_3(\phi(t))\mathscr{R}_1(90° - \delta_0)\mathscr{R}_3(\alpha_0 + 90°),$$

where

$$\mathscr{R}_1(\epsilon) = \begin{bmatrix} 1 & 0 & 0 \\ 0 & \cos\epsilon & \sin\epsilon \\ 0 & -\sin\epsilon & \cos\epsilon \end{bmatrix}, \quad \mathscr{R}_2(\epsilon) = \begin{bmatrix} \cos\epsilon & 0 & -\sin\epsilon \\ 0 & 1 & 0 \\ \sin\epsilon & 0 & \cos\epsilon \end{bmatrix},$$
$$\mathscr{R}_3(\epsilon) = \begin{bmatrix} \cos\epsilon & \sin\epsilon & 0 \\ -\sin\epsilon & \cos\epsilon & 0 \\ 0 & 0 & 1 \end{bmatrix}.$$

The values of the angles α_0, δ_0 and ϕ for Jupiter are the following:

$$\begin{aligned} \alpha_0 &= 268.056595 - 0.006499T + 0°.000117 \sin J_a + 0°.000938 \sin J_b \\ &\quad + 0.001432 \sin J_c + 0.000030 \sin J_d + 0.002150 \sin J_e \\ \delta_0 &= 64.495303 + 0.002413T + 0.000050 \cos J_a + 0.000404 \cos J_b \\ &\quad + 0.000617 \cos J_c - 0.000013 \cos J_d + 0.000926 \cos J_e \\ \phi &= 284.95 + 870.536\text{d}, \end{aligned}$$

where

$$\begin{aligned} J_a &= 99°.360714 + 4850°.4046T, \quad & J_b &= 175°.895369 + 1191°.9605T, \\ J_c &= 300°.323162 + 262°.5475T, \quad & J_d &= 114°.012305 + 6070°.2476T, \\ J_d &= 49°.511251 + 64°.3T \end{aligned}$$

and d is the number of days from J2000 and T is the interval in Julian centuries (of 36525 days) from J2000.

[2]Note that Q is fixed, thus the dependence on the time variable of ϕ is due to the displacement of B. If the planet rotates uniformly with angular velocity ω, then $\phi = \phi_0 + \omega t$, where $\phi_0 = \phi(t_0)$ for an arbitrary time instant t_0 (usually t_0 =J2000) and t is the time past t_0.

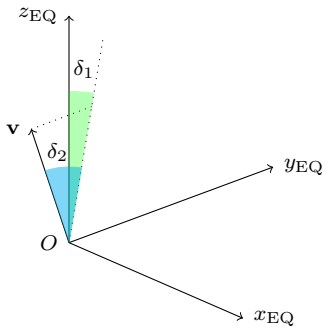

Figure 4.2: The two angles δ_1 and δ_2 defining the direction of the rotation axis (vector $\mathbf{v}$) with respect to the equatorial reference frame Σ_{EQ}, whose axes are $x_{\mathrm{EQ}}, y_{\mathrm{EQ}}, z_{\mathrm{EQ}}$.

Partial derivatives

The matrix $\mathscr{R}(t)$ defined in the previous section is used to compute the coordinates of the spacecraft acceleration due to the gravity field of the planet in the body-fixed reference frame Σ_{BF}, where the expression of the gravitational potential of the planet is given by (3.1).

Let $\mathbf{y}, \ddot{\mathbf{y}}$ be the vectors giving the coordinates of the position and the accelerations of the spacecraft in Σ_{ICRF} and $\mathbf{y}', \ddot{\mathbf{y}}'$ the vectors of the coordinates of the position and the acceleration of the spacecraft in Σ_{BF}. Then $\mathbf{y}'(t) = \mathscr{R}(t)\mathbf{y}(t)$ and $\ddot{\mathbf{y}}'(t) = \mathscr{R}(t)\ddot{\mathbf{y}}(t)$. Note that then latter is correct because we are not computing the apparent forces, but only the contribution of the gravity field to the acceleration. The computation of the whole acceleration is indeed performed in the Σ_{ECRF} frame, which is inertial, thus the apparent forces are not needed.

The partial derivatives of the acceleration $\ddot{\mathbf{y}}$ with respect to the rotation parameter α_0 are therefore (we omit the dependance on t)

$$\begin{aligned}\frac{\partial \ddot{\mathbf{y}}}{\partial \alpha_0} =& \frac{\partial \mathscr{R}^T \ddot{\mathbf{y}}'}{\partial \alpha_0} = \frac{\partial \mathscr{R}^T}{\partial \alpha_0}\ddot{\mathbf{y}}' + \mathscr{R}^T \frac{\partial \ddot{\mathbf{y}}'}{\partial \alpha_0} = \frac{\partial \mathscr{R}^T}{\partial \alpha_0}\ddot{\mathbf{y}}' + \mathscr{R}^T \frac{\partial \ddot{\mathbf{y}}'}{\partial \mathbf{y}_0'}\frac{\partial \mathbf{y}'}{\partial \alpha_0} \\ =& \frac{\partial \mathscr{R}^T}{\partial \alpha_0}\ddot{\mathbf{y}}' + \mathscr{R}^T \frac{\partial \ddot{\mathbf{y}}'}{\partial \mathbf{y}_0'} \cdot \frac{\partial \mathscr{R}}{\partial \alpha_0}\mathbf{y},\end{aligned}$$

where $\mathbf{y}_0'$ are the initial conditions of the spacecraft. The partial derivatives with respect to δ_0 are formally identical.

4.2.2 Semiempirical model

Another possibility for the modelization of the direction of Jupiter's rotation axis is to use a semiempirical model.

The idea is to keep fixed the angles α_0 and δ_0 described in the previous section and, in order to take into account a possible deviation of Jupiter's rotation axis from that model, we define two angles δ_1 and δ_2 such that the coordinates in Σ_{EQ} of the unit vector $\mathbf{v}$, giving the direction of the rotation axis, are (see figure 4.2)

$$[\mathbf{v}]_{\Sigma_{\mathrm{EQ}}} = (\sin\delta_1\cos\delta_2, -\sin\delta_2, \cos\delta_1\cos\delta_2)^T.$$

Consequently, the time-dependent transformation mapping Σ_{EQ} into Σ_{BF} is

$$\mathscr{S}(t) = \mathscr{R}_3(\phi(t))\mathscr{R}_1(\delta_2)\mathscr{R}_2(\delta_1).$$

The partial derivatives with respect to δ_1, δ_2 are similar to the partial derivatives with respect to α_0, δ_0.

In Fig. 4.3 the effect on the observable due to a change in the angle δ_1 of 10^{-7} rad is displayed. Two things should be remarked: first, the S/N ratio is high enough to ensure the sensitivity of the spacecraft to the direction of the rotation axis (the same S/N is obtained for a variation of the angle δ_2); second, the shape of the signal is very similar to the effect on the observable due to GJ (Fig. 4.1). This constitutes a first clue to the fact that the effects due to the Lense-Thirring acceleration and to the rotation axis are almost indistinguishable by the orbit determination process, thus affecting the determination of the related parameters GJ, δ_1, δ_2.

4.3 The problem of the correlation

In this section we present the results of a simulation of the Juno Radio Science experiment regarding the parameter GJ and the semi-empirical parameters δ_1, δ_2. The same results are obtained if solving for the parameters α_0, δ_0. For this reason, the discussion here is limited to the δ_1, δ_2, as it was done in (Cicalò et al., 2016).

Although the S/N ratio hinted that GJ could be determined with high level of accuracy, the results of a full parameter estimation simulation showed that this objective cannot be achieved in practice. Indeed we obtained that GJ cannot be estimated at all since the formal error obtained is too high if compared to its nominal value[3], the relative error being $\sim 112\%$. By analyzing the covariance

[3]See Section 4.1 for the nominal value used in the simulation.

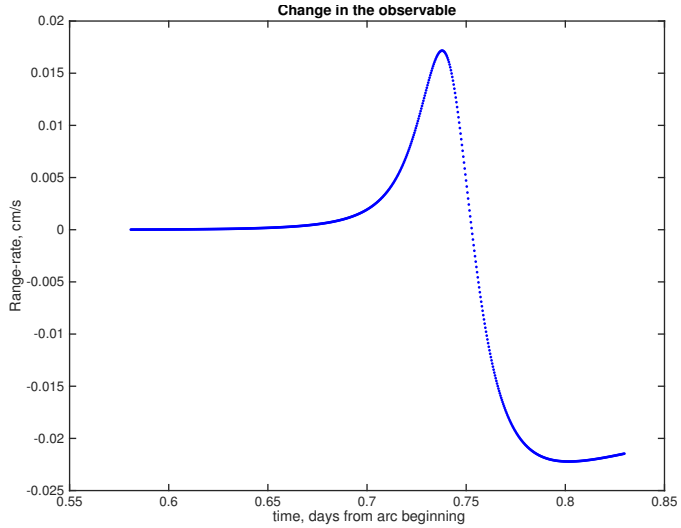

Figure 4.3: Effect on the observable (range-rate) due a change in δ_1 of 10^{-7}, during perijove 5.

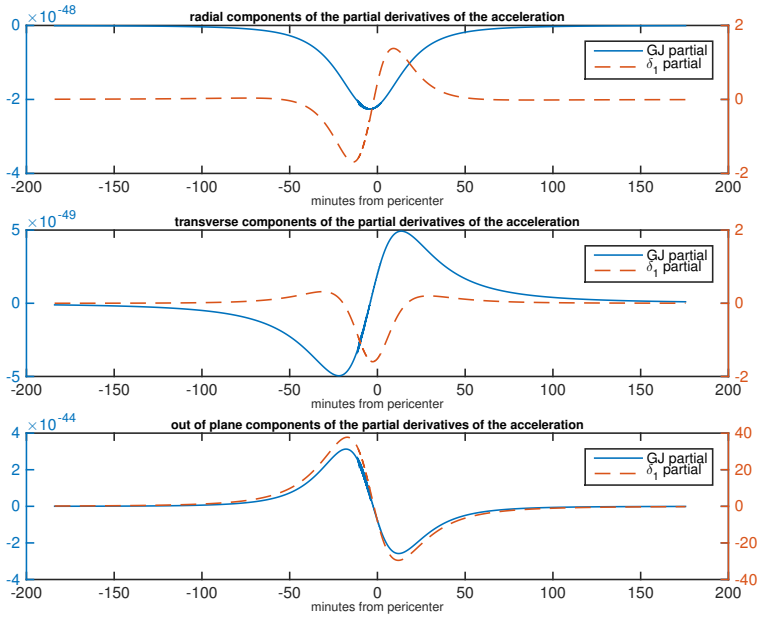

Figure 4.4: The three components in the RTW frame of the partial derivatives of the acceleration acting on the spacecraft with respect to GJ and δ_1, relative to perijove 5, in semi-logarithmic scale. The two out-of-plane components are almost proportional during the entire pass. Units are $\mathrm{cm}^{-4}\cdot\mathrm{s}$ for $\partial\mathbf{a}/\partial GJ$ and $\mathrm{cm}\cdot\mathrm{rad}^{-1}\cdot\mathrm{s}^{-2}$ for $\partial\mathbf{a}/\partial\delta_1$ which coincide for most of the duration of the pass. The radial and transverse components are at least one order of magnitude smaller than the out-of-plane one.

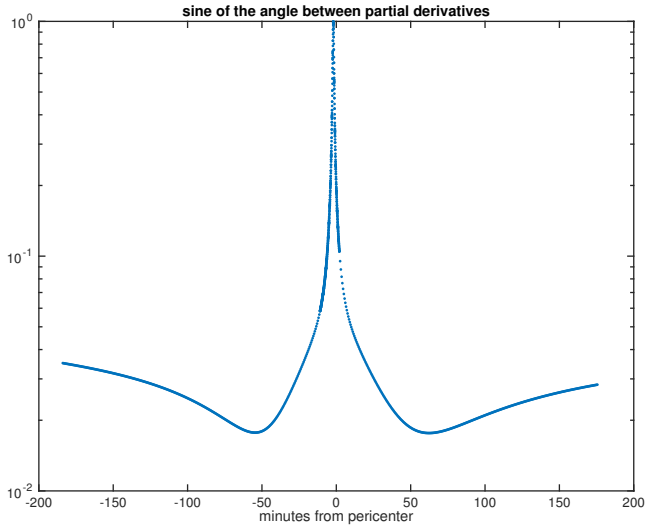

Figure 4.5: The sine of the angle between the two partial derivatives $\partial\mathbf{a}/\partial GJ$ and $\partial\mathbf{a}/\partial\delta_1$ of the acceleration $\mathbf{a}$ acting on the spacecraft, during perijove 5, semi-logarithmic scale.

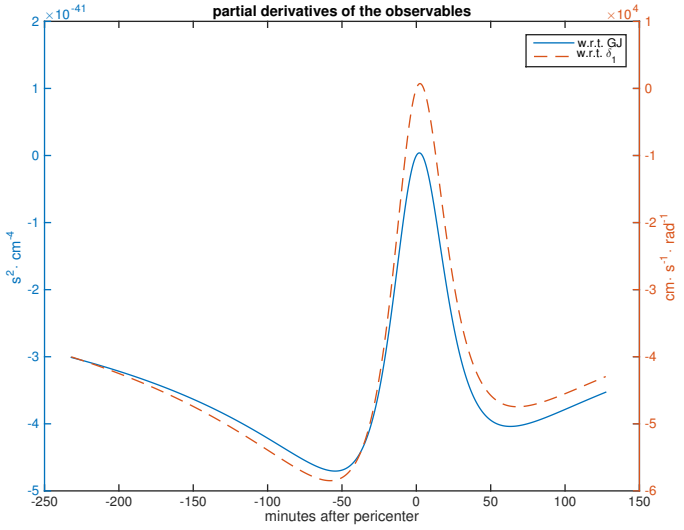

Figure 4.6: The partial derivatives of the range-rate observables with respect to the parameters δ_1 and GJ (perijove pass 4). The two are almost proportional, thus their effects can be hardly separated by the orbit determination process.

matrix, we found that GJ is highly correlated to δ_1, $\mathrm{corr}(GJ, \delta_1) \sim 0.9996$. This outcome is not surprising: by comparing Fig. 4.1 and Fig. 4.3, it is evident that the effect on the observable of a change in δ_1 is very similar to the effect due to the Lense-Thirring effect.

Generally speaking such high a value for the correlation is not enough to reflect a degeneration in the normal matrix. Nevertheless it can cause the degradation of some outcomes. Since the correlations between GJ, δ_1 and the other parameters are less than 0.7, we believe that the cause of such poor estimation of the parameter GJ is due to some symmetry involving just GJ and δ_1, which generates an approximate rank deficiency in the normal matrix (cf. (Milani and Gronchi, 2010), Chapter 6). Indeed, excluding δ_1 and δ_2 from the fit, the relative accuracy in the determination of GJ was $\sim 4\%$.

We investigated the reason for the presence of such a high correlation numerically. It is easy to show (see Section 4.6) that if there exist two solve-for parameters x_1, x_2 such that the corresponding partial derivatives of the acceleration $\partial\mathbf{a}/\partial x_1$ and $\partial\mathbf{a}/\partial x_2$ are linearly dependent vectors, then the normal matrix is singular. If such two vectors were not parallel, nonetheless the sine of the angle α formed by the two vectors is small, say $\sin(\alpha) = \epsilon$, then although the normal matrix is not singular, the correlation between x_1 and x_2 is $\mathrm{corr}(x_1, x_2) = 1 - o(\epsilon^2)$. This is the case of the two parameters GJ, δ_1. As Fig. 4.4 shows, the two partial derivatives $\partial\mathbf{a}/\partial GJ$ and $\partial\mathbf{a}/\partial\delta_1$ are actually very close to being parallel: the ratio of the out-of-plane components in the RTW frame (the other components are smaller by order of magnitudes and thus negligible) during perijove 5 is almost constant. The sine of the angle between these partial derivatives during perijove 5 (Fig. 4.5) is between 10^{-1} and 10^{-2} except for a 8-minute time interval around pericenter. Even a short period of time in which $\sin(\alpha) \sim 1$ would be in general enough to decorrelate the parameters, but in this case during that time interval the (dominant components of the) partial derivatives are near zero. Their effects are orders of magnitudes smaller than in the rest of the pass and therefore even if $\sin(\alpha)$ gets close to 1, the correlation does not decrease.

The same qualitative behaviour can be found in the partial derivatives of the range-rate observable (Fig. 4.6). Although not being perfectly proportional, their effects are not easily separable by the parameter estimation process.

4.4 A priori knowledge of the pole

If some previous knowledge of the parameters involved in the approximated rank deficiency is available, either from past space missions or theoretical considerations,

some a priori constraints could be added to the fit (using methods described for instance in (Bierman, 2006) and discussed in Section 2.1.3). If such information is accurate enough, then the degeneracy could be solved, at least partially.

We made three experiments. In all of them we performed full simulations, that is we determined Jupiter's gravity field, Love numbers, the orbit of the spacecraft, the orbit of BJS, the angular momentum magnitude GJ and the angles δ_1, δ_2. The three experiments distinguish themselves in the values of apriori sigma used on δ_1, δ_2:

- in the first experiment (exp. A), we added a priori observations of the δ_1 angle, with a priori uncertainty $\sigma_{\mathrm{AP}} = 10^{-7}$ rad;
- the second (exp. B) is the same as exp. A, except for $\sigma_{\mathrm{AP}} = 10^{-8}$ rad;
- in the third (exp. C) we assumed a priori knowledge about both the angles δ_1 and δ_2, with uncertainty $\sigma_{\mathrm{AP}} = 10^{-8}$ rad.

The results regarding GJ in the three experiments are shown in Table 4.1. In experiment A, although the correlation between GJ and δ_1 decreased (to 0.991), the relative accuracy in the determination of GJ was $\sim 48\%$, thus yet too low. In experiment B the correlation between δ_1 and GJ was less than 0.7 and GJ's relative accuracy $\sim 8\%$. Finally, experiment C showed that knowing the direction of the rotation axis up to 10^{-8}rad level would allow the estimation of GJ with relative accuracy of $\sim 6\%$.

Of course, the use of a priori constraints on Jupiter's rotation axis must reflect the actual availability of this information, otherwise the results obtained would be meaningless. Possible sources of knowledge can be, as anticipated, the measurements made during other experiments, other space missions, or from the observations of Jupiter's satellites orbits, which trace Jupiter's equator.

4.5 The precession rate

Although the determination of Jupiter's MOI looks compromised because of the poor estimation of GJ, it should not be forgotten that the latter is not the only parameter used to retreive the former. The precession rate $\dot{\psi}$ of Jupiter's rotation axis with respect to the normal of the invariable plane is another source of information about Jupiter's MOI. In (Le Maistre et al., 2016) the authors propose a new model of precession for Jupiter's rotation axis and perform numerical simulations using Jet Propulsion Laboratory's software ODP to assess the accuracy with which

	Exp. A	Exp. B	Exp. C
$\sigma_{AP}(\delta_1)$	10^{-7}	10^{-8}	10^{-8}
$\sigma_{AP}(\delta_2)$	–	–	10^{-8}
GJ rel. acc.	40%	13%	8%

Table 4.1: Relative accuracy in the determination of GJ as resulting from three different experiments: in experiment A and B a priori information on δ_1 alone ($\sigma_{AP} = 10^{-7}$ and 10^{-8} respectively) is considered, in experiment C a priori information on both rotation axis angles δ_1 and δ_2 ($\sigma_{AP} = 10^{-8}$) is included.

Parameter	Nom. value	Formal unc.	Relative unc.
$\dot{\psi}$	-3269 mas/yr	1.99 mas/yr	0.06%

Table 4.2: Nominal value, formal uncertainty, relative uncertainty of Jupiter's precession rate $\dot{\psi}$ obtained with the software ODP (Le Maistre et al., 2016).

such rate can be retrieved with Juno. The results are very encouraging, insofar as $\dot{\psi}$ is declared to be determined with relative accuracy $\sim 0.06\%$ (see Table 4.2). Furthermore, it is showed that such high an accuracy induces the same accuracy on Jupiter's MOI.

According to the analysis in (Helled et al., 2011), this should lead at least to conclude whether Jupiter has a core or not. In the best case, such could be the precision in the determination of the size and the mass of the core that it could help distinguish among competing scenarios for the planet's origins.

Part of our future work will be to enrich ORBIT14 with the possibility of determining Jupiter's precession rate, since for the time being it is the only chance to gain information on its moment of inertia.

4.6 Degeneracy of the normal matrix

This section contains the mathematical details cited and used in Section 4.3.

We recall that the normal matrix C is obtained multiplying the design matrix B

by its transpose. The generic component of B is

$$b_{ij} = \frac{\partial \xi_i}{\partial x_j} = -\frac{\partial r_i}{\partial x_j} = -\frac{\partial r_i}{\partial \mathbf{y}} \cdot \frac{\partial \mathbf{y}}{\partial x_j}. \tag{4.2}$$

The vectors $\partial \mathbf{y}/\partial x_j$ are computed solving the Cauchy problem, known as variational equation ((Milani and Gronchi, 2010), ch. 2),

$$\begin{cases} \dfrac{\partial}{\partial t}\dfrac{\partial \mathbf{y}}{\partial \mathbf{x}} = \dfrac{\partial \mathbf{a}}{\partial \mathbf{y}} \cdot \dfrac{\partial \mathbf{y}}{\partial \mathbf{x}} + \dfrac{\partial \mathbf{a}}{\partial \mathbf{x}} \\ \dfrac{\partial \mathbf{y}}{\partial \mathbf{x}}(0) = \mathbf{0}, \end{cases}$$

where $\mathbf{a}$ is the acceleration, $\mathbf{y}$ is the state vector and $\mathbf{x}$ is a set of parameters not involving the state vector initial coordinates.

Let us suppose, without loss of generality, that for the two parameters x_1, x_2 the partial derivatives satisfy

$$\frac{\partial \mathbf{a}}{\partial x_2} = c\frac{\partial \mathbf{a}}{\partial x_1}, \quad c \in \mathbb{R} \setminus \{0\};$$

it is an easy exercise to show that necessarily $\partial \mathbf{y}/\partial x_2 = c\partial \mathbf{y}/\partial x_1$ and consequently $b_{i2} = cb_{i1}$ for all i, that is B is not full-rank (and so is C).

Now, let us suppose that the two partial derivatives are not parallel, but the angle they form is close to zero; if we call α such angle, we suppose $\sin(\alpha) = \epsilon$, with ϵ infinitesimal. By taking the orthogonal projection of $\frac{\partial \mathbf{a}}{\partial x_2}$ on the subspace generated by $\frac{\partial \mathbf{a}}{\partial x_1}$, it follows that there exists a vector $\boldsymbol{\eta}$ and a constant $c \in \mathbb{R} \setminus \{0\}$ such that

$$\frac{\partial \mathbf{a}}{\partial x_2} = c\frac{\partial \mathbf{a}}{\partial x_1} + \boldsymbol{\eta};$$

if we call $\mathbf{v} := \frac{\partial \mathbf{a}}{\partial x_1}$ and $\mathbf{w} := \frac{\partial \mathbf{a}}{\partial x_2}$, then

$$c = \frac{\mathbf{v} \cdot \mathbf{w}}{\|\mathbf{v}\|^2}$$

and

$$\begin{aligned} \|\boldsymbol{\eta}\|^2 &= \|\mathbf{w}\|^2 + c^2 \|\mathbf{v}\|^2 - 2c\mathbf{v} \cdot \mathbf{w} \\ &= \|\mathbf{w}\|^2 - \frac{(\mathbf{v} \cdot \mathbf{w})^2}{\|\mathbf{v}\|^2} \\ &= \|\mathbf{w}\|^2 \left(1 - \cos^2 \alpha\right) \\ &= \epsilon^2 \|\mathbf{w}\|^2, \end{aligned}$$

thus $\|\boldsymbol{\eta}\| = o(\epsilon)$.

Let us show that, for such a choice of $\frac{\partial \mathbf{a}}{\partial x_1}$ and $\frac{\partial \mathbf{a}}{\partial x_2}$, the corresponding solutions $\mathbf{y}_1 := \frac{\partial \mathbf{y}}{\partial x_1}$ and $\mathbf{y}_2 := \frac{\partial \mathbf{y}}{\partial x_2}$ of the variational equation satisfy a similar property: there exists a vector $\mathbf{z}$ with $\|\mathbf{z}\| = o(\epsilon)$ such that

$$\mathbf{y}_2 = c\mathbf{y}_1 + \mathbf{z}.$$

Since $\mathbf{y}_1$ and $\mathbf{y}_2$ are respectively solutions of the two differential systems $\dot{\mathbf{y}}_1 = A(t)\mathbf{y}_1 + \mathbf{v}$ and $\dot{\mathbf{y}}_2 = A(t)\mathbf{y}_2 + \mathbf{w}$, where the matrix $A(t) = \frac{\partial \mathbf{a}}{\partial \mathbf{y}}$ is a continuous function of t, then the vector $\mathbf{z} := \mathbf{y}_2 - c\mathbf{y}_1$ solves the Ordinary Differential Equation (ODE)

$$\dot{\mathbf{z}} = A\mathbf{z} + \boldsymbol{\eta}.$$

Let $\rho(t)$ be its norm, $\rho = \|\mathbf{z}\|$; then,

$$\dot{\rho} = \frac{\langle \mathbf{z}, \dot{\mathbf{z}} \rangle}{\|\mathbf{z}\|} \leq \|\dot{\mathbf{z}}\| \leq \|A\|\, \rho + \|\boldsymbol{\eta}\|\,.$$

Thus $\rho \leq u$, where u is a solution of the ODE $\dot{u} = \|A\|\, u + \|\boldsymbol{\eta}\|$:

$$\rho \leq e^{a(t)} \int_0^t e^{-a(s)}\, \|\boldsymbol{\eta}(s)\|\, ds;$$

this implies that $\rho \leq \sup \|\boldsymbol{\eta}\|\, t = o(\epsilon)$, as we wanted to prove.

Now, let us show that if x_1, x_2 are the only solve-for parameters and the angle α between the two vectors $\mathbf{v}$ and $\mathbf{w}$ is such that $\sin\alpha = \epsilon$, then $\operatorname{corr}(x_1, x_2) = 1 - o(\epsilon^2)$. Let $\boldsymbol{\xi}_i$ be the derivative of the residual with respect to the parameter x_i. From (4.2) it follows that

$$\boldsymbol{\xi}_2 = c\boldsymbol{\xi}_1 + \boldsymbol{\zeta}, \quad \|\boldsymbol{\zeta}\| = o(\epsilon).$$

It is easy to show that the normal matrix is

$$C = \begin{pmatrix} \|\boldsymbol{\xi}_1\|^2 & c\,\|\boldsymbol{\xi}_1\|^2 + \boldsymbol{\xi}_1 \cdot \boldsymbol{\zeta} \\ c\,\|\boldsymbol{\xi}_1\|^2 + \boldsymbol{\xi}_1 \cdot \boldsymbol{\zeta} & \|c\boldsymbol{\xi}_1 + \boldsymbol{\zeta}\|^2 \end{pmatrix}, \tag{4.3}$$

the covariance matrix is

$$\Gamma = \frac{1}{\det C} \begin{pmatrix} \|c\boldsymbol{\xi}_1 + \boldsymbol{\zeta}\|^2 & -c\,\|\boldsymbol{\xi}_1\|^2 - \boldsymbol{\xi}_1 \cdot \boldsymbol{\zeta} \\ -c\,\|\boldsymbol{\xi}_1\|^2 - \boldsymbol{\xi}_1 \cdot \boldsymbol{\zeta} & \|\boldsymbol{\xi}_1\|^2 \end{pmatrix} \tag{4.4}$$

and consequently the correlation $\operatorname{corr}(x_1, x_2)$ is, at the first order in ϵ,

$$\operatorname{corr}(x_1, x_2) = \frac{c\,\|\boldsymbol{\xi}_1\|^2 + \boldsymbol{\xi}_1 \cdot \boldsymbol{\zeta}}{\|\boldsymbol{\xi}_1\|\, \|c\boldsymbol{\xi}_1 + \boldsymbol{\zeta}\|} = \left(1 + \frac{\boldsymbol{\xi}_1 \cdot \boldsymbol{\zeta}}{c\,\|\boldsymbol{\xi}_1\|^2}\right)\left(1 - \frac{\boldsymbol{\xi}_1 \cdot \boldsymbol{\zeta}}{c\,\|\boldsymbol{\xi}_1\|^2}\right) = 1 - o(\epsilon^2), \tag{4.5}$$

as we wanted to prove.

Part II

Analysis of the Juno cruise phase data

CHAPTER 5

Statistical analysis of the cruise phase data

Contents

Outline: In this chapter we present a statistical analysis - performed using ORBIT14 - of Juno Doppler data collected in the first half of 2015, during several tracking sessions performed by the Deep Space Network (DSN). In particular, we will tackle the analysis of the Day of the Year (DOY) 056 (corresponding to February 25). At that time the Juno spacecraft was on its way to Jupiter, more than 4.5 AU far from the Sun. Although the dynamical model of the probe in this case is much simpler than the one in jovicentric orbit in terms of forces acting on the spacecraft, many others are the corrections and calibrations that should be taken into account when computing the observable in order to reach the desired accuracy. Using the Allan Deviation, we analyse the quality of the data delivered by DSN and study the numerical noise introduced by the software ORBIT14 when computing the observable. We conclude with the analysis of the residuals of a least-squares fit of the given data.

5.1 Dynamical model for interplanetary spacecraft

The equation of motion for a spacecraft in interplanetary orbit is relatively easier than in the planetary case. The acceleration acting on the spacecraft can be expressed with the following formula

$$\mathbf{a} = \mathbf{a}_{\mathrm{N}} + \mathbf{a}_{\mathrm{PN}} + J_{2\odot}\mathbf{a}_{J_{2\odot}} + \mathbf{a}_{\mathrm{ng}},$$

where: $\mathbf{a}_{\mathrm{N}}$ is the newtonian N-body gravitational attraction due to the Sun, the planets, the dwarf planets and a number of asteroids; $\mathbf{a}_{\mathrm{PN}}$ is the Post-Newtonian term, accounting for the relativistic effects; $J_{2\odot}\mathbf{a}_{J_{2\odot}}$ is the acceleration caused by the Sun's oblateness and $\mathbf{a}_{\mathrm{ng}}$ includes the non-gravitational perturbations.

For a description of the relativistic terms, the reader may refer to (Milani et al., 2010). In the following section we will deal with the non gravitational perturbations term. We will then go on to describe all the corrections to the position of the ground antenna on Earth needed for accurate computation of the prediction function.

5.1.1 Solar radiation pressure

The main non-gravitational perturbation experienced by the Juno spacecraft in interplanetary orbit is the solar radiation pressure. Such force depends on the angle β between the incident radiation and the surface normal, the distance of the spacecraft from the sun r, the *solar constant* at 1 AU $\Phi_{\odot} = 1361$ W/m^2 (cf.

(Kopp and Lean, 2011)) and three constants, α, ρ, δ expressing the properties of radiation absorption, reflectivity and diffusivity of the spacecraft. The reader is recommended to consult (Milani and Gronchi, 2010), Chapter 14 for the explicit formulae.

Since no model of the spacecraft and of the optical properties of its surface are available because subject to information export restrictions (ITAR), we model the acceleration $\mathbf{a}_{\text{ng}}$ with semi-empirical parameters to be estimated during the fit. Since the solar radiation pressure can be considered constant during an observed arc of interplanetary orbit, we introduce three constant forces in the radial, transverse and out-of-plane directions and estimate them. In fact the main effect is given by the radial component, therefore our fit includes the latter only.

5.1.2 Modelling the position of the station

In order to compute the prediction function, not only do we need to know the position of the spacecraft, but also the exact position of the ground station on Earth. The following corrections have to be applied to the position of the antenna in the ITRF Σ_{ITRF}, before the inertial position is computed. Fig. 5.1 shows the difference between the DOY056 observables and the predictions (the so-called *pre-fit residuals*) if we neglect these corrections. For more details on the models, see (IERS, 1992) and (Moyer, 2003), Chapter 5.

Body-fixed velocity of the station

Let $\mathbf{r}_{\text{bf}}$ be the position of the ground station in the body-fixed reference frame. Because of the crust movement, the velocity of the spacecraft in this reference frame $\mathbf{v}_{\text{bf}}$ is not zero. For this reason, the following correction $\Delta\mathbf{r}_{\text{bf}}$ must be added to $\mathbf{r}_{\text{bf}}$:

$$\Delta\mathbf{r}_{\text{bf}} = \mathbf{v}_{\text{bf}}(t - t_0),$$

where t is the current time instant and t_0 is a reference time instant.

Note that in general we can write

$$\Delta\mathbf{r}_{\text{bf}} = s_r\hat{\mathbf{r}}_{\text{bf}} + s_\phi\mathbf{N} + s_\lambda\mathbf{E},$$

where $\hat{\mathbf{r}}_{\text{bf}} = \mathbf{r}_{\text{bf}}/|\mathbf{r}_{\text{bf}}|$, $\mathbf{N} = (-\sin\phi\cos\lambda, -\sin\phi\sin\lambda, \cos\phi)$, $\mathbf{E} = (-\sin\lambda, \cos\lambda, 0)$, and ϕ, λ are the latitude and the longitude of the tracking station.

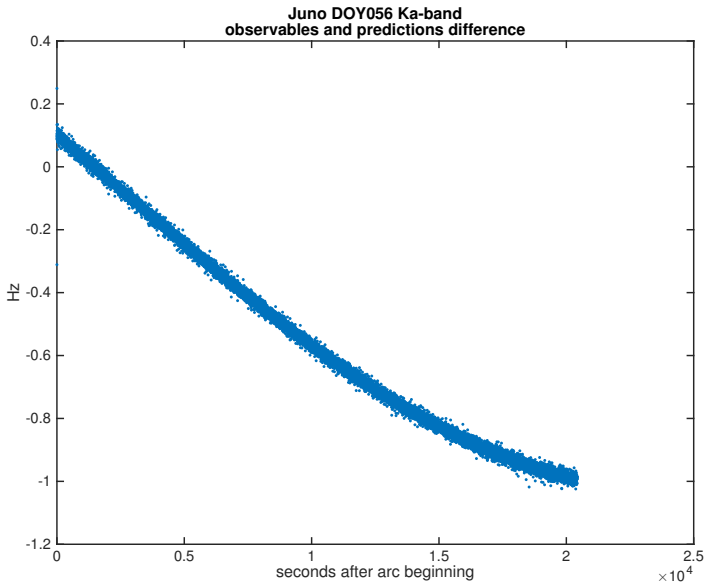

Figure 5.1: Difference between observations and predictions from DOY056, Ka-band. The predictions do not include the corrections to the position of the tracking antenna.

First-order tidal displacement

The solid tides induced by the differential attraction of the Sun and the Moon give rise to a displacement of the ground station, which can be expanded in series. The first-order contribution reads

$$\Delta\mathbf{r}_{\mathrm{bf}} = \sum_{j=1}^{2} \frac{GM_j}{GM_{\mathrm{E}}} \frac{r^4}{R_j^3} \left\{ 3l_2(\hat{\mathbf{R}}_j \cdot \hat{\mathbf{r}}_{\mathrm{bf}})\hat{\mathbf{R}}_j + \left[3\left(\frac{h_2}{2} - l_2\right)(\hat{\mathbf{R}}_j \cdot \hat{\mathbf{r}}_{\mathrm{bf}})^2 - \frac{h_2}{2} \right] \hat{\mathbf{r}}_{\mathrm{bf}} \right\},$$

where: $r = |\mathbf{r}_{\mathrm{bf}}|$; $\mathbf{R}_j$ is the body-fixed geocentric position of the body j, $R_j = |\mathbf{R}_j|$ and $\hat{\mathbf{R}}_j = \mathbf{R}_j/R_j$; $h_2 = 0.6090$ and $l_2 = 0.0852$ are the second-degree Earth Love numbers (IERS, 1992).

Second-order tidal displacement

The second-order contribution of the tidal displacement reads

$$s_r = -(1.264 \times 10^{-5}\ \mathrm{km}) \sin(2\phi) \sin(\theta_{\mathrm{M}} + \lambda),$$

where θ_{M} is the mean sidereal time.

Permanent displacement due to Solid Earth Tides

This accounts for the constant part of the displacement of the tracking station due to solid Earth tides. The correction is given by

$$s_r = -h_2(0.19841 \times 10^{-3} \text{ km}) \left(\frac{3}{2} \sin^2 \phi - \frac{1}{2} \right)$$
$$s_\phi = -l_2(0.29762 \times 10^{-3} \text{ km}) \sin(2\phi).$$

Ocean loading

This effect is due to the periodic ocean tides. Assuming the Earth spherical, the displacements in the geocentric north, radial and east directions are

$$s_r = +10^{-3} \sum_{i=1}^{11} A_i^r \cos(\theta_i + \chi_i - \phi_i^r) \quad \text{km}$$
$$s_\phi = -10^{-3} \sum_{i=1}^{11} A_i^S \cos(\theta_i + \chi_i - \phi_i^S) \quad \text{km}$$
$$s_\lambda = -10^{-3} \sum_{i=1}^{11} A_i^W \cos(\theta_i + \chi_i - \phi_i^W) \quad \text{km}.$$

Here, A_i^r, A_i^S, A_i^W are the amplitudes, θ_i are astronomical arguments, χ_i are called Schwiderski phase angles, $\phi_i^r, \phi_i^S, \phi_i^W$ are the Greenwich phase legs. All their numerical values can be found in (IERS, 1992). The summations are over eleven tide components.

Pole tide

This is a solid Earth tide caused by polar motion.

$$s_r = -\frac{h_2}{2} \frac{\omega_{\text{E}}^2 r^2}{g} \sin(2\phi)[(X - \overline{X}) \cos\lambda - (Y - \overline{Y}) \sin\lambda] \quad \text{km}$$
$$s_\phi = -l_2 \frac{\omega_{\text{E}}^2 r^2}{g} \cos(2\phi)[(X - \overline{X}) \cos\lambda - (Y - \overline{Y}) \sin\lambda] \quad \text{km}$$
$$s_\lambda = l_2 \frac{\omega_{\text{E}}^2 r^2}{g} \sin\phi[(X - \overline{X}) \sin\lambda + (Y - \overline{Y}) \cos\lambda] \quad \text{km}.$$

Here, $\omega_{\mathrm{E}} = 0.7292115 \times 10^{-4}$ rad/s is the magnitude of the Earth angular rotation vector, X and Y are the Earth-fixed coordinates of the true pole, whereas $\overline{X}$ and $\overline{Y}$ are average values of X and Y over some time span.

5.1.3 Time conversion

As we already pointed out in Section 2.3.3, converting times from TDB to TDT is a crucial task for the computation of the observables. The TDT time coordinate t_{TDT} solves the differential equation

$$\frac{dt_{\mathrm{TDT}}}{dt_{\mathrm{TDB}}} = 1 - \frac{1}{c^2}\left(U + \frac{1}{2}v_{\mathrm{E}}^2 - L_{\mathrm{C}}\right),$$

where c is the speed of light, U is the Newtonian gravitational potential at the Earth center, $v_{\mathrm{E}} = |\mathbf{v}_{\mathrm{E}}|$ is the magnitude of the barycentric velocity of the Earth and $L_{\mathrm{C}} = 1.48082686741 \times 10^{-8}$ is a constant used to remove secular terms.

In fact, the previous formula assumes that the observer (in this case the tracking station) is located at the center of the Earth. In order to take into account the actual position of the antenna, the formula should be modified as follows (cf. (Moyer, 2003), Chapter 4):

$$\frac{dt_{\mathrm{TDT}}}{dt_{\mathrm{TDB}}} = 1 - \frac{1}{c^2}\left(U_{\mathrm{E}} + \frac{1}{2}v_{\mathrm{E}}^2 - L_{\mathrm{C}}\right) - \frac{\mathbf{v}_{\mathrm{E}} \cdot \mathbf{v}_{\mathrm{ant}}^{\mathrm{E}}}{c^2} - \frac{\mathbf{a}_{\mathrm{E}} \cdot \mathbf{x}_{\mathrm{ant}}^{\mathrm{E}}}{c^2},$$

where $\mathbf{a}_{\mathrm{E}}$ is the barycentric acceleration of the Earth, $\mathbf{x}_{\mathrm{ant}}^{\mathrm{E}}$ and $\mathbf{v}_{\mathrm{ant}}^{\mathrm{E}}$ are respectively the position and the velocity of the antenna with respect to the Earth.

5.1.4 The computed observable

In Chapter 2 we defined the observable as a difference of range and touched on the integral formulation (cf. formula (2.11)), stating that it would be much more convenient. Strictly speaking, the actual observable delivered by DSN is not the range-rate of the spacecraft, but a frequency measurement $\nu(t)$, namely the difference of frequency between the uplink and the downlink radio signal. The relation between the frequency and the range-rate is described in the following and can be found in detail in (Moyer, 2003).

Let t be the time tag of the observable, receiving time of the signal at the ground antenna. The averaged received frequency is given by

$$\nu(t) = \frac{1}{\Delta}\int_{t_b - \frac{\Delta}{2}}^{t_b + \frac{\Delta}{2}} \nu(s)ds, \tag{5.1}$$

where t_b is the bounce time of the signal at the spacecraft. Analogously to what done for the range-rate, for the implementation of (5.1) ORBIT14 uses a quadrature formula:

$$\nu(t) \sim \sum_{i=1}^{m} w_i \nu_i,$$

where w_i are the weights associated to the quadrature formula, t_i are the times of discretization of the integration interval $\left[t_b - \frac{\Delta}{2}, t_b + \frac{\Delta}{2}\right]$ (the nodes) and ν_i is the instantaneous received frequency at time t_i. The formula relating ν_i and $\dot{r}_i$, the instantaneous range-rate computed at time t_i, whose formulation has been described in Chapter 2, is

$$\nu_i = M_2 f_t \left(1 - 2\frac{\dot{r}_i}{c}\right),$$

where M_2 is the *spacecraft turn-around ratio*[1], c is the speed of light, and f_{T} is the transmitted frequency at time $t_i - 2r_i/c$, where r_i is the range at time t_i.

Because of the Doppler effect, the transmitting frequency has not always the same value when the signal arrives at the spacecraft. In order to match the band width of the receiver during the entire tracking pass, the transmitted frequency is *ramped*, that is it is modified so as to take into account the relative velocity between the spacecraft and the antenna on Earth. Thus f_{T} is not constant over the tracking, but it is a linear function of time

$$f_{\mathrm{T}}(t) = f_{\mathrm{T},0} + \dot{f}_{\mathrm{T}} \cdot (t - t_0),$$

where $f_{\mathrm{T},0}$ is a reference frequency, t_0 is a reference time instant and $\dot{f}_{\mathrm{T}}$ is the ramp-rate, which could be either constant or piecewise constant.

5.1.5 Earth Troposphere

The troposphere is the lowest layer composing the Earth atmosphere, with a depth of 12 km on average. It represents an important source of perturbation for the radio signal coming from the spacecraft: with reference to Fig. 5.2, which displays the difference between Doppler observables and non-corrected ORBIT14 predictions for the DOY056 pass, we see that neglecting such calibrations would produce a signature in the observables as large as 0.3 Hz. For this reason, a proper modelization of the tropospheric effect on the observable is necessary.

[1]For the Juno spacecraft, the turn-around ratio is 3360/3599 for the Ka-band and 880/749 for the X-band.

The tropospheric perturbations appear as a delay in the time measurement of the signal traveling from the spacecraft and can thus be expressed in form of *correction to the range*. Since the troposphere contains both a *hydrostatic* part, made of the dry gases (N_2 and O_2 mostly), and a *wet* part, made of condensed water, the corrections are usually divided in two components, named *dry* and *wet* components. The two contributions are also very different qualitatively speaking: whereas the former is usually stable, the latter suffers from very stiff fluctuations (cf. Fig. 5.5).

The dry and wet tropospheric corrections are given as *zenithal* corrections to the range, $\Delta r_{\mathrm{dry,z}}$ and $\Delta r_{\mathrm{wet,z}}$, because based on the data available relative to the part of troposphere on the vertical line at the station. These must then be projected to their value at the actual elevation angle[2] of the spacecraft. The projection is performed by multiplying the terms $\Delta r_{\mathrm{dry,z}}$ and $\Delta r_{\mathrm{wet,z}}$ by *mapping functions*. ORBIT14 uses Niell's dry and wet mapping functions (cf. Niell (1996)): if α is the elevation angle of the spacecraft,

$$m(\alpha) = \frac{\frac{1}{1+\frac{a}{1+\frac{b}{1+c}}}}{\frac{1}{\sin\alpha+\frac{a}{\sin\alpha+\frac{b}{\sin\alpha+c}}}},$$

where a, b, c are constant coefficients depending on the latitude and height of the ground station, and are different for the dry mapping function $m_{\mathrm{dry}}(\alpha)$ and the wet mapping function $m_{\mathrm{wet}}(\alpha)$. In order to include the tropospheric delays in the computation of the observable, the following must be added to the range (2.9)

$$r_{\mathrm{tropo}} = \Delta r_{\mathrm{dry,z}} m_{\mathrm{dry}}(\alpha) + \Delta r_{\mathrm{wet,z}} m_{\mathrm{wet}}(\alpha).$$

Whereas the hydrostatic part of the atmosphere can be modeled from surface pressure and temperature using the laws of the ideal gases, the wet component is unpredictable and difficult to model. For Juno, the dry component is computed according to the model described in (Saastamoinen, 1972), whereas the wet component is supplied by *Advanced Water Vapor Radiometer (AWVR) measurements*.

An AWVR is a radiometer operating at frequencies from 22 to 31 GHz supporting NASA's radio science experiments. It measures atmospheric water vapor along a line of sight from the ground based antenna to the spacecraft. For the time being two AWVRs are used: one is installed at the DSN in Goldstone, the second in Madrid.

[2]The elevation angle measured with respect to a topocentric reference frame centered at the station.

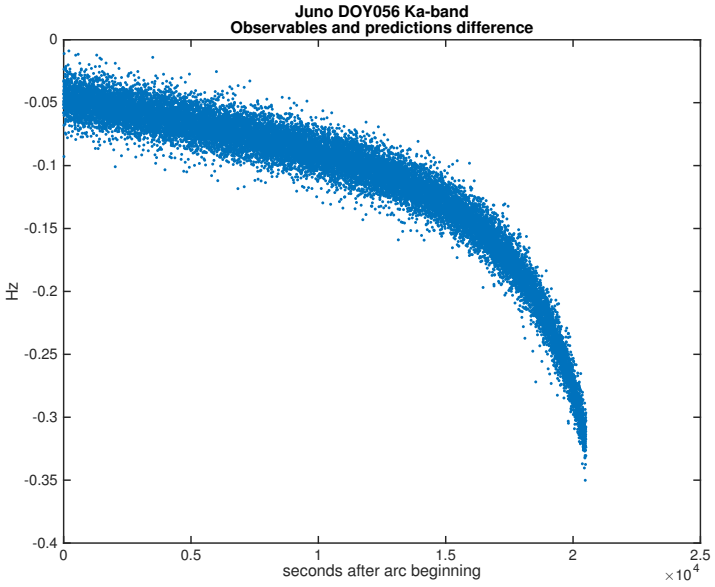

Figure 5.2: Difference between observations and predictions from DOY056, Ka-band. The predictions do not include tropospheric corrections, giving rise to a 0.3 Hz-large signature, whose peculiar shape is due to the elevation angle of the spacecraft (cf. Fig. 5.3).

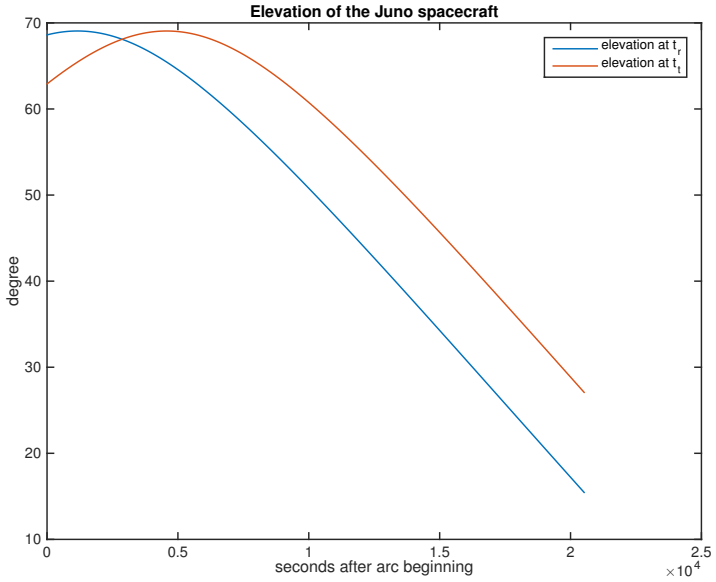

Figure 5.3: Elevation of the Juno spacecraft at transmission time and receiving time during DOY056 track.

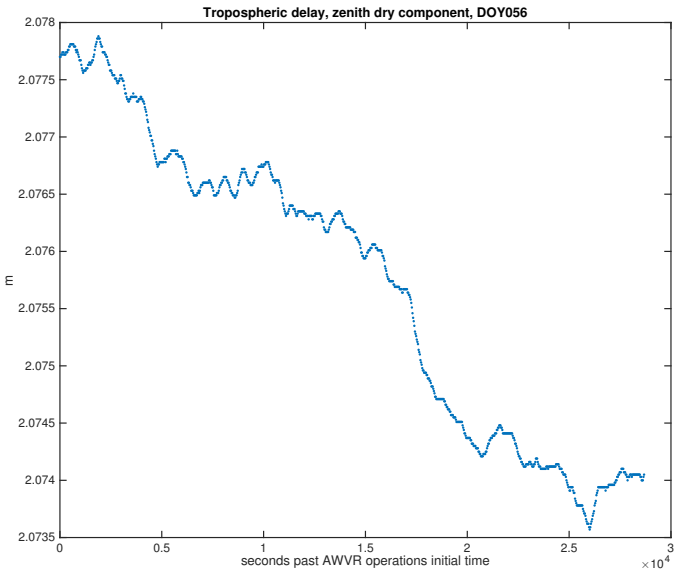

Figure 5.4: Dry component of the tropospheric corrections during DOY056 at Goldstone, CA.

For Juno the AWVR measured troposphere corrections along the line of sight to Jupiter and then mapped to zenith using the Niell mapping function. To use the data, the same function needed to applied to the desired elevation.

The measurements are expressed as corrections to the range at a given list of time instants. If the correction at a time instant not included in the list is needed, ORBIT14 performs interpolation using cubic splines.

Fig. 5.4 and 5.5 show respectively the zenith dry and the zenith wet components during DOY056 at the Goldstone station in California.

If AWVR measurements are not available (for instance in case of bad weather conditions), the tropospheric effects could be calibrated using *seasonal models*, giving predictions of the troposphere conditions based on data taken over the past years. Of course the level of accuracy of such models is inferior with respect to the AWVR data.

In this case, the functions $\Delta r_{\mathrm{dry,z}}$ and $\Delta r_{\mathrm{wet,z}}$ are expressed as trigonometric polynomials. For the dry component at time t, there exist coefficients $A_0, A_k, B_k,\ k =$

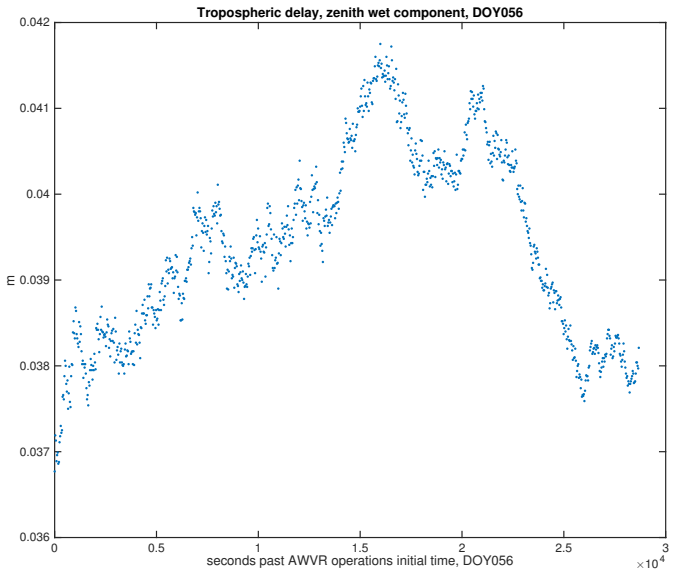

Figure 5.5: Wet component of the tropospheric corrections measured by the Advanced Water Vapor Radiometer during DOY056 at Goldstone, CA.

$1, \ldots, n$ such that

$$\Delta r_{\mathrm{dry,z}}(t) = A_0 + \sum_{k=1}^{n} A_k \cos(kX) + B_k \sin(kX),$$

where, calling t_0 the initial time of tracking and P the period of the fundamental mode, then $X = 2\pi(t - t_0)/P$ (see Cangahuala et al. (2002) for details). The wet component has a similar expression.

Fig. 5.6 and 5.7 show respectively the zenith dry and the zenith wet components for every day of the year 2014 at the Goldstone station in California.

5.1.6 Effect of charged particles

The noise budget of Doppler measurements contains also the contribution due to the interaction of the radio signal with the charged particles (plasma) contained in the solar wind and in the ionosphere. The presence of a medium characterized by refractive index fluctuations causes frequency fluctuations in the radio wave which are proportional to the square of the wavelength (cf. (Asmar et al., 2005)). Consequently Ka-band radio links suffer from these fluctuations much less than

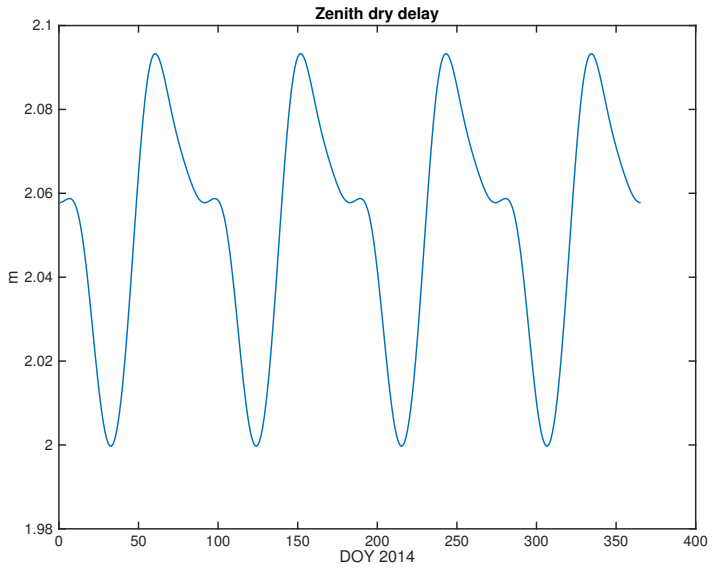

Figure 5.6: Dry component of the tropospheric corrections for the year 2014 (seasonal model).

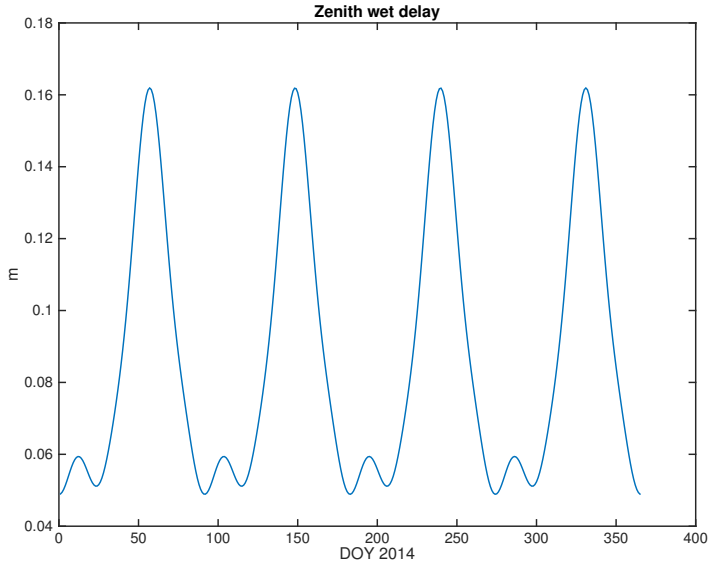

Figure 5.7: Wet component of the tropospheric corrections for the year 2014 (seasonal model).

X-band and in special conditions, such as near opposition, the plasma effect on Ka-band data is close to being negligible.

On the other hand, when the spacecraft is near conjunction it is necessary to eliminate the charged particles noise from the radiometric observables. As proposed in (Bertotti et al., 1993), in presence of a radio link featuring X/X, Ka/Ka and X/Ka phase coherent bands, by applying a suitable linear combination of the three types of observable, it is possible to remove completely the plasma noise. For Juno such a triple of links is not available, thus it is not possible to achieve a complete removal; following (Mariotti and Tortora, 2013), it is still possible to calibrate a substantial part of the charged particle noise exploiting the two available radio links X/X and Ka/Ka: if $f_{\mathrm{Ka/Ka}}$ and $f_{\mathrm{X/X}}$ are the received fractional frequencies respectively in Ka-band and X-band, the almost-calibrated observable is given by

$$f_{\mathrm{cal}} \simeq 1.05 f_{\mathrm{Ka/Ka}} - 0.05 f_{\mathrm{X/X}}.$$

Since the Juno Ka-band data analyzed in this chapter were obtained near opposition, we were in condition of ignoring plasma calibration. This might also be the case of the first Gravity orbits, but as Fig. 1.5 suggests, around perijove 28 noise removal will be crucial, as the spacecraft will be near conjuction.

5.1.7 Effect of the spin on the observable

The radio signal sent from the ground antenna to the spacecraft is circularly polarized. Since the spacecraft is spinning[3], the received frequency in the rotating frame at the spacecraft is lowered or increased, depending on the polarization of the signal. The Ka-band signal is Left-hand Circularly Polarized (LCP) for reception at the spacecraft and Right-hand Circularly Polarized (RCP) for transmission, whereas the X-band signal is RCP for both. This induces the Doppler shift (cf. Marini (1971))

$$\Delta\nu = -\omega_{\mathrm{spin}}(1 \pm M_2), \tag{5.2}$$

where ω_{spin} is the spin frequency of the spacecraft and M_2 the turn-around ratio of the spacecraft and the sign is chosen according to the polarization.

For the Juno spacecraft, this shift is ~ 0.0022 Hz for the Ka-band and ~ 0.0722 Hz for the X-band[4]. If one does not correct the Doppler observables with the effect of the spin, the least-squares process would correct the velocity of the spacecraft in order to account for this signal. As a consequence, computing a prediction of

[3]At the time of the analyzed pass the spin rate was 1 rpm, but currently, and at Jupiter, the spacecraft is rotating at 2 rpm

[4]These values were provided by the University of Bologna via private communication

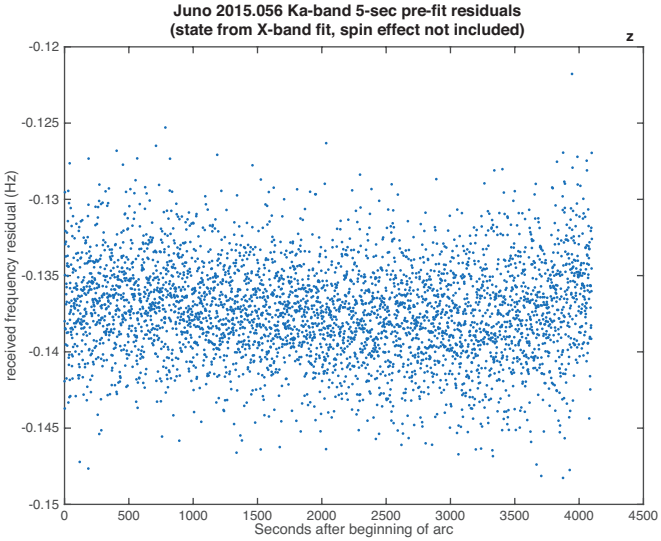

Figure 5.8: Difference between the Ka-band Doppler data and ORBIT14 predictions using initial conditions obtained by fitting the X-band data. The residuals have an offset of ~ -0.137 Hz because the effect of the spinning spacecraft had not been included in the X-band Doppler.

the Ka-band data using the spacecraft state vector obtained fitting the X-band data (or viceversa) would produce biased residuals. This is showed in Fig. 5.8 and Fig. 5.9. The first is the difference of the Ka-band Doppler observables and the predictions computed by ORBIT14 using the state vector obtained from a previous fit of non-corrected X-band data. A bias of ~ -0.137 Hz is present. The second figure shows the same difference, but in this case the X-band data had been corrected before the fit using (5.2). The bias is no longer present in the new figure, the mean being $\sim -2.3 \times 10^{-4}$.

Another effect due to the spinning spacecraft is due to a misalignment between the spacecraft spin axis and the antenna. If not taken into account, this results in a periodic effect in the residuals, the period being a multiple of the rotation period of the orbiter (cf. Fig. 5.16). See Section 5.2.3 for possible solutions.

5.2 Data processing

The results of the statistical analysis of the Juno Doppler data using ORBIT14 are described in this section. Before going on to deal with the fit of the observables,

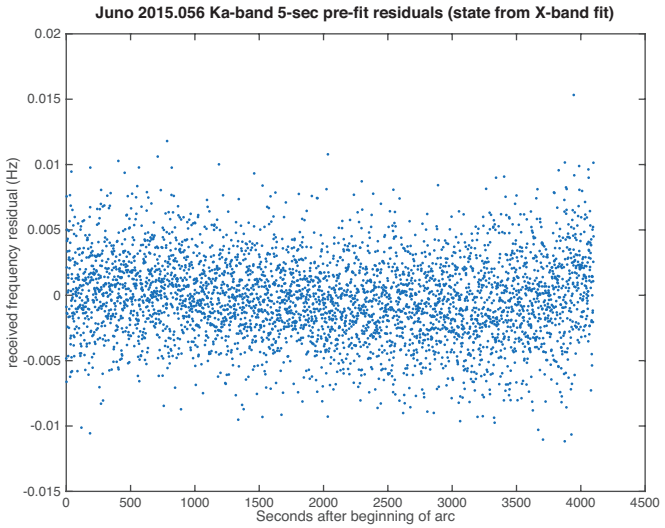

Figure 5.9: Difference between the Ka-band Doppler data and ORBIT14 predictions using initial conditions obtained by fitting the X-band data. Since the effect of the spinning spacecraft has been included, no bias is present.

we will dwell on the analysis of the intrinsic noise contained in the Doppler data and in the computed observables generated by ORBIT14.

We will fully analyse the DOY056 Ka-band data set. It has been obtained by two-way telemetry between the Juno spacecraft and the DSS-25 station in Goldstone, California. The sampling time is 1 second and the tracking time is approximately six hours. The elevation angle of the spacecraft over the topocentric reference frame at the station goes from ~ 70 degrees to ~ 15 degrees, see Fig. 5.3. Finally, the data set is unramped.

5.2.1 Quality of the data

To investigate the noise of the Doppler data we did as follows: first, we made a polynomial fit of the data using Chebyshev polynomials (cf. Section 5.3.1); second, we computed the Allan Deviation (cf. Section 5.3.2) of the difference between the data and the fitting polynomial, divided by the reference frequency[5]. The Allan Deviation (from now on, AD) was computed at times $\tau = 1, 2, \ldots, 1000$ seconds.

The result for the DOY056 Ka-band Doppler data is in Fig. 5.10. The value of the

[5]For the Ka-band data the reference frequency is ~ 34 GHz

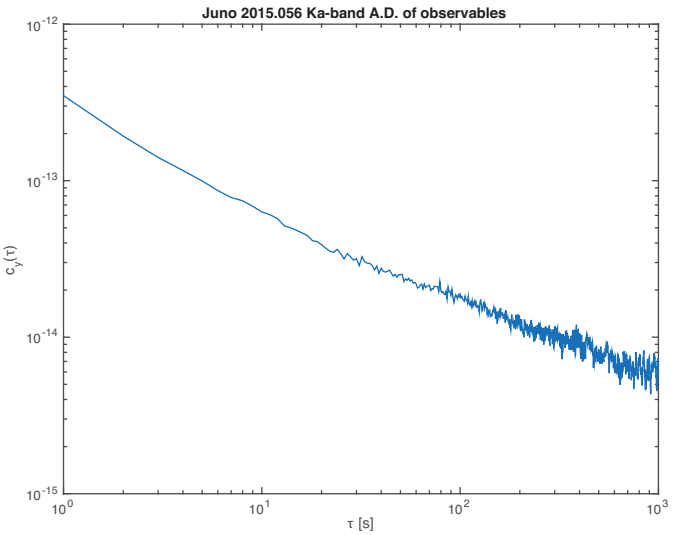

Figure 5.10: Allan Deviation of the Juno DOY056 Ka-band Doppler observables (received frequencies) for $t = 1, \ldots, 1000$ sec.

AD for this data set at 1000 s is $\sim 6 \times 10^{-15}$. This should be compared to what stated in (Asmar et al., 2005): the authors show that the best accuracy currently achievable[6] is about 3×10^{-15} at 1000 s, thus Juno performs 2 times worse.

5.2.2 Numerical noise of the computed observable

In order to detect the presence of numerical noise in the predictions computed by ORBIT14, we follow the same scheme used for the observables. That is, we fit the predictions to a polynomial and then compute the AD of the difference. The result relative to the DOY056 Ka-band Doppler data is in Fig. 5.11. The AD $\sigma(\tau)$ is less than 10^{-16} for all $\tau = 1, 2, \ldots, 1000$ sec. We conclude that the numerical noise introduced by the software when computing the predictions is much smaller than the noise of the observables, thus it is negligible. Such small a value of numerical noise could be reached using the integrated formulation for the computation of the observable, (5.1) for the observed frequency and (2.11) for the range-rate. As already shown in (Milani and Gronchi, 2010), Chapter 17, the integrated observable allows more control of the rounding off problems than the differenced observable (2.10).

[6]Note that although the cited article is more than 10 years old, such statement is still true since technology has not improved.

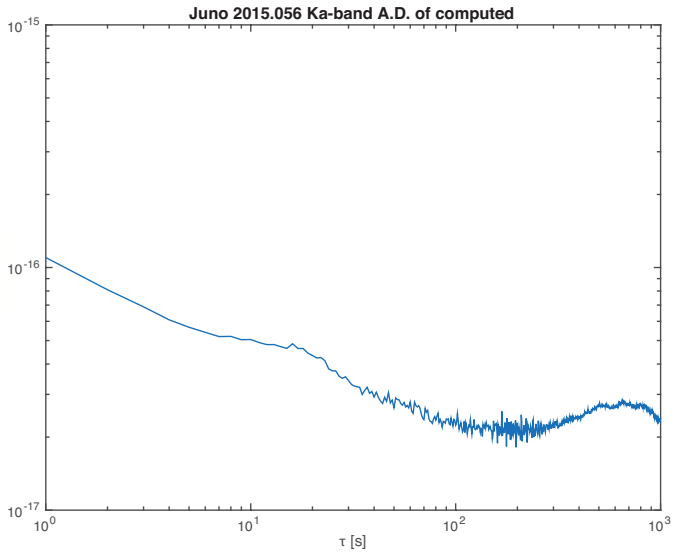

Figure 5.11: Allan Deviation of the predictions computed by ORBIT14 relative to the DOY056 Doppler data.

Note that the computed observables did not include the tropospheric corrections. The latter could contain additional noise which would affect the final result (see Section 5.2.3). In this case, the tropospheric data should be pre-processed in such a way that they are a smooth function of the time, allowing for a reduction of the numerical noise.

5.2.3 Least squares fit

In this section we describe the results of the least-squares fit of the DOY056 Ka-band observables performed with ORBIT14. The goal is to measure the noise of the residuals obtained from the fit.

Pre-fit residuals

Before going on to study the post-fit residuals, let us analyse the difference between the observables and the predictions (including the tropospheric corrections), the so-called *pre-fit residuals*. Figure 5.12 shows that the pre-fit residuals are characterised by an offset of about ~ -0.05 Hz and a linear drift. The former is due to

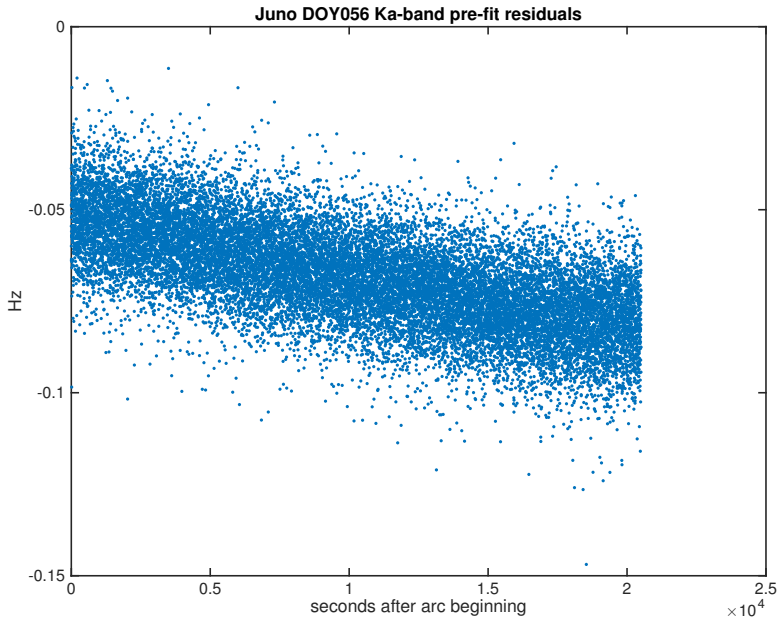

Figure 5.12: Difference between observables (DOY056 Ka-band) and predictions computed by ORBIT14.

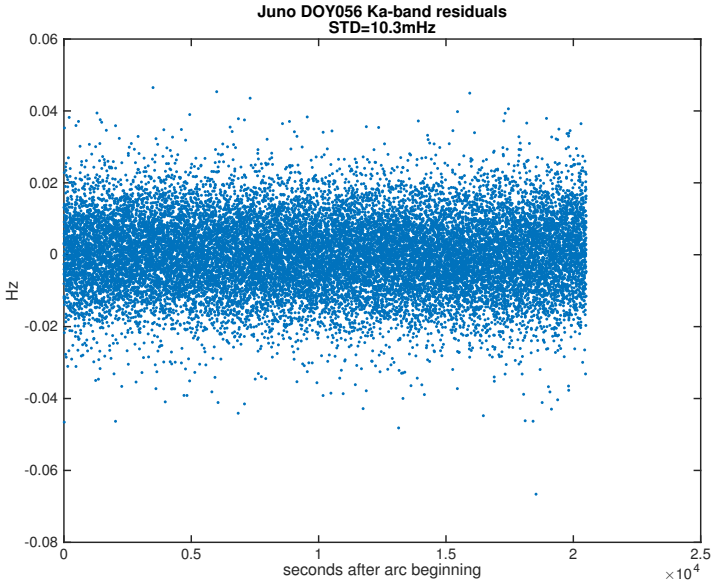

Figure 5.13: Residuals obtained at convergence of the least-squares fit.

an error in the initial conditions used, the latter is caused by unmodeled solar radiation pressure. Whereas the error in the initial conditions will be corrected during the fit, the solar radiation pressure will be taken into account by determining a semi-empirical parameter representing a constant force in the radial direction. The choice of the radial component is due to the fact that the solar radiation pressure has approximately the same direction.

Post-fit residuals

Since a single arc in cruise phase is not enough to determine the six components of the state of the spacecraft, we constrained it to its nominal value with apriori uncertainty of 1 km in position and 1 cm/s in velocity.

Fig. 5.13 shows the residuals of the DOY056 Ka-band data at convergence. The standard deviation (STD) is 10.3 mHz, which corresponds to $\sim 90\mu$m/s. The result obtained by the Radio-Science Laboratory - Università La Sapienza in Rome (cf. (Durante and Iess, 2015)), using the Jet Propulsion Laboratory software MONTE, for the same data set is STD=19 mHz, so almost 2 times worse than the result obtained with ORBIT14.

The AD of the ORBIT14 residuals is in Fig. 5.14. By comparing the AD curve of the residuals with the AD curve of a White Noise stochastic process (given by the function of the time $\tau^{-1/2}$, see Section 5.3.2), we remark that the two curves are almost parallel except for the smallest and largest considered times. As regards the smallest times, this is due to the noise contained in the observables: the observables and the residuals have indeed the same AD. As far as the largest times are concerned, a part of the difference stems from noise in the tropospheric corrections supplied by the AWVR. If we look at the Allan Deviation of the residuals of the same pass, obtained applying tropospheric corrections based on a seasonal model (Fig. 5.15), indeed we see that the difference in slope for large times has now diminuished and its value at 1000 sec is 6×10^{-15}, the same value obtained for the observables (Fig. 5.10). Investigation on the possible sources accounting for the remaining difference is still going on.

Finally, we computed the Power Spectral Density of the residuals (Fig. 5.16). The main feature is the peak at ~ 0.33 Hz, corresponding to twice the rotation period of the spacecraft. It is not known what this stems from: it might be caused by an antenna phase pattern that has two maxima per rotation. A possible way to deal with this problem is to correct the position of the antenna in the software by reading its relative position with respect to the spin axis from the SPICE C-kernel, the component of SPICE about the attitude of the spacecraft and the instruments. Another way to cope with it is by applying a suitable filter to the

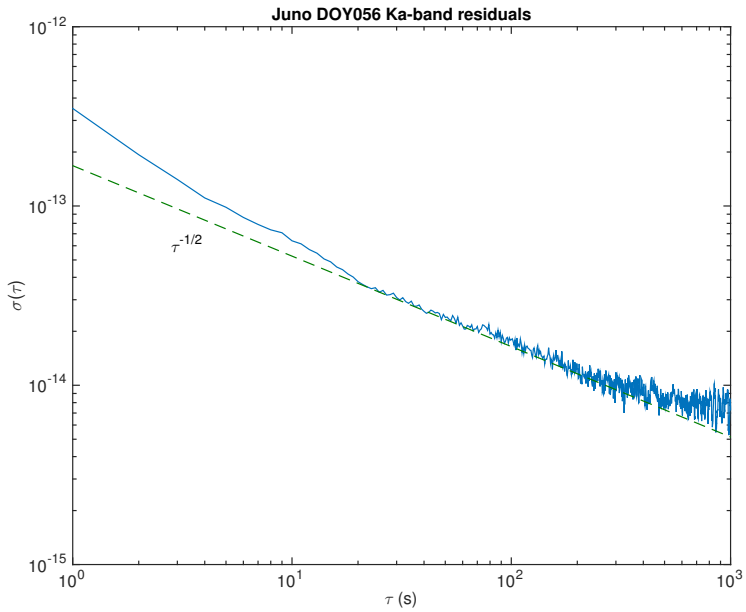

Figure 5.14: Allan Deviation at times $\tau = 1, \ldots, 1000$ of the residuals in Fig. 5.13 versus Allan Deviation of a White Noise process (curve $\tau^{-1/2}$).

Doppler observables (cf. (Carpino et al., 1987)) in such a way that the effect described above is deleted. According to our estimates, a 20-second low-pass filter (Fig. 5.17) is able to eliminate both the peak and the higher-frequency noise. We have not yet explored in detail such possibility, yet we intent on doing it in the near future.

5.3 Mathematical background

In this section we provide the mathematical details about Chebyshev polynomials and the definition and basic properties of the Allan Deviation, much used for the analysis of the Juno data.

5.3.1 Chebyshev polynomials

The *Chebyshev polynomials* of the first kind are a set of polynomials defined on the interval $[-1, 1]$. They form a set of orthogonal polynomials with respect to the

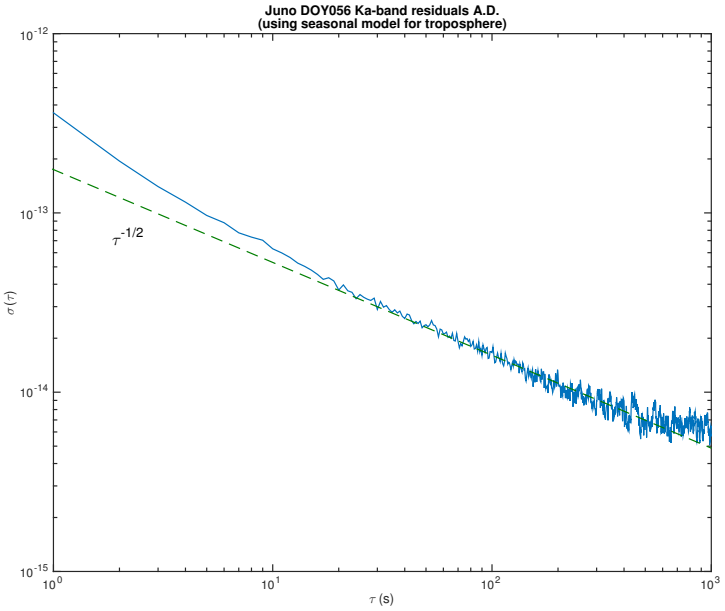

Figure 5.15: Allan Deviation at times $\tau = 1, \ldots, 1000$ of the residuals obtained applying tropospheric corrections versus Allan Deviation of a White Noise process (curve $\tau^{-1/2}$).

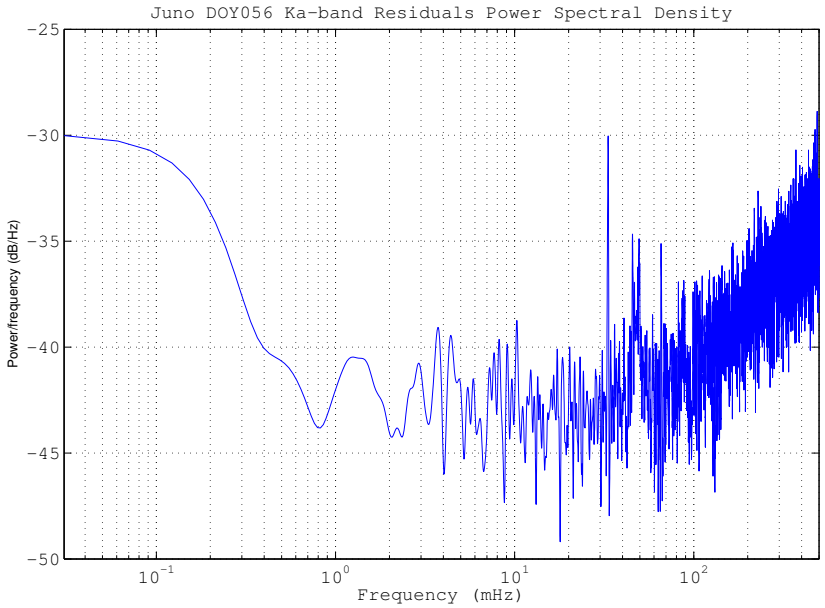

Figure 5.16: Power Spectral Density of the DOY056 Ka-band residuals.

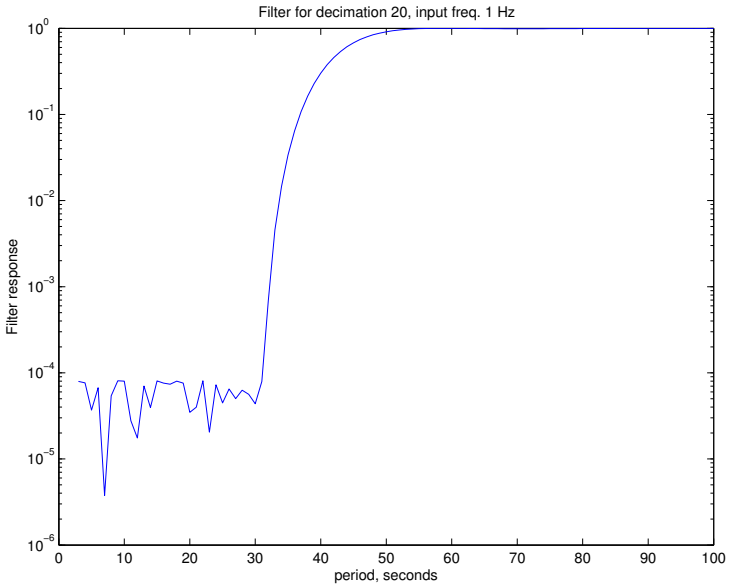

Figure 5.17: Low-pass digital filter decimating at 20 seconds the Doppler data. All the frequencies lower than 30 seconds are passed by the filter, while the high frequencies are multiplied by 10^{-4}.

scalar product

$$\langle f, g \rangle = \int_{-1}^{1} (1 - x^2)^{-\frac{1}{2}} f(x) g(x) \mathrm{d}x.$$

The following can be taken as a definition:

Definition 1. The *Chebyshev polynomial of degree* n is defined by the recurrence relation

$$\begin{cases} T_0(x) = 1 \\ T_1(x) = x \\ T_n(x) = 2xT_{n-1}(x) - T_{n-2}(x), \quad n \geq 2 \end{cases}$$

It can be proved that the roots of the degree-n polynomial T_n are all distinct and are given by

$$x_k = \cos\left(\frac{2k-1}{2n}\pi\right), \quad k = 1, \ldots, n.$$

The importance of knowing the expression of such roots is in that the polynomial interpolation of a function made using as nodes the Chebyshev roots produces an interpolation error somewhat minimal. In fact, the interpolation error of a

function $f \in C^{n+1}([-1,1])$ approximated by a degree-n polynomial $P(x)$ in the nodes $(x_j)_{j=0,\dots,n}$ is

$$f(x) - P(x) = \frac{f^{(n+1)}(\xi)}{(n+1)!} \prod_{j=0}^{n} (x - x_j), \quad \xi \in [-1,1],$$

where $f^{(n+1)}$ is the derivative of order $n+1$ of f. Therefore, taking the maximum, we have

$$\max_{x\in[-1,1]} |f(x) - P(x)| = \frac{1}{(n+1)!} \max_{x\in[-1,1]} \left|f^{(n+1)}(\xi)\right| \max_{x\in[-1,1]} \left|\prod_{j=0}^{n} (x - x_j)\right|.$$

One is interested in having the minimum possible value for $\max_{x\in[-1,1]} \left|\prod_{j=0}^{n}(x - x_j)\right|$. It can be shown that

$$\max_{x\in[-1,1]} \left|\prod_{j=0}^{n} (x - x_j)\right| \geq 2^{-n}.$$

Moreover, since $|T_{n+1}| = 2^n$, then choosing the roots of a degree-$n+1$ Chebyshev polynomial as interpolation nodes leads to having

$$\max_{x\in[-1,1]} \left|\prod_{j=0}^{n} (x - x_j)\right| = 2^{-n},$$

that is the minimum value achievable.

5.3.2 Allan Deviation

The Allan Deviation has been introduced in (Allan, 1966) in order to study the frequency stability of an oscillator. It is used nowadays as a powerful instrument to study the intrinsic noise of a frequency signal.

Let us suppose to have a frequency measurement $\nu(t)\colon \mathbb{R} \to \mathbb{R}$. Starting from this function, we can define the *fractional frequency fluctuations* function

$$y(t) := \frac{\nu(t) - \nu_0}{\nu_0},$$

where ν_0 is a reference frequency.

Let us fix $T_0 \in \mathbb{R}$ a generic instant of time and, for a given $\tau \in \mathbb{R}^+$, let $(T_k)_k$ be the sequence of $M+1$ time instants defined by

$$T_k = T_0 + (k-1)\tau, \ k = 1, \dots, M+1.$$

Let us define $\overline{y}_k$, the *average value* of y over the interval (T_k, T_{k+1}):

$$\overline{y}_k = \frac{1}{\tau}\int_{T_k}^{T_{k+1}} y(s)\mathrm{d}s.$$

Definition 2. The *Allan Variance* of the signal y at the *analysis time* $\tau \in \mathbb{R}^+$ is given by

$$\sigma_y^2(\tau) = \frac{1}{2M}\sum_{k=0}^{M-1}(\overline{y}_{k+1} - \overline{y}_k)^2. \tag{5.3}$$

The *Allan Deviation* is $\sigma_y(\tau) := \sqrt{\sigma_y^2(\tau)}$.

Let us now consider the case of a *discrete* frequency signal $(y_i)_{i=0,\dots,N}$ in the interval $[t_0, t_0 + T]$, with discretization rate τ_0. Let $m \in \mathbb{R}^+$ and $\tau = m\tau_0$, the analysis time. If we define

$$M := \left[\frac{T}{\tau}\right] - 1,$$

the average values $\overline{y}_k$, $k = 0, \dots, M$, simply read

$$\overline{y}_k = \frac{1}{m}\sum_{j=1}^{m} y_{k+j-1}.$$

The Allan Variance of the discrete signal y at the analysis time τ has the same expression (5.3).

The Allan Deviation of a signal as a function of the analysis time can be used to analyse the noise contained in the signal by comparing it to the Allan Deviation of the most common stochastic processes. In this work we will consider only *white noise* and *random walk*. It can be shown (cf. (Tehrani, 1983)) that the Allan Deviation of such processes is proportional to a power of τ, namely

$$\sigma_{\mathrm{WN}}(\tau) \propto \tau^{-\frac{1}{2}}, \quad \sigma_{\mathrm{RW}}(\tau) \propto \tau^{-1},$$

where σ_{WN} indicates the Allan Deviation of White Noise and σ_{RW} that of Random Walk.

5.4 Reading the ODF data file

The observables and all the other tracking data are saved in ODF (Orbital Data File) format files, created by the DSN. In order to be used by the ORBIT14

software, the data had to be extracted and converted in the ORBIT14 format. Following the guidelines contained in (Shin, 2008), the Matlab function `odf2orb.m` has been designed, coded and tested.

The routine reads a given ODF file and:

- writes the information in a number of .txt files for consultation;
- produces the files .obs and .trackinfo, in the ORBIT14 format.

The script uses two functions called `swapbits.m` and `convbi.m`, which respectively write the bits in the byte in the reverse order and convert a sequence of bits in decimal number. The script also produces a number of auxiliary files (frqncy.txt, obsvbl.txt, band.txt, timetags.txt) used for writing the ORBIT14 files.

If `filename` is the name of the ODF file, the files generated by `odf2orb.m` are:

Files containing orbit data

- `data_filename.txt` : contains all the data extracted by the file. See later for the details.
- `data_filename_X.txt` : contains all the X-band data extracted by the file (if any).
- `data_filename_Ka.txt` : contains all the Ka-band data extracted by the file (if any).
- `data_filename_1way.txt` : contains all the 1-way type data extracted by the file (if any).
- `data_filename_2way.txt` : contains all the 2-way type data extracted by the file (if any).

The information held is the same for all the previous files. The files are organized in rows, each one containing the same number of fields. Each row contains:

Time tag time of the observable, expressed as seconds past Jan 1, 1950, hh:00:00:00.

Data type type of the doppler observable (11=one-way, 12=two-way, 13=three-way)

Observable doppler observable (Hz)

Reference frequency the reference frequency used to compute the sky-frequency (Hz)

Downlink band 0=N/A or Ku-band, 1=S-band, 2=X-band, 3=Ka-band

Uplink band 0=N/A or Ku-band, 1=S-band, 2=X-band, 3=Ka-band

Downlink delay (sec)

Uplink delay (sec)

Spacecraft ID (61=Juno)

Files containing RAMP info

- `ramp_filename.txt` : contains all the information about the ramped frequencies (if any).

For each station, the ramp file contains the following information (organized in rows):

Station ID

Ramp start time expressed as seconds past Jan 1, 1950, hh:00:00:00.

Ramp end time expressed as seconds past Jan 1, 1950, hh:00:00:00.

Ramp start frequency frequency at the ramp start time (Hz)

Ramp rate derivative of the frequency wrt time (Hz/s)

Files for ORBIT14

- `o14_filename.obs` : contains the observables as well as the time tags, the type of observable, the station ID, the compression time.
- `o14_filename.trackinfo` : contains information such as uplink and downlink delays and the RAMP tables.

For the time being, the routine `odf2orb` can only read doppler data, since the ORBIT14 software can only process that kind of observables.

Bibliography

Allan, D. (1966). Statistics of Atomic Frequency Standards. In *Proceeding of the IEEE*, volume 54.

Anderson, J. (1976). *Jupiter. Studies of the interior, atmosphere, magnetosphere and satellites.*, chapter The Gravity Field of Jupiter. The University of Arizona Press.

Archinal, B. et al. (2011). Report of the IAU Working Group on Cartographic Coordinates and Rotational Elements: 2009. *Celestial mechanics and dynamical astronomy.*

Asmar, S., Armstrong, J., Iess, L., and Tortora, P. (2005). Spacecraft Doppler tracking: Noise budget and accuracy achievable in precision radio science observations. *Radio Science*, 40.

Bertotti, B., Comoretto, G., and Iess, L. (1993). Doppler tracking of spacecraft with multi-frequency links. *Astron. Astrophys.*, 269:608–616.

Bierman, G. J. (2006). *Factorization Methods for Discrete Sequential Estimation.* Dover Publications.

Campbell, J. and Synnott, S. (1985). Gravity field of the Jovian system from Pioneer and Voyager tracking data. *Astronomical Journal*, (90):364–372.

Cangahuala, A., D'Amario, L., Legerton, V., and Singleton, F. (2002). Mars exploration rover (mer) software interface specification. Technical report, JPL.

Carpino, M., Milani, A., and Nobili, A. M. (1987). Long-term numerical integrations and synthetic theories for the motion of the outer planets. *Astron. Astrophys.*, 181:182–194.

Cicalò, S., Schettino, G., Di Ruzza, S., Alessi, E., Tommei, G., and Milani, A. (2016). The BepiColombo MORE gravimetry and rotation experiments with the ORBIT14 software. *Mon. Not. R. Astron. Soc.*

CT (1959). Chicago Tribune: http://archives.chicagotribune.com/1959/01/29/page/1/article/cannot-stop-integration-almond-says.

Dehant, V. et al. (2011). Revealing Mars' deep interior: Future geodesy missions using radio links between landers, orbiters and the earth. *Planetary and Space Science*.

Dehant, V. and Mathews, P. (2015). *Precession, Nutation and Wobble of the Earth.* Cambridge Univ. Press.

Durante, D. and Iess, L. (2015). Juno Ka-test - statistical analysis of Ka-band observables. Private communication, Radio-Science Laboratory - University of Rome.

ESA/SRE(2014)1 (2014). JUICE. JUpiter ICy moons Explorer. Exploring the emergence of habitable worlds around gas giants. Technical report, European Space Agency.

Folkner, W. M., Williams, J. G., and Boggs, D. H. (2009). The planetary and lunar ephemeris de 421. *The Interplanetary Network Progress Report*.

Galanti, E. and Kaspi, Y. (2016). An adjoint based method for the inversion of the juno and cassini gravity measurements into wind fields. *The Astrophysical Journal*.

Gauss, C. (1809). Theoria motus corporum coelestium in sectionis conicis solem ambientum.

Gavrilov, S. and Zharkov, V. (1977). Love numbers of the giant planets. *Icarus*, (32):443–449.

Grammier, R. (2008). A Look inside the Juno Mission to Jupiter. *IEEEAC*.

Guillot, T. and Gautier, D. (2007). Giant Planets. In Spohn, T. and Schubert, J., editors, *Treatise of Geophysics: "Planets and Moons"*, volume 10, pages 439–464. Elsevier Publ.

Heine, E. (1861). *Handbuch der Kugelfunctionen. Theorie und Anwendungen. Band I, II.* Georg Reimer.

Helled, R., Anderson, J. D., Schubert, G., and Stevenson, D. (2011). Jupiter's moment of inertia: A possible determination by Juno. *Icarus*, 216:440–448.

Helmert, F. (1880). *Die mathematischen und physikalischen theorieen der höheren geodäsie.* B. G. Teubner.

IERS (1992). IERS standards (1992). Technical report, Ed. by Dennis D. McCarthy.

IERS (2016). International Celestial Reference System http://aa.usno.navy.mil/faq/docs/icrs_doc.php.

Iess, L., Jacobson, R., Ducci, M., Stevenson, D., Lunine, I., Armstrong, J., Asmar, S., Racioppa, P., Rappaport, N. J., and Tortora, P. (2012). The tides of Titan. *Science*, (337):457–459.

Iorio, L. (2010). Juno, the angular momentum of Jupiter and the Lense-Thirring effect. *New Astronomy*, 15(6):554–560.

Irwin, A. and Fukushima, T. (1999). *Astron. Astrophys.*, 348:642–652.

Jacobson, R. A. (2003). JUP230 Orbit Solution.

Kaspi, Y., Hubbard, W., Showman, A., and G.R., F. (2010). Gravitational signature of Jupiter's internal dynamics. *Geophysical Research Letters.*

Kaula, W. (1966). *Theory of Satellite Geodesy: Applications of Satellites to Geodesy.* Dover Publications.

Klioner, S. (1991). Influence of the Quadrupole Field and Rotation of Objects on Light Propagation. *Astron. Zh.*, 68:1046–1062.

Konopliv, A. and Yoder, C. (1996). Venusian k_2 tidal Love number from Magellan and PVO tracking data. *Geophys. Res. Lett.*, 23:1857–1860.

Konopliv, A. S. and Sjogren, W. L. (1994). Venus Spherical Harmonic Gravity Model to Degree and Order 60. *Icarus*, 112(1):42 – 54.

Kopp, G. and Lean, J. L. (2011). A new, lower value of total solar irradiance: Evidence and climate significance. *Geophys. Res. Lett.*, 38.

Le Maistre, S., Folkner, W. M., Jacobson, R., and Serra, D. (2016). Jupiter spin-pole precession rate and moment of inertia from Juno radio-science observations. *Planetary and Space Science*.

Ma, C. and Feissel, M. e. (1997). Definition and Realization of the International Celestial Reference System by VLBI Astrometry of Extragalactic Objects. Technical report, IERS.

Marini, J. (1971). The effect of satellite spin on two-way doppler range-rate measurements. *IEEE Transactions on Aerospace and Electronics System*, AES-7(2):316–320.

Mariotti, G. and Tortora, P. (2013). Experimental validation of a dual uplink multifrequency dispersive noise calibration scheme for deep space tracking. *Radio Science*, 48(2):111–117.

Mashhoon, B., Hehl, F. W., and Theiss, D. S. (1984). On the Gravitational Effects of Rotating Masses: The Thirring-Lense Papers. *General Relativity and Gravitation*, 16(8).

Matousek, S. (2007). The Juno New Frontiers mission. *Acta Astronautica*, 61(10):932 – 939.

Mignard, F. (1978). Multiple expansion of the tidal potential. *Celestial Mechanics*, 18:287–294.

Milani, A. and Gronchi, G. F. (2010). *Theory of Orbit Determination*. Cambridge University Press.

Milani, A., Tommei, G., Vokrouhlicky, D., Latorre, E., and Cicalò, S. (2010). Relativistic models for the BepiColombo radioscience experiment. In *Relativity in Fundamental Astronomy: Dynamics, Reference Frames and Data Analysis*, volume 261. IAU Symposium, Cambridge University Press.

Moyer, T. D. (2003). *Formulation for Observed and Computed Values of Deep Space Network Data Types for Navigation*. Wiley-Interscience.

Mukai, R., Hansen, D., Mittskus, A., Taylor, J., and Danos, M. (2012). Juno telecommunications. *DESCANSO Design and Performance Summary Series - Telecommunications*.

Muller, P. and Sjogren, W. (1968). Lunar mass concentrations: Mascons. *Science*, 161:680.

Niell, A. (1996). Global mapping functions for the atmosphere delay at radio wavelengths. *Journal of Geophysical Research*, 101(B2):3227–3246.

Nordtvedt, K. (1970). Post-Newtonian metric for a general class of scalar-tensor gravitational theories and observational consequences. *Astrophysics Journal*.

Padovan, S., Margot, J., Hauck, S. A., Moore, W., and Solomon, S. C. (2014). The tides of Mercury and possible implications for its interior structure. *Journal of Geophysical Research*.

Parisi, M., Galanti, E., Finocchiaro, S., Iess, L., and Kaspi, Y. (2016). Probing the atmospheric dynamics of Jupiter's Great Red Spot with the Juno gravity experiment. *Icarus*, 267:232–242.

Petit, G. and Luzum, B. e. (2010). IERS conventions (2010). IERS technical note; 36, IERS Conventions Centre.

Rickman, H., editor (2001). *Proceedings of the Twenty-Fourth General Assembly, Manchester 2000*, volume XXIV-B. Transactions of the IAU, San Francisco: ASP.

Saastamoinen, J. (1972). *HENRIKSEN, The Use of Artificial Satellites for Geodesy*, volume 15, chapter Atmospheric Correction for the Troposphere and Stratosphere in Radio Ranging of Satellites, pages 247–251. Geophys. Monogr. Ser.

Seeber, G. (2003). *Satellite Geodesy - 2nd completely revised and extended edition*. Walter De Gruyter - Berlin - New York.

Shapiro, I. I. (1964). Fourth Test of General Relativity. *Phys. Rev. Lett.*, 13.

Shin, D. (2008). TRK-2-18 Tracking System Interfaces Orbit Data File Interface. Technical report, DSN.

Tehrani, M. M. (1983). Ring Laser Gyro Data Analysis with Cluster Sampling Technique. In *Proceedings of SPIE*, volume 412.

Teyssandier, P. and Le Poncin-Lafitte, C. (2008). a nice tool for relativistic astrometry:. synge's world function. In *The Eleventh Marcel Grossmann Meeting On Recent Developments in Theoretical and Experimental General Relativity, Gravitation and Relativistic Field Theories*, volume 1, pages 2573–2575.

Tommei, G., Dimare, L., Serra, D., and Milani, A. (2015). On the Juno Radio Science Experiment: models, algorithms and sensitivity analysis. *Monthly Notices of Royal Astronomical Society*, 446 (2):3089 – 3099.

Tommei, G., Milani, A., and Vokrouhlicky, D. (2010). Light time computations for the Bepicolombo Radioscience experiment. *Celestial mechanics and dynamical astronomy*, 107.

van der Hucht, K., editor (2008). *Proceedings of the Twenty-Sixth General Assembly, Prague 2006*, volume XXVI-B. Transactions of the IAU, Cambridge University Press.

Will, C. (1971). Theoretical frameworks for testing relativistic gravity ii: Parametrized post-Newtonian hydrodynamics and the Nordtvedt effect. *Astrophys. J.*, (163):611–628.

Williams, D. R. (2015). Jupiter Fact Sheet http://nssdc.gsfc.nasa.gov/planetary/factsheet/jupiterfact.html.

Young, R. (1998). The Galileo probe mission to Jupiter: Science overview. *Journal of Geophysical Research*, 103(E10):22,775–22,790.